DESIGN, FABRICATION, AND MEASUREMENT OF EFFICIENT
BEAM-SHAPING REFLECTORS FOR 5G MM-WAVE APPLICATIONS

A THESIS SUBMITTED TO
THE GRADUATE SCHOOL OF NATURAL AND APPLIED SCIENCES
OF
MIDDLE EAST TECHNICAL UNIVERSITY

BY

GÖKHAN ÇAĞLAYAN KARAOVA

IN PARTIAL FULFILLMENT OF THE REQUIREMENTS
FOR
THE DEGREE OF MASTER OF SCIENCE
IN
ELECTRICAL AND ELECTRONICS ENGINEERING

MAY 2021

Approval of the thesis:

DESIGN, FABRICATION, AND MEASUREMENT OF EFFICIENT BEAM-SHAPING REFLECTORS FOR 5G MM-WAVE APPLICATIONS

submitted by **GÖKHAN ÇAĞLAYAN KARAOVA** in partial fulfillment of the requirements for the degree of **Master of Science in Electrical and Electronics Engineering Department, Middle East Technical University** by,

Prof. Dr. Halil Kalıpçılar
Dean, Graduate School of **Natural and Applied Sciences** _____

Prof. Dr. İlkay Ulusoy
Head of Department, **Electrical and Electronics Engineering** _____

Prof. Dr. Özgür Ergül
Supervisor, **Electrical and Electronics Engineering** _____

Examining Committee Members:

Prof. Dr. Mustafa Kuzuoğlu
Electrical and Electronics Engineering, METU _____

Prof. Dr. Özgür Ergül
Electrical and Electronics Engineering, METU _____

Prof. Dr. Sencer Koç
Electrical and Electronics Engineering, METU _____

Prof. Dr. Özlem Aydın Çivi
Electrical and Electronics Engineering, METU _____

Prof. Dr. Birsen Saka
Electrical and Electronics Engineering, Hacettepe University _____

Date: 20.05.2021

I hereby declare that all information in this document has been obtained and presented in accordance with academic rules and ethical conduct. I also declare that, as required by these rules and conduct, I have fully cited and referenced all material and results that are not original to this work.

Name, Surname: Gökhan Çağlayan Karaova

Signature   :

ABSTRACT

**DESIGN, FABRICATION, AND MEASUREMENT OF EFFICIENT
BEAM-SHAPING REFLECTORS FOR 5G MM-WAVE APPLICATIONS**

Karaova, Gökhan Çağlayan

M.S., Department of Electrical and Electronics Engineering

Supervisor: Prof. Dr. Özgür Ergül

May 2021, 99 pages

In this study, an optimization procedure to design corrugated passive metallic reflectors for the fifth-generation millimeter wave (5G mm-wave) applications, as well as the fabrication and measurement of the designed reflectors, are presented. Such reflecting surfaces can be used as passive repeaters in both indoor and outdoor applications to change the field coverage by redirecting incident beams into desired directions with controllable power distributions. The design procedure includes a heuristic optimization method (genetic algorithms (GAs)) and full-wave electromagnetic analyses. For efficient and effective optimization of complex geometries, a multigrid approach is used. In this approach, the number of surface representation points is gradually increased in the course of an optimization to reach the best designs via a dynamic process from coarse shaping to fine tuning. Multilevel fast multipole algorithm (MLFMA) is used for the required full-wave electromagnetic analyses by reducing the computation time substantially without deteriorating the accuracy. The optimized geometries are fabricated using a three-dimensional (3D) printing method that enables low-cost and adaptive fabrication. The fabricated 3D prints are coated

with a low-cost conductive paint to obtain the final reflectors. Measurements are performed using a Naval Radio Lab arch (NRL arch) and in a free-space setup. The measured results are in good agreement with the simulations, demonstrating the success of both the design procedure and the designed reflectors as efficient 5G components. The designed reflectors provide solutions to the demand for low-cost and energy-efficient signal repeaters needed in 5G mm-wave mobile communication. Thanks to the adaptive design procedure and the use of 3D printing technology, the proposed types of reflectors can be realized and implemented for diverse configurations and alternative scenarios, where the distribution of the signal needs to be controlled in free space. Finally, the designs presented in this study have large bandwidths, while they are also scalable for alternative frequency ranges.

ÖZ

5G MM-DALGA UYGULAMALARI İÇİN VERİMLİ HÜZME ŞEKİLLENDİRİCİ YANSITICILARIN TASARIMLARI, ÜRETİMLERİ VE ÖLÇÜMLERİ

Karaova, Gökhan Çağlayan
Yüksek Lisans, Elektrik ve Elektronik Mühendisliği Bölümü
Tez Yöneticisi: Prof. Dr. Özgür Ergül

Mayıs 2021, 99 sayfa

Bu çalışmada, beşinci nesil milimetre dalga (5G mm-dalga) uygulamalarında kullanılmak üzere şekillendirilen pasif metal yansıtıcıların tasarımları için bir optimizasyon prosedürü ile tasarlanan yansıtıcıların üretim ve ölçümleri sunulmuştur. Bu yansıtıcılar, iç ve dış ortamda gelen ışınların (hüzmelerin) istenilen yönlere kontrol edilebilir güç dağılımlarıyla yönlendirilmesini, ve böylece kapsama alanının değiştirilmesini sağlayan pasif tekrarlayıcılar olarak kullanılabilmektedir. Tasarım prosedürü sezgisel bir optimizasyon yöntemini (genetik algoritma (GA)) ve tam dalga elektromanyetik analizleri içermektedir. Karmaşık yapıların verimli ve etkin optimizasyonları için çok katmanlı yaklaşım kullanılmıştır. Bu yaklaşımda, optimizasyon boyunca yüzeyler üzerindeki kontrol noktalarının kademeli olarak artırılmasıyla, kaba şekillendirmeden ince ayarlamalara varan dinamik işlemler sonucunda en iyi tasarımlara ulaşılabilmektedir. Tam dalga elektromanyetik çözücü olarak çok seviyeli hızlı çokkutup yöntemi (MLFMA) kullanılmıştır. Bu çözücü sayesinde sonuçların doğruluğundan ödün vermeden çözümler büyük oranda hızlandırılmıştır. Optimize edilmiş geometriler, düşük

maliyet ve uyarlanabilir üretim imkanı sağlayan üç boyutlu (3B) yazıcılarla gerçeklenmiştir. Üretilen geometriler, düşük maliyetli iletken boya ile kaplanarak yansıtıcılara dönüştürülmüşlerdir. Ölçümler Naval Radio Lab arch (NRL arch) ve boş uzay düzeneklerinde gerçekleştirilmiştir. Ölçümler ve benzetimler büyük oranda benzerlik göstermekte, elde edilen sonuçlar hem tasarım prosedürünün başarısını hem de tasarlanan yansıtıcıların verimli 5G bileşenleri olarak kullanılabileceklerini göstermektedir. Tasarlanan yansıtıcılar 5G mm-dalga uygulamalarında düşük maliyetli ve enerji verimi yüksek sinyal tekrarlayıcılarına duyulan ihtiyacı karşılayabilecek niteliktedir. Uyarlanabilir tasarım ve üretimleri sayesinde, bu çalışmada önerilen yansıtıcılar boş uzayda sinyal dağılımının kontrolünü gerektiren birçok uygulamada kullanılmak üzere gerçeklenebilir. Son olarak, bu çalışmada sunulan yansıtıcı yapılar, yüksek bant genişliğine sahip olup farklı frekanslarda kullanılmak üzere ölçeklenebilmektedir.

Anahtar Kelimeler: 5G sistemler, mm-dalga iletişim, genetik optimizasyon, hüzme şekillendirme, 3B üretim, MLFMA

to my beloved family

ACKNOWLEDGMENTS

TABLE OF CONTENTS

LIST OF FIGURES

FIGURES

xviii

LIST OF ALGORITHMS

ALGORITHMS

LIST OF TABLES

TABLES

LIST OF ABBREVIATIONS

2D	Two-Dimensional
3D	Three-Dimensional
4G	Fourth Generation
5G	Fifth Generation
CAD	Computer Aided Design
CDF	Cumulative Distribution Function
CFIE	Combined-Field Integral Equation
CG	Conjugate Gradient
CNC	Computer Numerical Control
CTF	Combined T formulation
EFIE	Electric-Field Integral Equation
EHF	Extremely High Frequency
FMM	Fast Multipole Method
Gbits	Gigabits
GHz	Gigahertz
GMRES	Generalized Minimal Residual
HETNETs	Heterogeneous Networks
JMCFIE	Electric-Magnetic Current Combined-Field Integral Equation
Mbits	Megabits
MCTF	Modified Combined T Formulation
MFIE	Magnetic-Field Integral Equation
MHz	Megahertz
MIMO	Multiple Input Multiple Output
MLFMA	Multilevel Fast Multipole Algorithm

mm-wave	Millimeter Wave
MoM	Method of Moments
NFV	Network Function Virtualization
NRL	Naval Research Lab
PEC	Perfect Electric Conductor
PLA	Polylactic Acid
PMCHWT	Poggio-Miller-Chang-Harrington-Wu-Tsai
PO	Physical Optics
RHS	Right Hand Side
SDN	Software Defined Network
SIE	Surface Integral Equation

CHAPTER 1

INTRODUCTION

1.1 Fifth-Generation Mobile Network
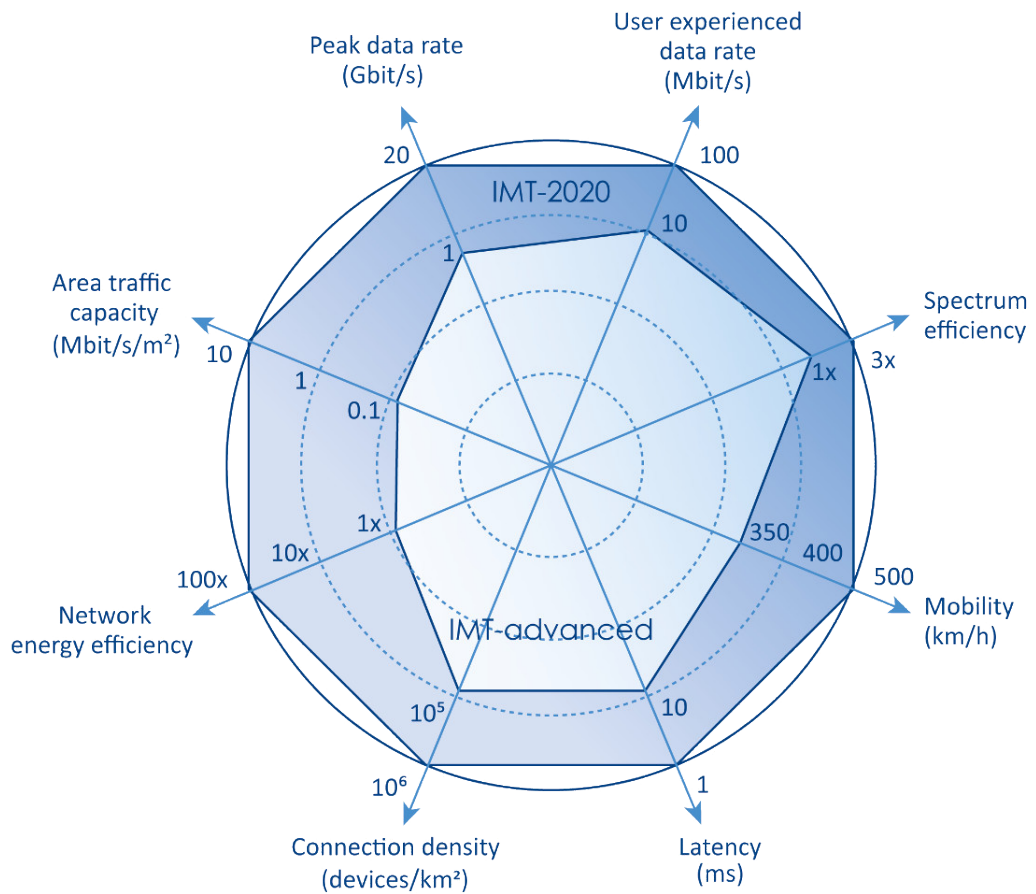
Figure 1.1: Planned improvements of 5G (IMT 2020) over 4G (IMT-advanced) [1].

The fifth generation (5G) of mobile network technology promises to meet the demands of wireless communication in the 2020s. Higher capacity, larger data usage,

lower latency, and higher speed in comparison to the former generation of mobile communication are some of the essential points 5G focuses on. According to the International Telecommunication Union (ITU-R M.2083) [1], 5G should be capable of providing 3x more spectrum efficiency, 100x more efficient networks, 20 Gbits/s peak data rate, and 1ms latency. Suggested improvements in different subjects over fourth-generation (4G) networks can be seen in Figure 1.1 [1].

Suggested improvements for 5G arise due to the needs of different application areas, such as factory automation [3], autonomous driving [4], and smart city applications [5,6]. The increasing use of the Internet, affordable access to information, and storage of larger data put further demands on the 5G technology. To respond such demands and reach the desired capabilities, the network should be highly flexible, integrable, and smart. This makes 5G a revolution rather than an improvement over 4G.

5G requires advanced technical improvements and solutions to problems in all layers of mobile communication. Millimeter waves (mm-waves) [2, 7], massive multiple-input multiple-output (massive MIMO) systems [7, 8], heterogeneous networks (Het-Nets) [7,9], software defined networks (SDN) [7,10], and network function virtualization (NFV) [7, 10] are some of the pioneering technologies and innovative solutions adapted in 5G, each contributing to different layers in mobile communications. At the physical layer, mm-waves and massive MIMO systems are the most prominent technological improvements.

1.1.1 Millimeter Waves

Millimeter waves (mm-waves) constitute the extremely high frequency (EHF) spectrum ranging from 30 GHz to 300 GHz, or wavelengths from 10 mm to 1 mm. In 5G, the mm-wave band is defined slightly differently, from around 20 GHz to 100 GHz. This spectrum is highly underdeveloped and can be used for mobile communication [7]. Specifically, using this spectrum enables us to enhance the capability of sending larger amounts of data at higher speeds thanks to wide unoccupied continuous bands of frequency. Currently, in 4G systems, the spectrum is limited to 6 GHz, while the bandwidth is limited to 20 MHz per user at maximum [2]. This limitation results in low data transmission rates even for today's requirements. For example,

with the 4G technology, the peak data rate is 100 Mbits/s, and with the 4G-Advanced or 4.5G, it is 300 Mbits/s. In 5G, the goal is to improve these figures to 10 Gbits/s to meet the aforementioned demands.

Even though using mm-waves offers a solution to bandwidth limitations, there are some challenges peculiar to this spectrum. First, there is a considerable amount of atmospheric attenuation present for mm-waves. For example, there are peaks of attenuation at 24 GHz and 60 GHz due to water molecules and oxygen as shown in Figure 1.2. Also, rain is substantially effective for the electromagnetic waves in the mm-wave spectrum.

In addition to atmospheric attenuation, mm-waves have higher path losses compared to the waves at lower frequencies used in mobile communications [2]. If the electrical sizes of the antennas are kept constant, each tenfold increase in the frequency leads to an additional 20 dB power loss on the receiver side.

However, those attenuations are tenable, particularly because applications using mm-waves in 5G mobile networks offer dense utilization of spaces and are developed mostly for short-distance communications [9]. Considering limiting standards on power radiations from wireless-network devices based on health regulations and communication standards, dense-utilization or short-distance communications become practical solutions for attenuation issues in free space. However, this approach of dense utilization results in high power consumption due to vastly increased numbers of devices needed to construct networks. Systems should be optimized and designed rigorously to use minimum numbers of devices and maximum numbers of passive devices, as much as possible, to reduce the power consumption.

Another issue of using mm-waves is related to their limited penetration into matter. These waves cannot propagate through buildings and objects as well as sub-6 GHz frequencies, which require solutions involving redirection of incident waves using relay and repeater structures to cover desired regions [11–13].
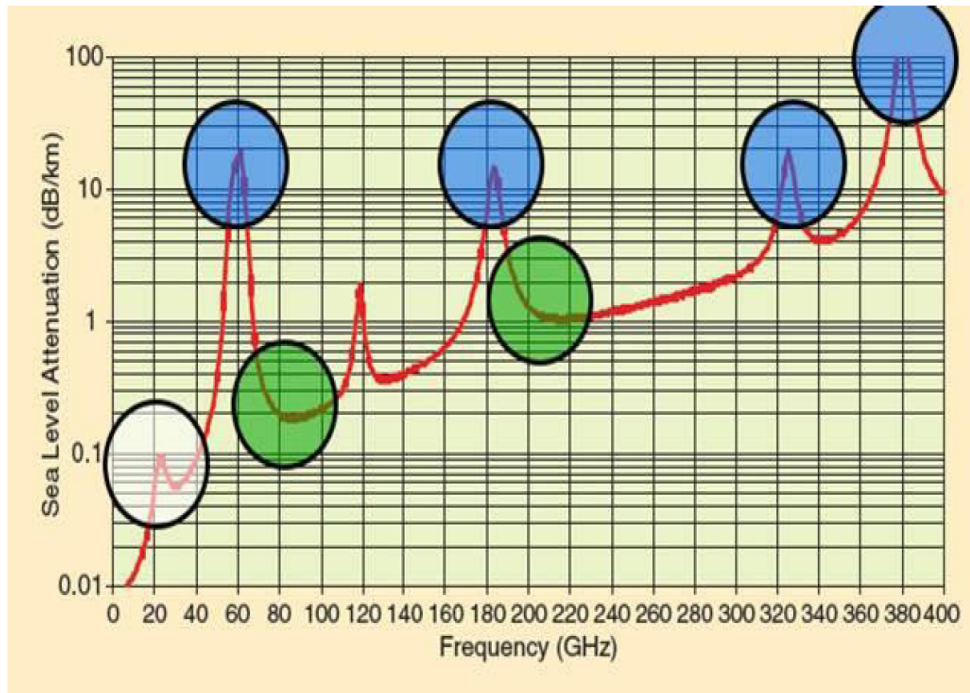
Figure 1.2: Atmospheric attenuation of mm-waves [2].

1.2 Reflecting Structures in Electromagnetics

Reflecting structures or reflectors in electromagnetics are devices that are used to redirect incident electromagnetic waves. Reflectors have been used since the early days of civilization in the form of mirrors, and they have been popular components in wireless communications, radar systems, and many other applications.

Reflecting structures in electromagnetics are employed in different forms, such as reflector antennas [14, 15] and passive repeaters [11]. Depending on the application, passive repeaters are made of metallic sheets, arrays, and metasurfaces. We note that, while most of the state-of-the-art reflectors are passive, we still prefer using the term "passive" to clearly distinguish the designed reflectors from emerging technologies on the use of active components for reflection mechanisms.

A reflector antenna usually consists of a source antenna and a reflecting structure. The function of the reflecting structure is to redirect, reshape, and/or enhance the incident waves from the source. Such reflectors can be in different forms, such as metallic surfaces and reflectarrays. Sources can differ as well; it can be a single structure, such as

4

a horn, patch, or lens, while it can be an array of antennas. Reflector antennas are preferred in communication systems since they can offer very high directivity compared to non-reflector designs, as well as increased control on the radiation characteristics.

Passive repeaters are usually made of metals or materials with high conductive properties. The most basic form of a passive reflector is a metallic sheet; but they can be in other alternative forms, such as optimized surfaces and parabola. In some applications, repeaters can also be built from arrays of unit cells, such as metasurfaces [16].

Both reflector antennas and passive repeaters may be supported by mount systems (gimbals). An active mount system can be used to physically rotate the reflecting structure, if desired. An incoming wave onto a reflector structure usually has a plane-wave characteristic, since the source is far away from the structure. Figure 1.3 presents the photographs of a passive repeater (left) and a reflector antenna (right).

1.2.1 Reflector Shaping

Performance of passive reflecting surfaces can be increased by introducing surface optimization methods [15–19]. A passive metallic reflector surface can be shaped carefully to enhance coverage and obtain constant power distribution at desired locations, or it can be shaped to block waves propagating in certain directions to reduce losses. Also, a passive reflector antenna surface can be optimized to reduce spillover losses, blockages, beam squints, or sidelobes, as well as to increase gain and aperture efficiency.

1.3 Reflector Shaping for 5G Applications

As discussed so far, reflector antennas and passive reflecting structures can be used in 5G mobile communication systems to achieve desired operational characteristics. Reflector antennas can be used in base stations to enhance coverage performance in mm-wave applications, by increasing directivity and/or reducing sidelobes. Passive reflecting surfaces can be used in indoor and outdoor mm-wave applications to enhance coverage by redirecting fields and increasing capacity, without requiring additional power consumption.

Figure 1.3: A passive repeater (left) and a reflector antenna (right).

Reflector shaping techniques can be used in 5G mm-wave applications to further increase the usability of reflecting structures. First, the reflector shaping technique can be applied to design passive reflectors that can be used as high-performance adaptive passive repeaters for indoor or outdoor applications. In mm-wave communication, propagation through physical obstacles is an issue, and redirecting fields around such obstacles is necessary for reliable communication. Rather than using active systems, passive repeaters are preferred since they do not require any power. Shaping can be used to increase the directivity of such repeaters or to tailor reflected fields for specific applications. For example, using shaped reflectors, an incoming field can be redirected over a specified set of angles with constant power distribution, leading to reliable communication. Similarly, the intensity of an incoming field can be reduced down to a certain level to decrease communication overheads without requiring any active device.

Second, shaping techniques can be used for reflector antennas. They can be particularly useful for a base station antenna consisting of a reflector antenna and a source array. These kinds of antenna structures can be useful in a plethora of applications, such as MIMO, sectorization, and mm-wave communication. Shaping techniques can be applied to reflector parts to reduce sidelobes, increase directivity, reduce co-

channel interference during sectorization, and adjust power levels radiating from the base station in different directions, which further improve the signal-to-noise ratio and enable reliable communications.

This thesis is devoted to the design and optimization of reflector surfaces as passive repeaters to be used in mm-wave applications. In addition to the rigorous design of effective surfaces, a low-cost fabrication technique based on three-dimensional (3D) printing and a coating technique is presented to realize them.

A discussed in the next chapter, reflector shaping is performed by employing genetic algorithms (GAs). The developed GA implementation is used to find optimal deformed surfaces, starting from a square planar surface with zero thickness. Throughout an optimization, full-wave electromagnetic analyses are conducted by the multilevel fast multipole algorithm (MLFMA). The results of simulations are studied in multiple perspectives, e.g., coverage performance, bandwidth, and sensitivity.

The presented novel procedure involving the design, optimization, and fabrication of reflecting structures is not limited to the examples included in this thesis. The target problem can be coverage enhancement in a specific space of a room, achieving uniform power distribution throughout a hallway, or it can be related to achieve communication requirements of two base stations that are not in the line of sight of each other. The presented technique is highly adaptive; so any problem involving a design of a passive reflector can be attempted with minor modifications on the overall procedure.

In Chapter 2, the shaping technique for reflecting structures based on GAs is presented, including the electromagnetic tool required for analyses of candidate designs. In Chapter 3, sample optimization and simulation results are presented and discussed. Fabrication and measurement of selected structures are presented together with comparisons with simulations in Chapter 4. Finally, in Chapter 5, the conclusions are drawn with future aspects of this study.

CHAPTER 2

SHAPING TECHNIQUE FOR PASSIVE REFLECTOR STRUCTURES

In this chapter, the reflector shaping technique involving a combination of GAs and an electromagnetic solver is presented.

Electromagnetic design procedures often require finding optimal shapes and topologies that provide the desired electromagnetic characteristics and responses. Unsurprisingly, optimization tools have become major components in the design of many electronic devices at radio, microwave, THz, and optical frequencies. In the literature, one can find a plethora of applications, including antennas [20, 21], reflecting surfaces [22–24], frequency-selective surfaces [25], metamaterials [26], optical and photonic components [27–30], where the structures are designed via optimization to satisfy the desired absorption, radiation, reflection, scattering, and transmission properties. In some cases, it is possible to transform the original problem into a simplified form, such as a network of lumped elements, which can be easier to optimize at an analytical level [31]. Also, topological optimization involving relatively small perturbations can efficiently be handled by using gradient-based tools, where the kernel solution methods are modified to incorporate the gradient operation on the electromagnetic interactions. On the other side, nature-inspired algorithms, such as particle swarm optimization methods [32, 33] and GAs [34, 35], provide a great freedom on the fitness functions, including those for multipurpose applications. These heuristic algorithms can easily be combined externally with electromagnetic solvers, while, as a drawback, they need relatively large numbers of trials for satisfactory optimization results.

In this study, a multigrid optimization strategy is applied to design passive metallic reflectors with corrugated shapes for 5G mm-wave mobile communications. The

strategy is based on using GAs at multiple grids and shaping the metal sheets, starting from coarse details to fine tunings. By employing MLFMA to analyze the electromagnetic problems corresponding to optimization trials, we obtain accurately designed reflectors that provide the desired reflection characteristics with high performances. The designed reflectors are also resistant to fabrication errors with suitable corrugations and simplified reflection mechanisms thanks to the usage of adaptive Bézier surfaces.

2.1 Genetic Algorithms

GAs are heuristic algorithms that can provide remarkably successful solutions to complex optimization problems [34–36]. They are well-known and widely used for electromagnetic problems, and have been used in surface optimizations [17, 22, 26], antenna array optimizations [21], and particle array optimizations [29, 30].

In general, GAs are based on the theory of evolution in nature. An optimization is performed via biologically-inspired operators, and the aim is either decreasing a predefined cost value or increasing a predefined fitness value by approximating the solution.

An operation diagram for a GA implementation is described in Figure 2.1. There is an initial set that is a randomly generated pool of candidate solutions, called population. The individuals in the set are analyzed to obtain performance metrics according to the fitness function. As a result, cost or fitness values of the individuals are found. In the decision step, existence of a solution that satisfies the predefined optimization goal is checked. This goal can be a metric of performance (cost or fitness value) or the number of generations created so far during the optimization. If the goal is not met, the next step is to apply reproduction techniques to create the next generation of individuals. Reproduction techniques might be crossover, mutation, selection, and other methods inspired by the theory of evolution. This newly generated set is forwarded to the analysis step so that the process is iterated until decision criteria are met and a final design is reached. In the following section, steps of the GA implementation are presented in more detail from the perspective of optimization problems in this study.
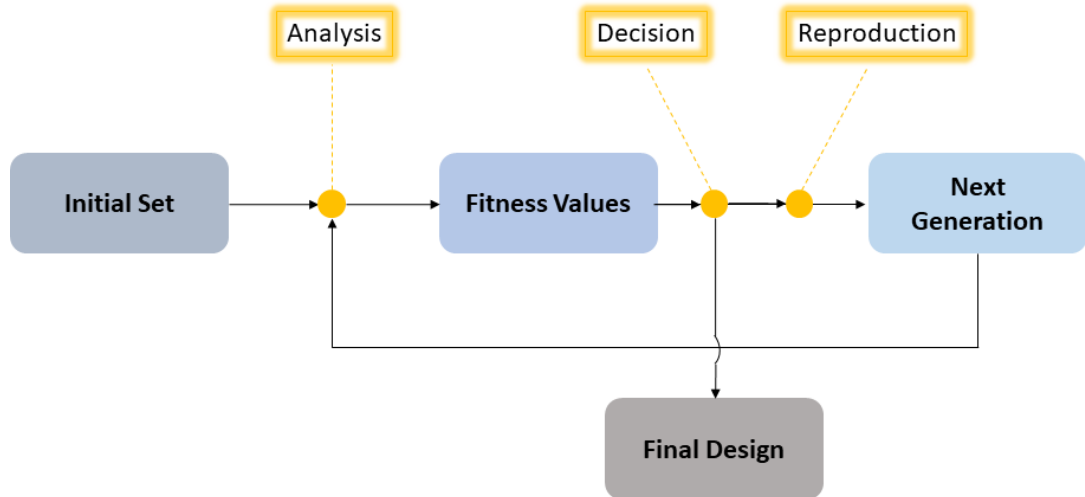
Figure 2.1: Operation diagram of the GA implementation.

2.1.1 Individuals

Individuals are candidate solutions; as evolution (optimization) proceeds, they represent better solutions to the problem. In our optimization attempts, the number of individuals is set to 20 without any change throughout generations. This number is selected for the necessary pool size to cover a large portion of the solution space with affordable computation time. Based on our initial experiments, using smaller or larger numbers of individuals result in insufficient or inefficient optimization results, as small numbers of individuals cannot trace the optimization space sufficiently, while large numbers of individuals lead to long processing times without significant improvements on the quality of the final results.

Individuals are defined by their chromosome representations. Each individual has a chromosome containing a fixed number of genes. In our problems, these genes correspond to the values that represent control point positions, which are used to define the shape of the surface. Hence, throughout an optimization, genes and the control points that they represent evolve to generate better solutions to the problem.

GAs can be categorized by their gene definitions. Specifically, genes can be defined either by discrete or continuous values. Representing genes by discrete numbers of values reduces the search space by discretizing the optimization space. For example,

a gene can be composed of 4 bits or 8 bits, which correspond to the representation of the gene value by 16 or 256 discrete points, respectively. Continuous-value genes are defined directly by real numbers, which, in theory, have infinitely many values. In our problems, the height of a control point on a given surface is directly used as a gene represented by maximum three digits. This representation is sufficient for the range of control point values (heights of the control points over the initial surface defined on two-dimensional (2D) plane) that is defined as $\pm 2\lambda$.

2.1.1.1 Surface Representation

In an optimization problem, the initial surface is a rectangular sheet and it is bent in the third dimension during the optimization. Such a surface should be defined in terms of discrete points (nodes) and there can be different approaches, as described below.

Representation Using Independent Mesh Nodes: A trivial method to represent a surface is to directly use nodes on the discretization grid with independently assigned heights for each node. In a computer simulation problem, the geometry is already discretized into smaller pieces for numerical solutions. In this study using surface integral equations (SIE) and MLFMA, the given geometry surface is discretized with small triangles, each of which is represented by three nodes. If these discretization nodes are used directly to represent deformed surfaces, the resulting geometries are highly corrugated. This obviously makes the fabrication a challenging task, even when the optimization attempts are successful. In addition, in a full-wave electromagnetic solver, such as MLFMA, geometries should be triangulated using small elements ($\lambda/10$ edge size), which result in a lot of points to be represented by individuals (chromosomes), further giving rise to poor optimization performance. An example to a surface represented by independent nodes can be seen in Figure 2.2.

12
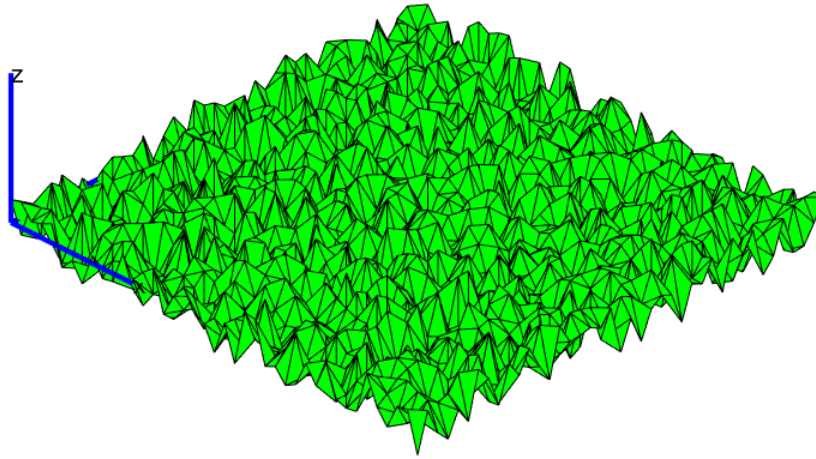
Figure 2.2: Surface shaping using independent nodes.

Representation Using Control Points: Alternatively, a surface can be represented by control points defined independently of the mesh elements. The number of control points can be selected to be much smaller than the number of discretization nodes on the geometry, allowing a shorter chromosome definition. This method was used in [22] together with a multigrid technique that changes the number of control points on the surface throughout an optimization, which can improve the results substantially compared to the independent optimization of each node.

- Bézier Curves and Surfaces

  One approach to efficiently employ individual control points on a surface is to use Bézier curves and surfaces. Developed by the French engineer Pierre Bézier, the Bézier curve representation is a parametric curve creation method based on defining control points on a given surface. This method provides smooth transitions on the surface and it is mathematically defined as

$$p(u) = \sum_{i=0}^{n} B_i^n(u) P_i. \tag{2.1}$$

13

Similarly, for a Bézier surface, we have

$$p(u,v) = \sum_{i=0}^{n}\sum_{j=0}^{m} B_i^n(u)B_j^m(v)P_{ij} \qquad (2.2)$$

$$B_i^n(u) = \binom{n}{i}u^i(1-u)^{n-i}. \qquad (2.3)$$

In equations 2.2 and 2.3, u,v represent the parametric axes on the surface, m, n are the indices of the control points on the surface, P is the position of each control point defined on the u-v axes, and p is the height of a desired point, which corresponds to a node of the meshed geometry in this study. In addition, B_i^n defined in 2.3 is known as Bernstein polynomials. In this method, the size of the geometry should be between 0 and 1 units in both u and v directions. Hence, while shaping a surface in this study, the surface is first scaled into these limits, control points are defined, the geometry is shaped, and then it is re-scaled to return back to original dimensions. An example surface generated by this method can be seen in Figure 2.3, where $m = 7$ and $n = 7$, while u and v correspond to the Cartesian x and y, respectively.

Throughout an optimization in this study, u and v are selected equally between 4 and 12.
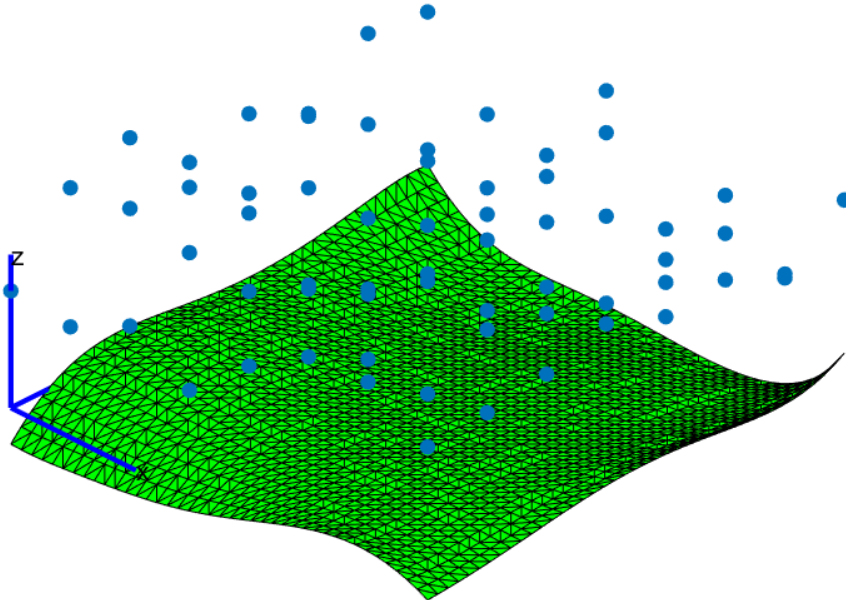
Figure 2.3: Optimization nodes defined by using Bézier control points (blue) and a shaped surface based on these control points (green).

- Multigrid Bézier Surfaces

  In [22], the multigrid shaping method is proposed to efficiently optimize surfaces in a controllable manner by gradually increasing chromosome lengths. In this study, it is further developed and adapted to Bézier representations of surfaces. For a Bézier curve, there is a concept called degree raising, which corresponds to the increase of the number of control points representing a curve. This method is mathematically defined as

  $$Q_i = \left(\frac{i}{n+1}\right)P_{i-1} + \left(1 - \frac{n+1-i}{n+1}\right)P_i, \tag{2.4}$$

  where in $i = 0, ..., n+1$, and Q and P are the increased and original numbers of control points. This method can be applied to Bézier surfaces on considering both axes as

  $$\begin{aligned}
  Q_{i,j} = &\left(\frac{i}{n+1}\right)\left(\frac{j}{n+1}\right)P_{i-1,j-1} \\
  &+ \left(\frac{i}{n+1}\right)\left(\frac{n+1-j}{n+1}\right)P_{i-1,j} \\
  &+ \left(\frac{n+1-i}{n+1}\right)\left(\frac{j}{n+1}\right)P_{i,j-1} \\
  &+ \left(\frac{n+1-i}{n+1}\right)\left(\frac{n+1-j}{n+1}\right)P_{i,j}.
  \end{aligned} \tag{2.5}$$

  During an optimization, the number of control points is increased using equation 2.5 every 40 generations. This method lets increasingly refined grids be employed at different levels such that reflectors are designed progressively from coarse details to fine tunings. Hence, this approach enables more controllable exploration of the solution space, while, as in all heuristic algorithms, the developed implementation does not guarantee a globally optimal solution.

  In the context of this study, obtaining a smooth surface is important since its fabrication can be less complicated. Also, the number of control points to define a surface is an important figure for an optimization since each point contributes to the length of the chromosomes. Choosing a very large number of control points leads to huge optimization spaces that are very difficult to explore, while small numbers of points might result in stagnations in very limited parts of the space.

15

2.1.2   Initialization

In GAs, an initial population is a set of randomly generated individuals. In this study, initial individuals are randomly deformed and bent square plates, where all deformations are described by control points and they remain in predefined limits.

2.1.3   Fitness or Cost Function

Fitness or cost function is the mathematical definition of the optimization problem. GA operations are performed to generate improved individuals such that the optimization increases the fitness (for a fitness function) or decreases the cost (for a cost function) as the generations continue. The evaluation of the fitness function is usually a single number defining the performances of individuals and the overall optimization. However, this single number can be a combination of various parameters, such as power, beamwidth, cross-polarization level, or another metric for an electromagnetic optimization problem. Thus, a GA implementation can be considered as a multi-variable optimization tool.

To find the fitness value for an individual, an electromagnetic analysis is performed to obtain the reflected fields from the reflector represented by the individual. The electromagnetic analysis step is performed by MLFMA, which will be covered later in this chapter. The fields reflected from a reflector are computed in the far-zone, and the selection of the far-zone directions is critical in terms of the optimization.

In this study, we aim to generate balanced distributions of fields values within predefined limits in certain directions. Specifically, optimization is used to generate surfaces such that power values in selected directions are equal to a predefined value. The predefined value is based on the reflection characteristics of the original (flat) surface, which roughly provide the capabilities of the reflector and achievable reflection characteristics.The fitness function for the optimization problem is defined as

follows:

Algorithm 1: Fitness Function Definition

---

for *Every Chosen Far-Field Point* **do**

    Fitness Value at Point

    $= |PredefinedFieldValue - MeasuredFieldValue|$;

end

Fitness Value $= -\sum$(Fitness Value at Point);

Besides the fitness function itself, the number of observation points in the far-zone should be carefully chosen to ensure that the optimization process can provide desired results. Choosing a large number of points can make an optimization unsuccessful since reflection characteristics in a wide range of directions cannot be a represented by a single fitness value. On the other hand, choosing a few points causes problems since reflection characteristics may not be formulated by the fitness function. In this study, different far-field sampling methods are considered in accordance with various optimization purposes, as described below.

- Far-field Points on a Single Cut

  Far-field points can be selected on a single cut corresponding to a Cartesian plane. Selected (but not all) directions on the cut can be used to compute the reflected fields and fitness values. Choosing a single plane is preferred if the problem requires field control only on a single plane. In such a case, since the number of samples is limited, each point typically has a significant contribution in the fitness value. Obviously, this approach does not provide any control on the reflected waves in 3D space, even for the directions in the vicinity of the samples on the other cuts. An example to a representation of far-field points on a single plane is shown in Figure 2.4.

- Far-field Points on a Spherical Surface

  Far-field points can also be chosen on a sphere in a 3D manner. This approach can provide strong reflections toward a 3D far-field region rather than a set of directions on a single plane. However, representing a 3D region can result in a large number of points that potentially degrades the optimization performance. As a solution, sampling representing the 3D area (whether it is a half space,

17

quarter space, 1/8 space, or even smaller) can be sparsed. A representative 3D far-field selection is depicted in Figure 2.5.
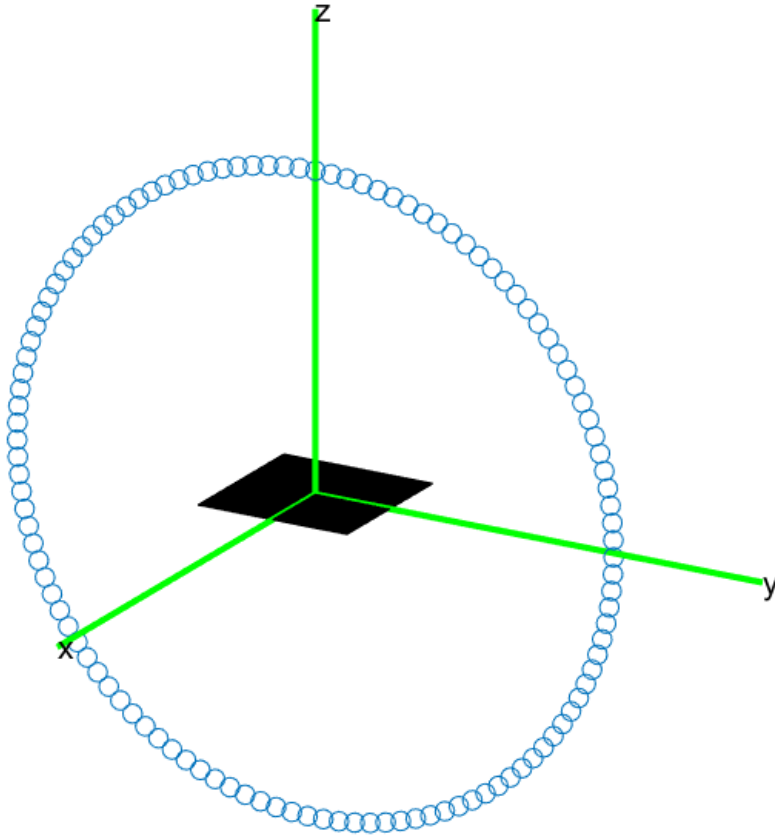
Figure 2.4: Far-field points (blue) on a single plane.

2.1.4 Reproduction Techniques

Reproduction techniques are used to create subsequent of individuals in GAs. Evolutionary processes such as elitism, crossover, and mutation are explained below. An adaptive selection of reproduction rates, which is a novel approach in GA implementations, is also explained.
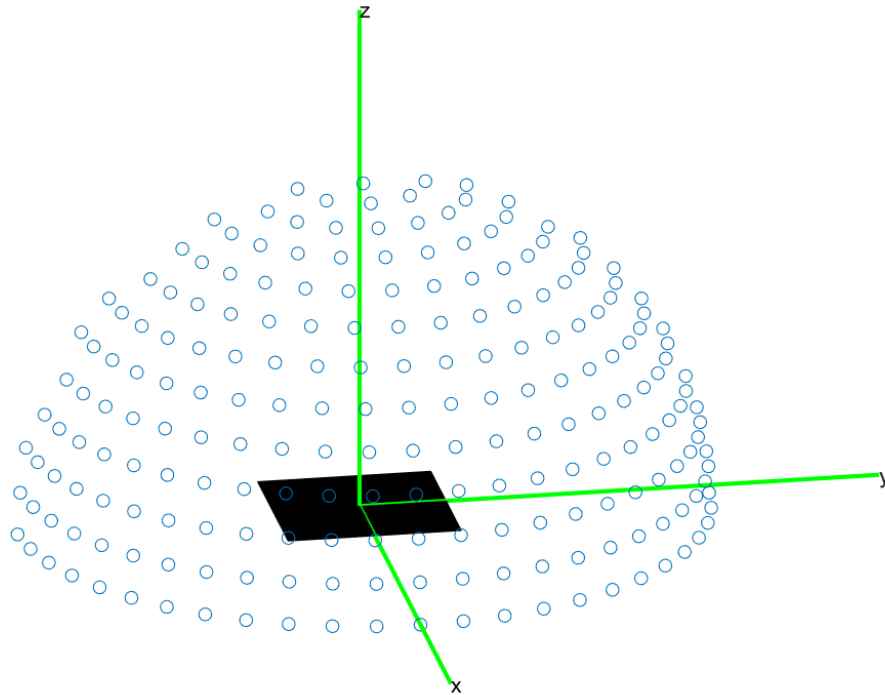
Figure 2.5: Far-field points (blue) on a quarter sphere.

2.1.4.1 Selection and Elitism

After all electromagnetic simulations are carried out for a generation, the individuals are sorted from best to worst considering their performances. Then two individuals with the highest fitness values are transferred to the next generation unchanged. This operation is called elitism, which is performed to ensure that the fitness value in a generation is always equal to or larger than the fitness value in the previous generation. Also, two new individuals of the next generation are generated from these two parents via crossover and mutation with a very low probability rate. Elitism provides only four individuals of the new generation. For the others, selection is an operation to generate the individuals in the next generation. Specifically, crossover and mutation operations are applied on the selected individuals (parents) to generate new individuals. In general, parents are selected among those with higher fitness values to increase the overall quality of the next generation. At the same time, for the selection of the individuals with sufficient potentials, we apply the roulette wheel approach to randomize the overall process.

2.1.4.2 Crossover

Crossover is the process where two individuals exchange their genes (corresponding to geometric control points in this study). This operation enables new individuals with new chromosomes, which possibly represent more successful trials than the parents.

2.1.4.3 Mutation

Mutation is randomization of a gene (or genes) of a chromosome. In our GA implementation, there are two mutation definitions, i.e., moderate mutation and heavy mutation. Moderate mutations are applied to offsprings of relatively successful individuals, while heavy mutations are well-suited to dramatically modify unsuccessful individuals for the variation of the generation.

2.1.4.4 Adaptive Reproduction Rates

Reproduction techniques described above provide necessary randomization and variation for GAs to succeed. However, at some point throughout generations, it is common for an optimization to converge to a local minimum, and stagnate without a better result for a long period of time. In such cases, what we call an adaptive reproduction rate is an effective technique to obtain better results. This method identifies the number of consecutive generations where no improvement occurs on the fitness value of the pool (the best individual). Then, if a given number of generations have similar fitness values, it introduces a large discrepancy in the reproduction rates; specifically, it greatly increases the probability of crossover and mutation on individuals for a single generation. Elitism is still applied in this approach, meaning that the population maintains its best individual from the previous generations. However, most of the offsprings are significantly different from their parents, leading to sampling of new unexplored regions in the optimization space. Using adaptive reproduction rates can provide an essential assistance in critical cases, where GAs stagnate and the restart of the optimization is time consuming.

2.1.5 Decision

Various decision criteria are used to decide whether the optimization should be terminated or continued. The decision can be based on either reaching a predefined fitness value or completing a number of generations. In our optimization problems, we always terminate an optimization within 200 generations. Based on our experience, smaller numbers of generations provide premature results, while larger numbers do not provide better results even when the fitness criteria are not satisfied.

In this section, GA is presented with important operations and parameters. Some modifications to improve the performance of GAs for the targeted problems are also described. In the following, we present the analysis step, i.e., solutions of electromagnetic problems.

2.2 Solutions of Electromagnetic Problems

An optimization of a reflector surface requires many electromagnetic analyses, and MLFMA is used for this purpose in this study. Although it is based on the method of moments (MoM), MLFMA is an efficient algorithm both in terms of memory and computation time. MLFMA performs a full-wave analysis of the given problem using boundary conditions and integro-differential (SIE) forms of Maxwell's equations on the surface of the object. By using MLFMA, current distributions on the surface of the object can be found, enabling the computation of near-zone or far-zone fields via radiation integrals.

To be used within MoM/MLFMA solutions, there are different SIEs derived from Maxwell's equations, such as the magnetic-field integral equation (MFIE), electric-field integral equation (EFIE), combined-field integral equation (CFIE), and potential integral equations (PIEs) to analyze perfect electric conductors (PECs). There are also, JM combined-field integral equation (JMCFIE), combined tangential formulation (CTF), modified combined tangential formulation (MCTF), and many other alternatives for dielectric problems.

In this study, considering the range of frequencies, the reflector surfaces are represented as PEC sheets. This approach is used since PEC problems are solved more

21

efficiently compared to dielectric problems (e.g,, dielectric problems require larger numbers of unknowns), and PEC approximation is viable for relatively large metallic objects at mm-wave frequencies. In a single optimization process, a total of 4000 solutions are required considering 20 individuals and 200 generations; so the efficiency of simulations is crucial to obtain optimization results in reasonable processing times.

Since the reflectors are modeled as PEC objects, MFIE, EFIE, CFIE, and PIEs are candidate integral equations that we can use. However, MFIE and other equations based on MFIE (in this context, CFIE) are applicable to close surfaces, while our reflectors are represented as 2D sheets (an open surface). On the other hand, PIEs are more suitable for accurate solutions of low-frequency problems in general. Thus, EFIE is chosen and used in this work.

2.2.1 Electric-Field Integral Equation (EFIE)

Maxwell's equations can be written as

$$\nabla \times \boldsymbol{E}(\boldsymbol{r}, t) = -\frac{\partial \boldsymbol{B}(\boldsymbol{r}, t)}{\partial t} \tag{2.6}$$

$$\nabla \times \boldsymbol{H}(\boldsymbol{r}, t) = \frac{\partial \boldsymbol{D}(\boldsymbol{r}, t)}{\partial t} + \boldsymbol{J}(\boldsymbol{r}, t) \tag{2.7}$$

$$\nabla \cdot \boldsymbol{D}(\boldsymbol{r}, t) = \rho_e(\boldsymbol{r}, t) \tag{2.8}$$

$$\nabla \cdot \boldsymbol{B}(\boldsymbol{r}, t) = 0. \tag{2.9}$$

In these equations, $\boldsymbol{E}$ is the electric field intensity, $\boldsymbol{H}$ is the magnetic field intensity, $\boldsymbol{D}$ is the electric flux density, and $\boldsymbol{B}$ is the magnetic flux density. We note that equations 2.6-2.9 represent Faraday's law, Ampere's law, Gauss' law, and Gauss' law of magnetism, respectively, and they are written in the absence of magnetic sources. As it is well known, Maxwell's equations are connected to each other with the help of physical constraints, such as the continuity equation. If one evaluates the divergence of the Ampere's law

$$\nabla \cdot \nabla \times \boldsymbol{H}(\boldsymbol{r}, t) = \nabla \cdot \frac{\partial \boldsymbol{D}(\boldsymbol{r}, t)}{\partial t} + \nabla \cdot \boldsymbol{J}(\boldsymbol{r}, t), \tag{2.10}$$

we obtain

$$0 = \frac{\partial \nabla \cdot \boldsymbol{D}(\boldsymbol{r}, t)}{\partial t} + \nabla \cdot \boldsymbol{J}(\boldsymbol{r}, t) \tag{2.11}$$

22

since the divergence of a curl is identically zero. Then, if equation 2.11 is inserted into equation 2.8, the continuity equation is reached as

$$\nabla \cdot \boldsymbol{J}(\boldsymbol{r}, t) = -\frac{\partial \rho_e(\boldsymbol{r}, t)}{\partial t}. \tag{2.12}$$

Alternative practices can be used to demonstrate the interrelationship between Maxwell equations.

If the medium is linear and isotropic, constitutive relations can be written as

$$\boldsymbol{D}(\boldsymbol{r}, t) = \epsilon \boldsymbol{E}(\boldsymbol{r}, t) \tag{2.13}$$

$$\boldsymbol{B}(\boldsymbol{r}, t) = \mu \boldsymbol{H}(\boldsymbol{r}, t). \tag{2.14}$$

Furthermore, Maxwell's equations can be written in phasor domain using $e^{-i\omega t}$ time convention as

$$\nabla \times \boldsymbol{E}(\boldsymbol{r}) = i\omega\mu \boldsymbol{H}(\boldsymbol{r}) \tag{2.15}$$

$$\nabla \times \boldsymbol{H}(\boldsymbol{r}) = -i\omega\mu \boldsymbol{E}(\boldsymbol{r}) + \boldsymbol{J}(\boldsymbol{r}) \tag{2.16}$$

$$\nabla \cdot \boldsymbol{E}(\boldsymbol{r}) = \frac{\rho_e(\boldsymbol{r})}{\epsilon} \tag{2.17}$$

$$\nabla \cdot \boldsymbol{H}(\boldsymbol{r}) = 0. \tag{2.18}$$

Starting from these forms in the phasor domain, the curl of Faraday's law leads to

$$\nabla \times \nabla \times \boldsymbol{E}(\boldsymbol{r}) = i\omega\mu \nabla \times \boldsymbol{H}(\boldsymbol{r}) \tag{2.19}$$

$$\nabla\nabla \cdot \boldsymbol{E}(\boldsymbol{r}) - \nabla^2 \boldsymbol{E}(\boldsymbol{r}) = i\omega\mu(-i\omega\epsilon \boldsymbol{E}(\boldsymbol{r}) + \boldsymbol{J}(\boldsymbol{r})) \tag{2.20}$$

$$\frac{1}{\epsilon}\nabla\rho_e(\boldsymbol{r}) - \nabla^2 \boldsymbol{E}(\boldsymbol{r}) = \omega^2\mu\epsilon \boldsymbol{E}(\boldsymbol{r}) + i\omega\mu \boldsymbol{J}(\boldsymbol{r}) \tag{2.21}$$

$$\nabla^2 \boldsymbol{E}(\boldsymbol{r}) + k^2 \boldsymbol{E}(\boldsymbol{r}) = -i\omega\mu \boldsymbol{J}(\boldsymbol{r}) + \frac{1}{\epsilon}\nabla\rho_e(\boldsymbol{r}), \tag{2.22}$$

where $k = \omega\sqrt{\mu\epsilon}$ is the wavenumber. The Helmholtz equation in 2.22 shows how the electric field intensity is related to sources. However, instead of solving this equation, an alternative approach based on potentials is more commonly used.

As indicated in equation 2.9, the magnetic flux density is solenoidal; hence and it can be defined in terms of a vector potential as

$$\boldsymbol{B}(\boldsymbol{r}) = \nabla \times \boldsymbol{A}(\boldsymbol{r}). \tag{2.23}$$

23

Using equations 2.14 and 2.15,

$$\frac{\nabla \times \boldsymbol{E}(\boldsymbol{r})}{i\omega} = \nabla \times \boldsymbol{A}(\boldsymbol{r}) \tag{2.24}$$

$$\nabla \times (\boldsymbol{E}(\boldsymbol{r}) - i\omega\boldsymbol{A}(\boldsymbol{r})) = 0. \tag{2.25}$$

The gradient of a scalar field can be assigned to the right-hand side (RHS) of the equation since it represents an irrotational vector. Then, we arrive at

$$\boldsymbol{E}(\boldsymbol{r}) - i\omega\boldsymbol{A}(\boldsymbol{r}) = -\nabla\phi(\boldsymbol{r}) \tag{2.26}$$

$$\boldsymbol{E}(\boldsymbol{r}) = -\nabla\phi(\boldsymbol{r}) + i\omega\boldsymbol{A}(\boldsymbol{r}), \tag{2.27}$$

where $\boldsymbol{E}$ is defined in terms of potentials. For unique representations, Lorenz gauge can be defined between the two potentials as

$$\nabla \cdot \boldsymbol{A}(\boldsymbol{r}) = i\omega\mu\phi(\boldsymbol{r}). \tag{2.28}$$

Then, Helmholtz equations for the potentials can be derived as

$$\nabla^2 \boldsymbol{A}(\boldsymbol{r}) + k^2 \boldsymbol{A}(\boldsymbol{r}) = -\mu\boldsymbol{J}(\boldsymbol{r}) \tag{2.29}$$

$$\nabla^2 \phi(\boldsymbol{r}) + k^2 \phi(\boldsymbol{r}) = -\frac{1}{\epsilon}\rho_e(\boldsymbol{r}), \tag{2.30}$$

where the electric current density and electric charge density are separated into two equations. The Helmholtz equations in 2.29 and 2.30 can be solved for a point source, leading to the homogeneous-space Green's function. It can be written as

$$g(\boldsymbol{r}, \boldsymbol{r}') = \frac{e^{ik|\boldsymbol{r}-\boldsymbol{r}'|}}{4\pi|\boldsymbol{r}-\boldsymbol{r}'|}, \tag{2.31}$$

where $\boldsymbol{r}$, $\boldsymbol{r}'$ are observation and source points, respectively. Using the Green's function, the solutions to Helmholtz equations for the potentials can be derived as

$$\phi(\boldsymbol{r}) = \frac{1}{\epsilon} \int d\boldsymbol{r}' g(\boldsymbol{r}, \boldsymbol{r}')\rho_e(\boldsymbol{r}') \tag{2.32}$$

$$\boldsymbol{A}(\boldsymbol{r}) = \mu \int d\boldsymbol{r}' g(\boldsymbol{r}, \boldsymbol{r}')\boldsymbol{J}(\boldsymbol{r}'). \tag{2.33}$$

Finally, the electric field intensity can be derived by inserting 2.32 and 2.33 into 2.26 as

$$\boldsymbol{E}(\boldsymbol{r}) = ik\eta \int d\boldsymbol{r}' \big[\boldsymbol{J}(\boldsymbol{r}') + \frac{1}{k^2}\nabla' \cdot \boldsymbol{J}(\boldsymbol{r}')\nabla\big] g(\boldsymbol{r}, \boldsymbol{r}'). \tag{2.34}$$

This is the main equation to form EFIE that we discretize to analyze reflector problems in this study.

In the reflector problem, we often compute far-zone field, i.e., the electric field intensity in various directions away from the reflector. For this purpose, the Green's function and its gradient can be approximated as

$$g(\boldsymbol{r}, \boldsymbol{r}') \approx \frac{e^{ik\boldsymbol{r}}}{4\pi\boldsymbol{r}} e^{-ik\hat{\boldsymbol{r}}\cdot\boldsymbol{r}'} \tag{2.35}$$

$$\nabla g(\boldsymbol{r}, \boldsymbol{r}') \approx ik\hat{\boldsymbol{r}} \frac{e^{ik\boldsymbol{r}}}{4\pi\boldsymbol{r}} e^{-ik\hat{\boldsymbol{r}}\cdot\boldsymbol{r}'}. \tag{2.36}$$

Using these approximations, the electric-field intensity can be written as

$$\boldsymbol{E}(\boldsymbol{r}) \approx ik\eta \frac{e^{ikr}}{4\pi r} \left\{ \int d\boldsymbol{r}' \left[\boldsymbol{J}(\boldsymbol{r}') e^{-ik\hat{\boldsymbol{r}}\cdot\boldsymbol{r}'} + \hat{\boldsymbol{r}} \frac{ik}{k^2} \nabla' \cdot \boldsymbol{J}(\boldsymbol{r}') e^{-ik\hat{\boldsymbol{r}}\cdot\boldsymbol{r}'} \right] \right\}. \tag{2.37}$$

Using the divergence theorem, the second term on the RHS can be manipulated as

$$\int d\boldsymbol{r}' \nabla' \cdot \boldsymbol{J}(\boldsymbol{r}') e^{-ik\hat{\boldsymbol{r}}\cdot\boldsymbol{r}'} = -\int d\boldsymbol{r}' \boldsymbol{J}(\boldsymbol{r}') \cdot \nabla' e^{-ik\hat{\boldsymbol{r}}\cdot\boldsymbol{r}'}$$
$$= ik\hat{\boldsymbol{r}} \cdot \int d\boldsymbol{r}' \boldsymbol{J}(\boldsymbol{r}') e^{-ik\hat{\boldsymbol{r}}\cdot\boldsymbol{r}'}. \tag{2.38}$$

Then, we finally arrive at the expression for the electric field intensity in the far zone as

$$\boldsymbol{E}(\boldsymbol{r}) = ik\eta \frac{e^{ik\boldsymbol{r}}}{4\pi\boldsymbol{r}} \left\{ \int d\boldsymbol{r}' \left[\boldsymbol{J}(\boldsymbol{r}') e^{-ik\hat{\boldsymbol{r}}\cdot\boldsymbol{r}'} - \hat{\boldsymbol{r}}\hat{\boldsymbol{r}} \boldsymbol{J}(\boldsymbol{r}') e^{-ik\hat{\boldsymbol{r}}\cdot\boldsymbol{r}'} \right] \right\}, \tag{2.39}$$

where the radial term is canceled, as expected. This expression is used in a normalized form by omitting the terms related to $\boldsymbol{r}$.

2.2.2 Method of Moments

For the full-wave solutions of electromagnetic problems considered in this thesis, MOM is used to solve integral equations in the phasor domain. A given geometry is discretized into smaller regions (elements), and a matrix equation is constructed, where the matrix elements represent the interactions of these elements and the RHS vector represents the excitation applied to the geometry (incident fields). The solution of the matrix equation gives electric and magnetic current coefficients, which are further used to analyze scattering, reflection, or other electromagnetic phenomena.

A general form of integral equations can be written as

$$\mathcal{L}\{\boldsymbol{f}\}(\boldsymbol{r}) = \boldsymbol{g}(\boldsymbol{r}), \tag{2.40}$$

25

where $\mathcal{L}$ is a linear operator, $\boldsymbol{f}$ is an unknown vector function, and $\boldsymbol{g}$ is a known vector function. In electromagnetic problems, $\boldsymbol{f}$ represents the unknown electric and magnetic current distributions, while $\boldsymbol{g}$ corresponds to the excitation field. For numerical solutions via MoM, unknown function $\boldsymbol{f}$ can be written in terms of basis functions $\boldsymbol{f}_n$ as

$$\boldsymbol{f}(\boldsymbol{r}) = \sum_{n=1}^{N} \boldsymbol{a}[n] \boldsymbol{f}_n(\boldsymbol{r}), \tag{2.41}$$

where $\boldsymbol{a}[n]$ is the nth unknown weighting coefficient. Substituting equation 2.41 into equation 2.40, we obtain

$$\sum_{n=1}^{N} \boldsymbol{a}[n] \mathcal{L}\{\boldsymbol{f}_n\}(\boldsymbol{r}) = \boldsymbol{g}(\boldsymbol{r}). \tag{2.42}$$

This equation can be tested by testing functions $\boldsymbol{t}_m(\boldsymbol{r})$ as

$$\int d\boldsymbol{r} \boldsymbol{t}_m(\boldsymbol{r}) \cdot \sum_{n=1}^{N} \boldsymbol{a}[n] \mathcal{L}\{\boldsymbol{f}_n\}(\boldsymbol{r}) = \int d\boldsymbol{r} \boldsymbol{t}_m(\boldsymbol{r}) \cdot \boldsymbol{g}(\boldsymbol{r}), \tag{2.43}$$

which can be rearranged by changing the order of summation and integration as

$$\sum_{n=1}^{N} \boldsymbol{a}[n] \int d\boldsymbol{r} \boldsymbol{t}_m(\boldsymbol{r}) \cdot \mathcal{L}\{\boldsymbol{f}_n\}(\boldsymbol{r}) = \int d\boldsymbol{r} \boldsymbol{t}_m(\boldsymbol{r}) \cdot \boldsymbol{g}(\boldsymbol{r}). \tag{2.44}$$

Finally, in a closed form, equation 2.41 can be written as a matrix system as

$$\sum_{n=1}^{N} \boldsymbol{a}[n] \bar{\boldsymbol{Z}}[m, n] = \boldsymbol{\omega}[m], \tag{2.45}$$

where

$$\bar{\boldsymbol{Z}}[m, n] = \int d\boldsymbol{r} \boldsymbol{t}_m(\boldsymbol{r}) \cdot \mathcal{L}\{\boldsymbol{f}_n\}(\boldsymbol{r}) \tag{2.46}$$

$$\boldsymbol{\omega}[m] = \int d\boldsymbol{r} \boldsymbol{t}_m(\boldsymbol{r}) \cdot \boldsymbol{g}(\boldsymbol{r}). \tag{2.47}$$

Here, $\bar{\boldsymbol{Z}}[m, n]$ represents interactions between discretization elements (impedance matrix) and $\boldsymbol{\omega}[m]$ represents the projection (testing) of the known incident fields. In an iterative solution, the constructed matrix equation is satisfied approximately within a given residual error. The corresponding residual vector can be written as

$$\boldsymbol{R}[m] = \boldsymbol{\omega}[m] - \sum_{n=1}^{N} \boldsymbol{a}[n] \bar{\boldsymbol{Z}}[m, n]. \tag{2.48}$$

Iterative methods such as the generalized minimal residual method (GMRES) or the conjugate gradient method (CG) can be used to approximate the values of $\boldsymbol{a}[n]$. In this study, GMRES is preferred as the iterative method due to its superior performance for EFIE-based matrix equations.

2.2.2.1 Preconditioner

Preconditioners are applied to improve the conditioning of matrix equations; in other words, they are used to construct more suitable linear system that is easier to solve iteratively with faster convergence rates. Considering $\bar{\boldsymbol{M}}$ as a preconditioner and $\bar{\boldsymbol{A}}\boldsymbol{x} = \boldsymbol{b}$ as the linear system to be solved, preconditioning (specifically, left preconditioning) can be shown as

$$\bar{\boldsymbol{A}}\bar{\boldsymbol{M}}^{-1}\bar{\boldsymbol{M}}\boldsymbol{x} = \boldsymbol{b} \tag{2.49}$$

$$\bar{\boldsymbol{A}}\bar{\boldsymbol{M}}^{-1}\boldsymbol{y} = \boldsymbol{b} \tag{2.50}$$

$$\bar{\boldsymbol{M}}\boldsymbol{x} = \boldsymbol{y}. \tag{2.51}$$

Hence, by applying a preconditioner $\bar{\boldsymbol{M}}$, the linear system is solved in two steps; first solving equation 2.50 for $\boldsymbol{y}$ and then solving equation 2.51 for $\boldsymbol{x}$. In both steps, the condition numbers should be smaller than the condition number of the original system for an effective preconditioning.

In this study, incomplete LU factorization (ILU) is preffered for preconditioning. LU factorization creates $\bar{\boldsymbol{L}}$ and $\bar{\boldsymbol{U}}$ matrices such that a matrix $\bar{\boldsymbol{A}}$ is defined in the form of

$$\bar{\boldsymbol{A}} = \bar{\boldsymbol{L}}\bar{\boldsymbol{U}}, \tag{2.52}$$

where $\bar{\boldsymbol{L}}$ is an upper triangular matrix and $\bar{\boldsymbol{U}}$ is a lower triangular matrix. ILU is an approximate version of LU with a predefined approximation rate $\bar{\boldsymbol{R}}$ as

$$\bar{\boldsymbol{A}} \approx \bar{\boldsymbol{L}}\bar{\boldsymbol{U}} \tag{2.53}$$

$$\bar{\boldsymbol{R}} = \bar{\boldsymbol{A}} - \bar{\boldsymbol{L}}\bar{\boldsymbol{U}}. \tag{2.54}$$

The preconditioner is obtained by employing the approximate factors in preconditioner solutions, leading to an effective reduction in the number of iterations at the cost of the factorization time.

2.2.3 Multilevel Fast Multipole Algorithm

MoM can be used directly to perform a full-wave electromagnetic analysis. However, for an electrically large or densely discretized object, its direct application results in unfeasible computational time and memory usage. In MoM, interactions between all unknowns (elements) are calculated and stored, which leads to $\mathcal{O}(N^2)$ complexity, where N represents the number of unknowns. Solution of a constructed matrix equation further has $\mathcal{O}(N^3)$ time complexity if Gaussian elimination is employed, while each matrix-vector multiplication required for an iterative solution has $\mathcal{O}(N^2)$ time complexity.

MLFMA is used to reduce the computational time and memory by applying recursive clustering of unknowns in the linear system. In MoM, interactions between all elements are calculated and present in the interaction matrix. In contrast, in MLFMA, only the interactions between nearby elements are calculated directly, and far-zone interactions are calculated on-the-fly. Deciding which elements are near or far from each other is based on the grouping scheme used in the implementation of MLFMA. As a result, the number of operations, as well as the memory, required to perform a matrix-vector multiplication is reduced from $\mathcal{O}(N^2)$ to $\mathcal{O}(N \log N)$. In addition only $\mathcal{O}(N)$ elements of the matrix are calculated directly and stored in memory so that the overall implementation becomes extremely efficient in comparison to the direct application of MoM.

The difference between MoM and MLFMA is illustrated in Figure 2.6. As shown in this Figure, interactions in MLFMA are computed at multiple levels based on the grouping of discretization elements into clusters (virtual boxes) and building larger clusters by combining smaller ones. Then, radiation patterns of the clusters are obtained from the lowest level to the highest level by performing aggregation operations. Once the radiation patterns are obtained, they are translated between the clusters and converted into incoming fields at the same level. Finally, performing disaggregation operations, the total incoming fields are computed from the highest level to the lowest level, where they are finally received by the discretization elements to finalize the result of the matrix-vector multiplication.
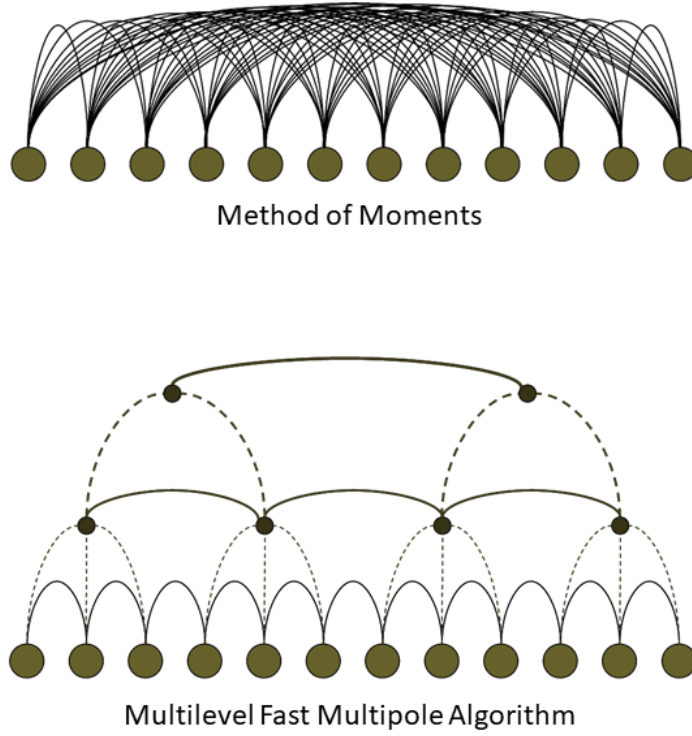
Figure 2.6: Calculation of electromagnetic interactions in MoM (top) and MLFMA (bottom).

2.2.4 Physical Optics

Physical optics (PO) is an approximation that analytically solves scattering problems involving electrically large objects with relatively simple geometries. It is also known as a high-frequency technique, as its approximation is based on optical properties of electromagnetic waves when they encounter electrically large objects. Specifically, if the given geometry is electrically large and does not involve complex electromagnetic interactions between its parts, PO enables a fast electromagnetic analysis by approximating the current coefficients on the surface as

$$\boldsymbol{J}(r) = \begin{cases} 2\hat{\boldsymbol{n}} \times \boldsymbol{H}^i(r), & \text{lit,} \\ 0, & \text{shadow,} \end{cases} \tag{2.55}$$

where $\boldsymbol{J}$ is the induced current on the surface, $\hat{\boldsymbol{n}}$ is normal of the surface, and $\boldsymbol{H}^i$ is

the incident magnetic field intensity. In PO, only surfaces that are in the line of sight of the incident field are lit and have nonzero induced currents, while other surfaces are shadowed without any current induced on them. Using $\boldsymbol{J}$, scattered fields can be found as usual via radiation integrals.

In this study, the optimized surfaces have smooth variations thanks to the previously discussed surface shaping method, and PO can alternatively be used to obtain approximate reflection characteristics of the shaped surfaces. For example, Figure 2.7 presents comparisons of electric field intensity values obtained for five different surfaces that are generated with the same surface generation rules. All surfaces reside on the x-y plane, have $10\lambda \times 10\lambda$ dimensions, and are illuminated by a normally incident plane wave. Figure 2.7 presents scattered fields in the reflection region obtained by using MLFMA and PO, as well as the difference between them. The fields are sampled in on the spherical plane where θ is from 0 to 90 degrees and ϕ is from -45 to 45 degrees. For the given region of interest, the average deviation of PO from MLFMA is below -10 dBV, which can be considered reasonable for many applications. However, such errors do not have controllable characteristics and they are likely to accumulate when favorable individuals are passed from generation to generation in GAs, leading to poor optimization results. Also considering the acceleration provided by MLFMA and reasonable processing times provided by this implementation, all optimization results presented in thesis are obtained by using MLFMA for simulations.

In this chapter, the optimization mechanism constructed to efficiently and accurately shape reflecting surfaces is presented. General operational principles and key parameters, together with novel approaches, are presented in detail for the mechanism that includes a well-designed combination of GAs and MLFMA. As a summary, a scheme of the optimization environment is shown in Figure 2.8. In the next chapter, we present the optimization of reflective surfaces for 5G mm-wave applications and their performance analyses.
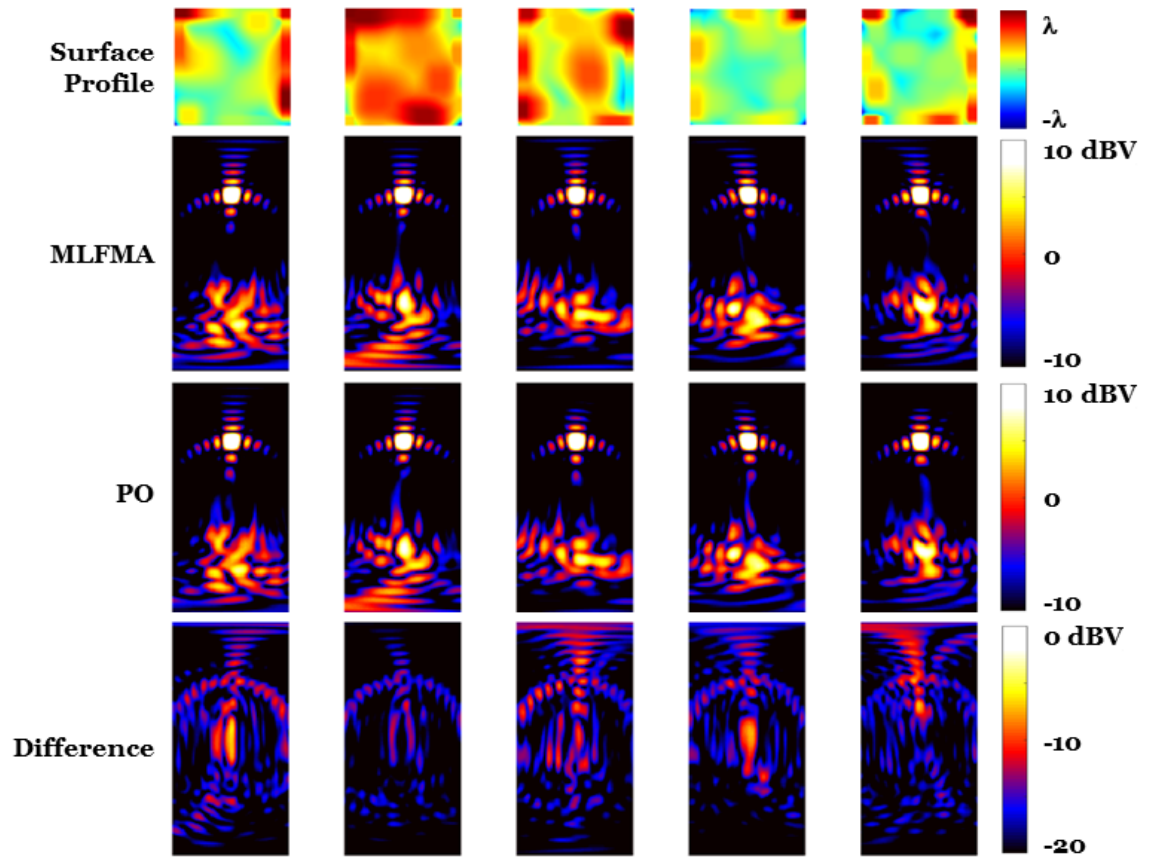
Figure 2.7: Comparison of MLFMA and PO for the analyses of various reflectors with deformed surfaces.
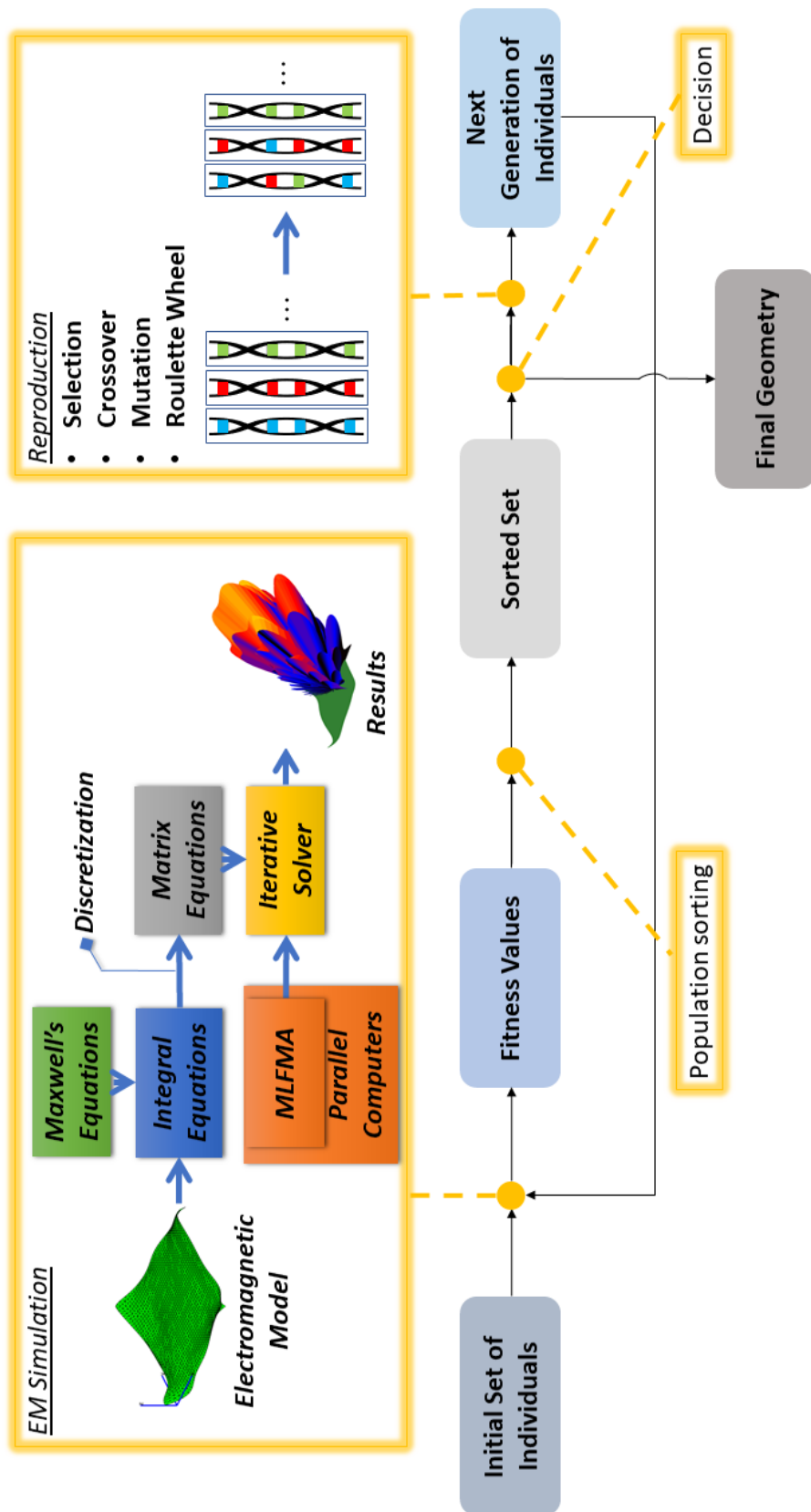
Figure 2.8: Detailed operational diagram of the optimization environment including GAs and MLFMA for full-wave analyses.

CHAPTER 3

OPTIMIZATION OF REFLECTING SURFACES FOR 5G MM-WAVE APPLICATIONS

In this chapter, simulation results for various surface optimizations are presented. We show that, thanks to the well-designed optimization mechanism, optimized surfaces can change field coverage by redirecting incident beams into desired directions with controllable power distributions.

All simulations are conducted in the MATLAB environment. Both MLFMA and GAs are developed and implemented by employing various components and capabilities provided by CEMMETU research group. All simulation and optimization processes are performed on the CEMMETU servers using parallel cores.

For each optimization, fitness value, cumulative distribution function (CDF), and electric field distributions in the far-zone, together with the physical appearance of the optimized surface, are shown. Also, as a sample case, one of the optimization result is analyzed in greater detail, i.e., in terms of operational characteristics in a frequency band, under oblique excitations, and when the surface involves geometric noises that represent possible fabrication errors. All optimized surfaces are compared with the flat surface, which is the most basic and original reflector.

3.1 Initial Surface

In all optimization trials, the initial (original) surface is fixed; it is a 10λ by 10λ flat surface centered at the origin on the x-y plane. It is discretized with $\lambda/10$ edge-sized elements, resulting in 20000 triangles and 10201 nodes representing the surface. This mesh size is chosen to accurately sample induced currents that are used to generate

reflection characteristics. The selected initial surface has viable physical dimensions for coverage enhancements in 5G mm-wave [11] applications, while it corresponds to a compact reflector at 5G frequencies. The triangulated surface of the initial geometry is shown in Figure 3.1.

3.2 Excitation

In all optimization trials, plane-wave excitation is used. A plane-wave is a theoretical wave, which can be represented in the phasor domain as;

$$\boldsymbol{E}(\boldsymbol{r}) = \hat{\boldsymbol{e}} E_0 \exp(i\boldsymbol{k} \cdot \boldsymbol{r}), \tag{3.1}$$

where i is the imaginary unit, $E_0 (V/m)$ is the amplitude, and, $\boldsymbol{k}$ and $\boldsymbol{r}$ are the wave and position vectors, respectively. Plane waves are in fact reasonable representations of waves far away from sources (e.g., far-field regions of antennas); thus they are commonly used in the literature, as well as in this study. Figure 3.2 shows a comparison of radiations from a square reflecting surface excited by a plane wave and a horn antenna. On the left-hand side, the reflector is illuminated by a plane-wave with an oblique incidence, and the computed secondary fields correspond to the reflected fields are shown. On the right-hand side, when the same reflector is excited by a properly tilted horn antenna, we obtain the secondary fields as a combination of reflected fields and those radiated by the antenna. We observe that the reflections have similar characteristics for the plane-wave and antenna excitations, showing that using a plane-wave is a viable approach, without considering the antenna as a part of the problem (and its solution). This is particularly useful for extremely many simulations in reflector optimization.
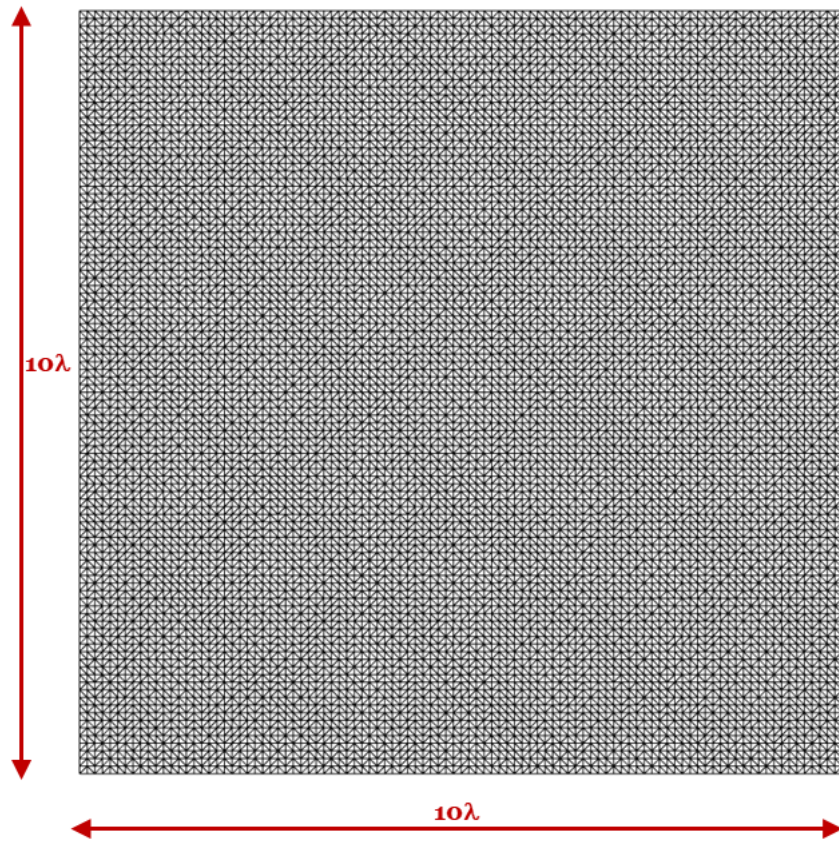
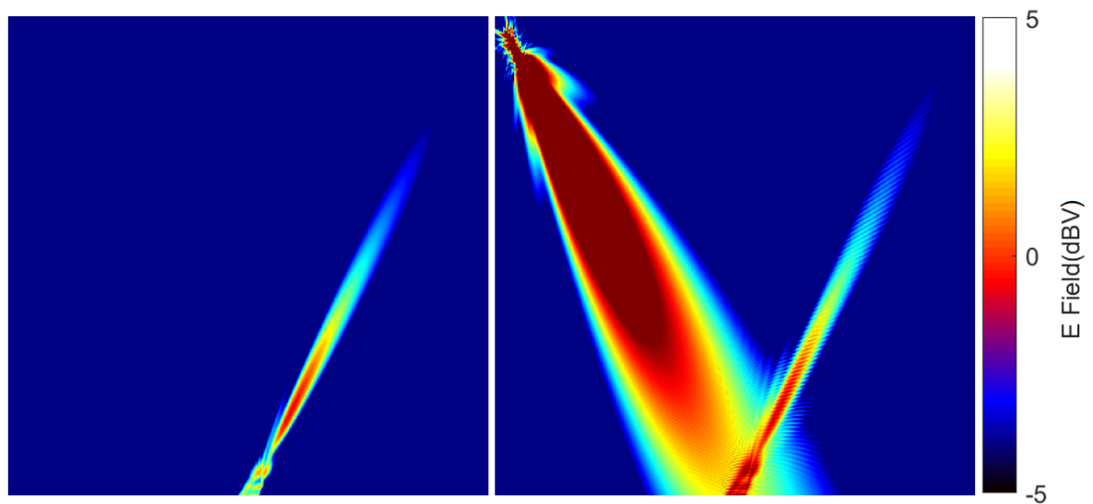Figure 3.1: 10λ by 10λ square surface with $\lambda/10$ mesh.

Figure 3.2: Secondary fields obtained when a reflector (at the bottom center) is excited by a plane wave (left) and a horn antenna (right).

3.3 Optimization Parameters

An electromagnetic analysis of a single surface requires approximately 600 seconds. Consequently, for a single design (optimization), the processing time is between 30 and 40 hours. Table 3.1 and Table 3.2 show some of the GA and electromagnetic solver parameters, respectively.

In the following sections, results of an optimization is analyzed in detail, followed by discussions on the effects of optimization parameters. Finally, various optimization results with different cost functions are presented.

3.4 Redirecting Incident Fields in a Single Cut

In the type of the optimization that we focus in this section, a reflecting surface is optimized to obtain constant field distribution over a selected set of directions in the y-z plane in the far zone. Such a surface can be used in applications when mobile signals need to pass through a narrow slit or a steady level of signal is required in a limited region. The surface is constrained to be symmetric with respect to the y-z ($x = 0$) plane. The optimization setup can be seen in Figure 3.3. Incident waves are directed from $\theta = 45$, $\phi = -270$ degrees in spherical coordinates, the electric field polarized in the x direction. The filled dots represent the selected far-zone locations (far-field points) where the reflected fields are optimized, and they are located from $\theta = 30$ to $\theta = 60$ degrees in the y-z plane. Using a sampling rate of 1.5 degrees, the number of selected far-zone locations is 20.

Table 3.1: GA parameters

Number of Generations	200
Number of Individuals	20
Multigrid Level	40
Moderate Mutation	70% (99% for adaptive reproduction)
Heavy Mutation	10% (50% for adaptive reproduction)
Crossover	42.5% (49.5% for adaptive reproduction)

Table 3.2: Electromagnetic solver parameters

Electromagnetic Solver	MLFMA
Solution Environment	MATLAB
Error Limit of the EM Solver	$0.01 - 0.001$
Preconditioner	ILU
Surface Size	10λ by 10λ
Mesh Size	0.1λ
Solution Time	1 day for 8000 simulations (per optimization)

3.4.1 Fitness Function Definition

In this optimization problem the goal is to obtain a constant field value of 12 dBV over the predefined far-field points. This value is chosen first by observing the reflection characteristics of the flat (unoptimized) surface at the same far-field points and evaluating achievable values by deformations.

3.4.2 Surface Representation

Initially, surfaces are controlled by 16 points on the surface (using a 4 by 4 grid), and each of these points is moved within the $\pm 2\lambda$ range in the z direction with three-digit precision. Throughout the optimization, at every 40 generations, two control points are added on each axis. For example, between 41st and 80th generations, the optimization uses 36 points (6 by 6 grid), while it uses 64 points (8 by 8 grid) between 81st and 120th generations. This trend continues until the decision criteria are met. We recall that this systematic increase in the number of control points is called multigrid optimization, which provides more efficient results in comparison to optimization with fixed control points.
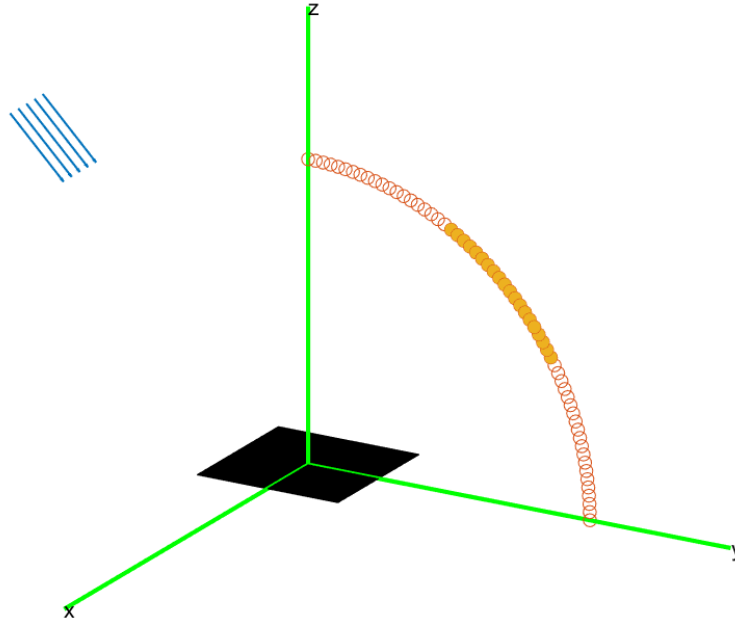
Figure 3.3: Optimization setup for redirecting incident fields towards a set a directions in a single cut.

3.4.3 Optimization History

The optimization history (the fitness value throughout generations) is shown in Figure 3.4. These values correspond to the fitness values of the best individuals (reflecting surfaces) of generations. The initial surfaces have relatively poor reflection characteristics at the beginning of the optimization, but the GA implementation quickly improves the designs in the early generations, followed by gradual improvements mainly via fine tuning on surface shapes in the rest of the optimization. This type of a fitness value variation throughout an optimization, i.e., a rapid convergence followed by gradual improvements, is a typical behavior of GAs, while it is more common for a multigrid optimization. Considering the optimization in Figure 3.4 quantitatively, the fitness value is increased from -95.68 dBV to -33.59 dBV, which represents more than 60 dB improvement.
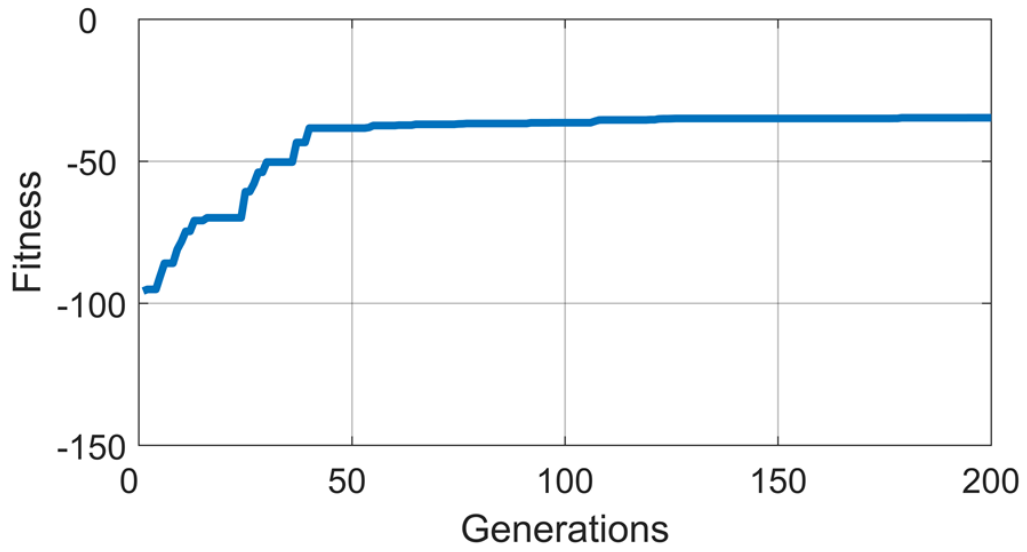
Figure 3.4: Optimization history (fitness value throughout generations) for the optimization problem in Figure 3.3.
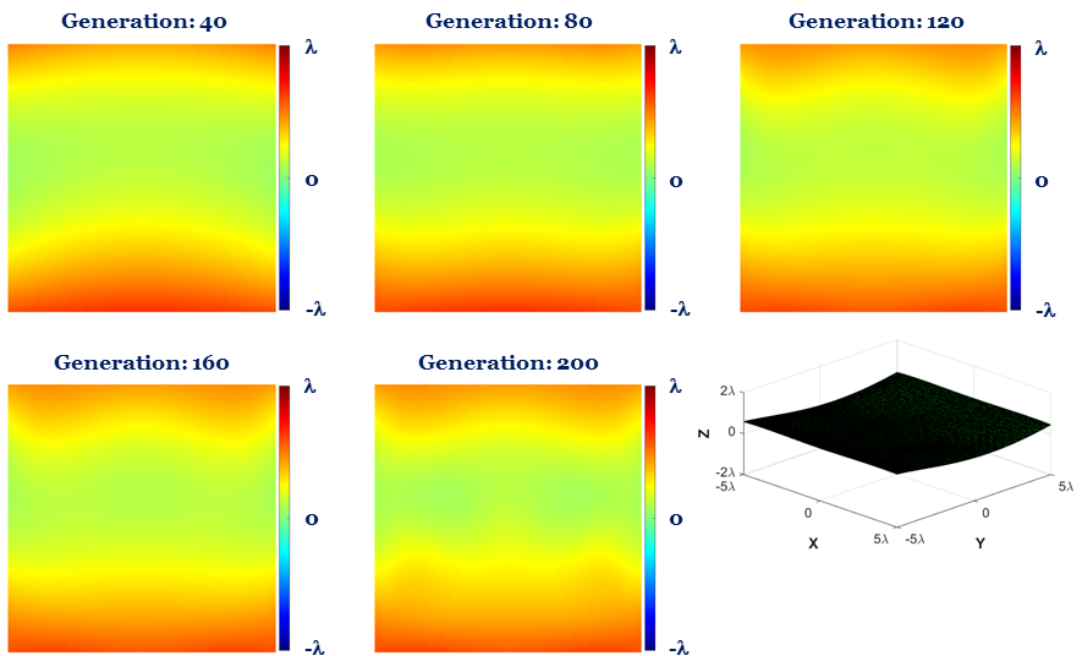
Figure 3.5: Topographical view of the optimized surface at the end of every 40 generations and a 3D view of the final optimized surface.

3.4.4 Optimized Surface

The topographical visualization of the optimized surface at the end of every 40 generations, together with the 3D view of the final optimized surface, are presented in Figure 3.5. It is also evident in these figures that the GA implementation reaches a coarsely optimal surface in initial generations, and fine tunings are made during the rest of the optimization.
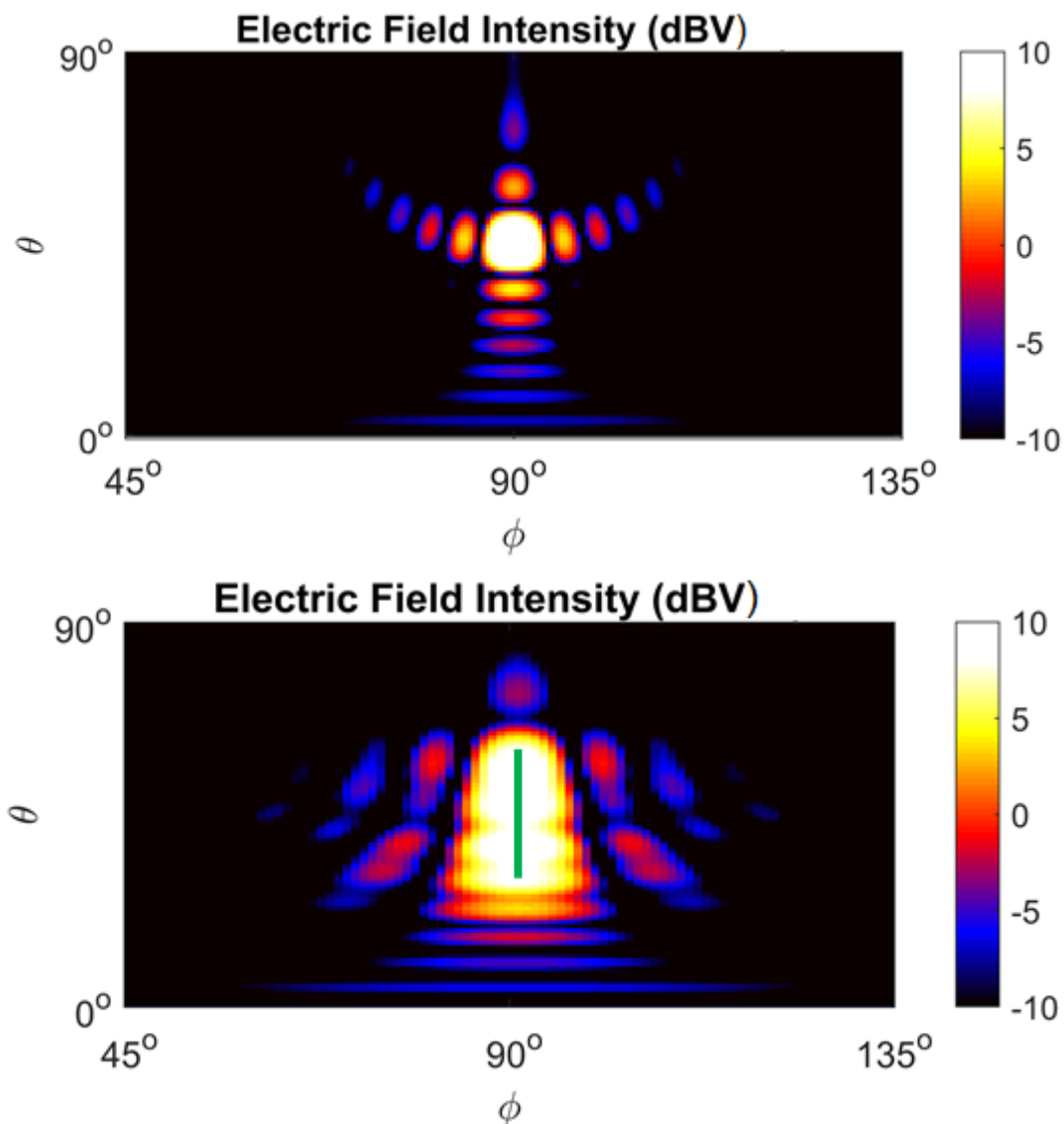
Figure 3.6: The reflected electric field intensity distributions in the far zone obtained for the flat surface (top) and the optimized surface (bottom).

3.4.5 Electric Field Intensity Distribution in the Far Zone
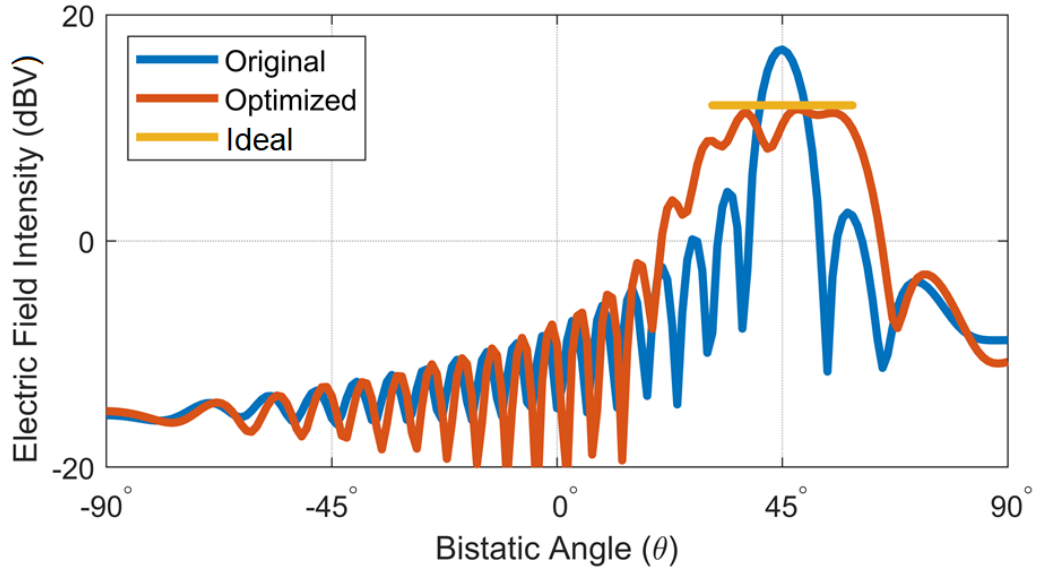
Figure 3.7: The reflected electric field intensity distributions in the optimization (y-z) plane obtained for the flat and optimized surfaces.

The reflected electric field intensity distributions in the far zone for the flat and optimized surfaces are presented in Figure 3.6, where the green line represents the selected optimization points. It is inferred from the figure that the reflected fields from the optimized surface are higher at the optimization points with a more uniform distribution over them, whereas the reflected fields from the flat surface shows a focusing behavior. To further illustrate the effect of the optimization, the electric field intensity values on the optimization (y-z) plane are shown in Figure 3.7. It is observed that the reflected fields become much more steady in the desired range thanks to the optimization.

3.4.6 Cumulative Distribution Function

Observations of fitness values and reflected fields may not be sufficient to understand the success of an optimization. For this purpose, CDF is defined as

$$F_X(x) = P(X <= x), \tag{3.2}$$

41

where F_X is CDF of X with respect to x, namely the probability that X has a value less than or equal to x. In this study, CDF is used as a comparative metric to support observations on reflected fields and fitness values.

The CDF of the optimized surface considered so far, based on the optimization locations, is shown in Figure 3.8. In this figure, the blue line shows the CDF for the flat surface, the red line shows the CDF for the optimized surface, and the green line shows the best achievable CDF using an ideal reflector (whether such a reflector exists or not). In the plots, while CDF values are represented by the y axis, the x axis represents the electric field intensity values. For example, an electric field intensity value with a CDF value of 1 indicates that, this intensity value is the maximum among all intensity values at the optimization points. On the other hand, an electric field intensity value with a CDF value of 0 indicates that, this intensity value is the minimum among all intensity values at the optimization points. Obviously, when the electric field intensity is exactly the same at all optimization points, the CDF curve should be a vertical line. For this optimization, this vertical line is located at 12 dBV, i.e., the target electric field intensity. In Figure 3.8, it is observed that the optimization successfully improves the CDF from blue line to red line, indicating that the variation in the electric field intensity is reduced (the curve becomes more straight) and the CDF becomes closed to the best case (the values become close to the target 12 dBV). Numerically, the median gain, where CDF is 0.5, is increased from 4.1 dBV to 10.9 dBV, corresponding to 6.8 dBV improvement, by the optimization.

3.4.7 Band of Operation Frequency

The optimized surface is further examined in terms of its performance with respect to frequency. The CDF of optimized surface is calculated and compared to the CDF of the flat surface in a range of frequencies from 10 GHz to 59 GHz, as presented in Figure 3.9. Although the optimization is performed at 30 GHz, it is observed that it has a higher median gain than the flat surface from 20 GHz to 59 GHz. Such a wide band of operation frequency is achieved thanks to the followed optimization strategy that leads smooth variations on the surface. We note that a wideband operation is needed especially for devices used in 5G mm-wave applications and the reflectors designed in this study satisfy this requirement.
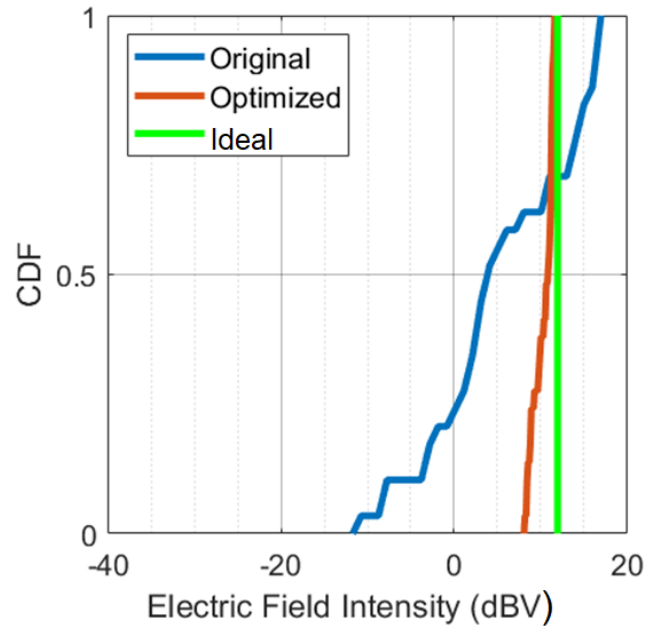
Figure 3.8: CDF of the optimized and original surfaces in comparison to the CDF of the best (ideal) case.
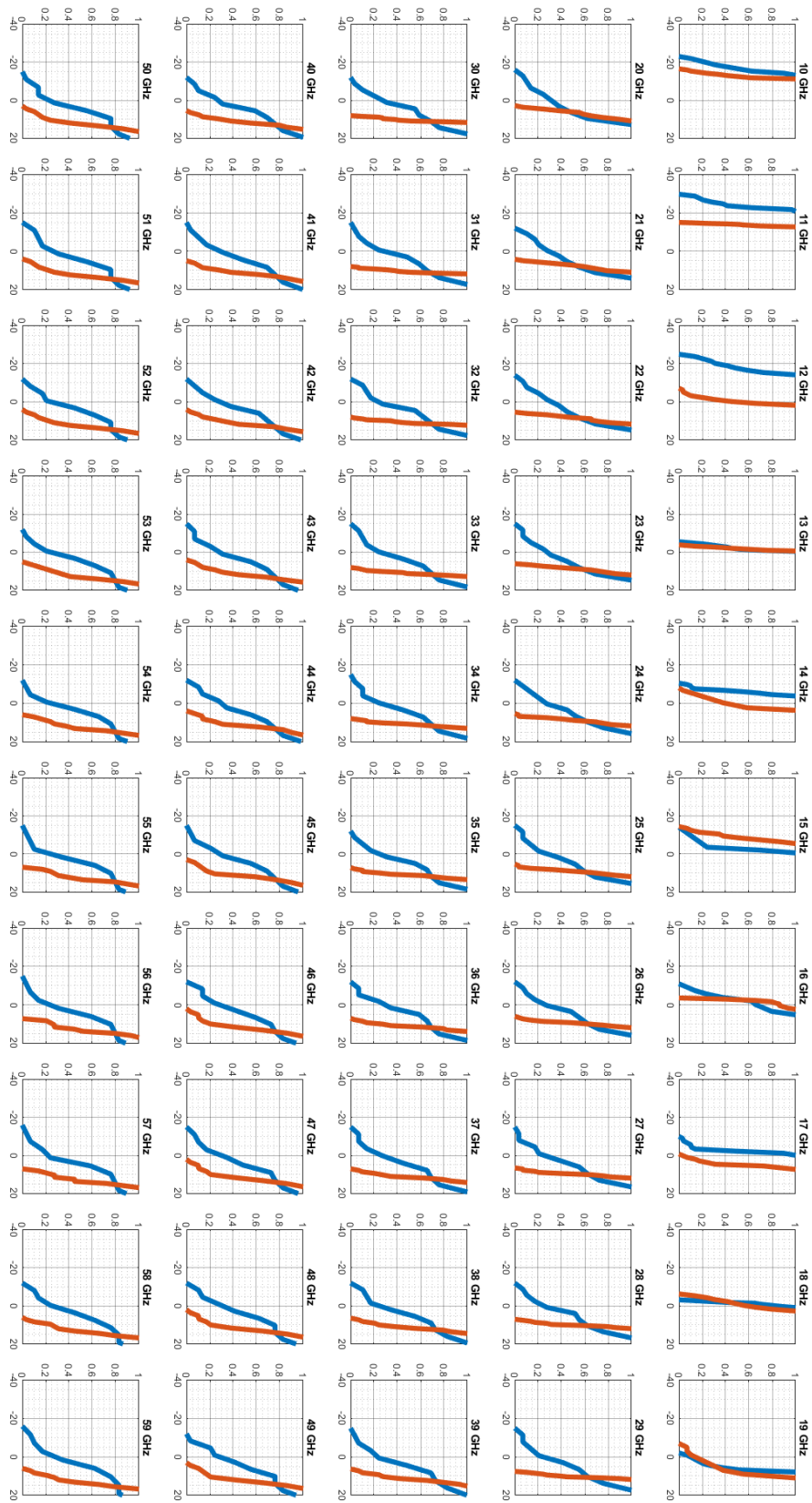
Figure 3.9: CDF of the optimized and flat surfaces from 10 GHz to 59 GHz.

44

3.4.8 Sensitivity Analyses

The optimized surface is investigated in terms of different sensitivity metrics, namely polarization changes, incident wave directions, and surface defects.

3.4.8.1 Effects of Polarization

The optimization is performed for a linearly polarized plane wave with the electric field in the x direction. In mobile communications, incoming waves typically have variations in polarization due to various disturbances in the communication medium and positioning of devices. Figure 3.10 shows that changing the polarization of the incident wave from the intended one to the perpendicular case (magnetic field in the x direction) has insignificant effects on the CDF, demonstrating that the optimized surface is capable of maintain its performance under different polarizations.

3.4.8.2 Effects of Incident Wave Direction

In mobile communication applications, radiation directions of sources are usually disturbed and not exactly as they are designed; so it is important to observe the effects of the direction of the incident wave on the reflection performance of an optimized surface.

For the optimized surface, CDF values obtained for different θ angles are depicted in Figure 3.11. Here, the angle of 45 degrees corresponds to the original incidence so that we consider tilts in the range of ± 5 degrees around the original direction. We observe that even 5 degrees of tilts in both directions slightly deteriorate the reflection performance. Similar tests are also performed for deviations in the ϕ direction, and the results for the CDF values are shown in Figure 3.12. In this case, the angle of 90 degrees corresponds to the original incidence, while it is deviated up to -5 degrees. Unlike the tilts in the θ direction, the CDF of the reflector is severely affected by changes in ϕ angles. This is directly related to the broken symmetry of the reflector for the tilts in the ϕ direction, particularly considering that the optimization is based on locations selected on the y-z cut. For applications that possess uncertainties in the plane of incidence, other reflectors can be designed accordingly. In general, the

results in Figure 3.11 and Figure 3.12 demonstrate that the designed reflectors may demonstrate different sensitivities to different parameters, depending on how they are designed.
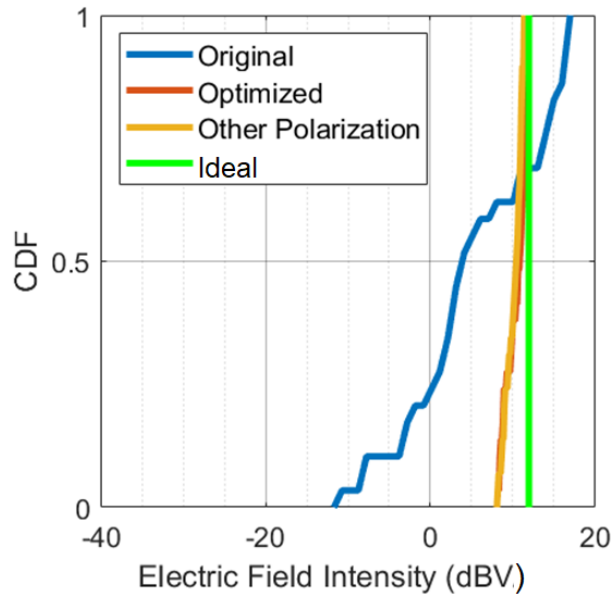

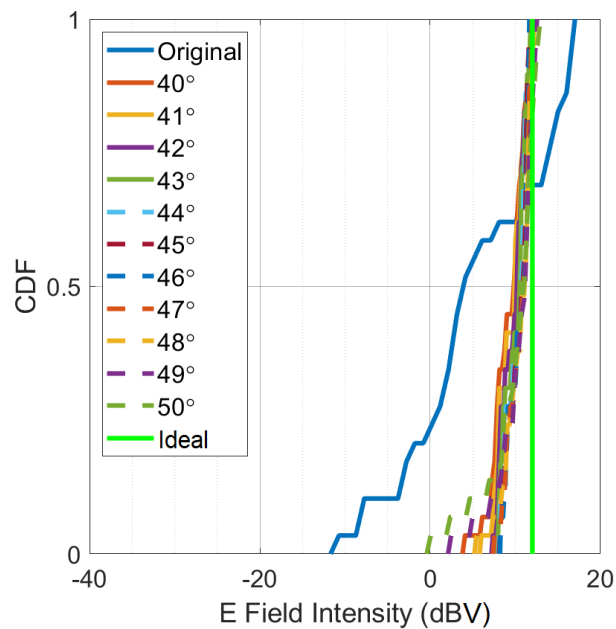Figure 3.10: Sensitivity of the optimized surface to polarization in terms of the CDF.

Figure 3.11: Sensitivity of the optimized surface to the illumination direction, when the variation is in the original plane of incidence.
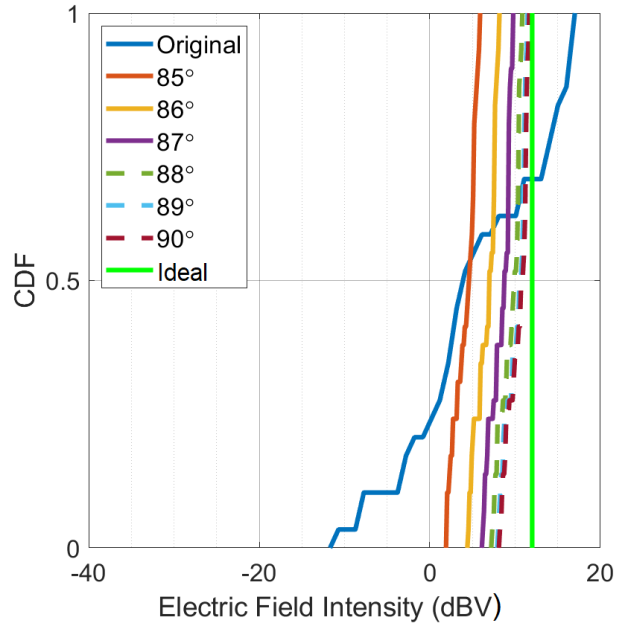
Figure 3.12: Sensitivity of the optimized surface to the illumination direction, when the variation changes the plane of incidence.

3.4.8.3 Effects of Surface Defects

The optimized surface is also investigated in terms of geometric faults that may occur in their fabrications or when they are in use. To observe such effects, first, Gaussian-type noises with various scales are added onto the discretization nodes of the optimized surface, second, onto the control points that are used to shape the surface during optimizations.

In Figure 3.13 and in Figure 3.15, four surfaces are shown together with the noise-free (optimized) surface for the Gaussian-type noises added onto discretization nodes and onto control points, respectively. The smallest introduced noise scale is $\lambda/40$, while the largest one is $\lambda/5$. CDF values for all surfaces are compared in Figure 3.14 and in 3.16 for the surfaces in 3.13, and in 3.15, respectively.

For the noises added onto the discretization nodes, the median gain of the CDF (with respect to the flat surface) is deteriorated only by 0.5 dBV at $\lambda/10$ noise level. At $\lambda/5$ noise level, it is decreased by 2.7 dBV, even though the noise added onto the surface

causes significant geometric deviations, much beyond fabrication errors.

For the noises added onto the control points, deterioration due to added noises are similar to the previous noise study. At $\lambda/10$ noise level, the median value of CDF is decreased by 0.8 dBV, and at $\lambda/5$ noise level, the median value of CDF is decreased by 1 dBV.

Analyses similar to those presented in Figure 3.13 and 3.15 show that optimized surfaces designed in this study demonstrate strong resistance for geometric faults.

With sample sensitivity analyses, we complete this section that exemplifies the study of the thesis via one of the optimized surface. In the next section, more optimized surfaces are presented and compared in terms of optimization stability. The optimized surface presented so far is called OPT1 in the rest of this thesis.

Figure 3.13: Topographical views of surfaces obtained by adding Gaussian noise onto the discretization nodes, together with a 3D view of the original optimized surface.

Figure 3.14: Comparisons of CDF values for the deformed surfaces in Figure 3.13.
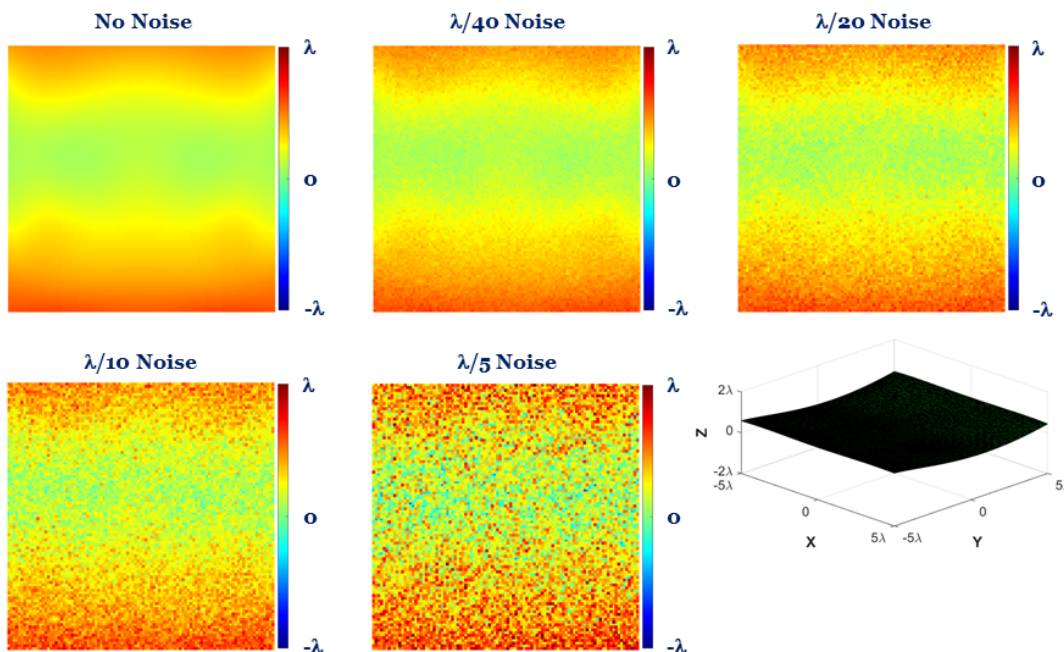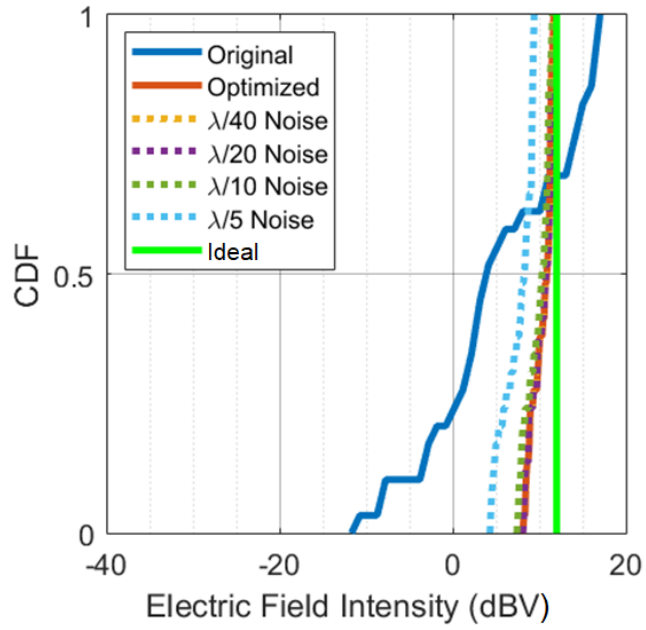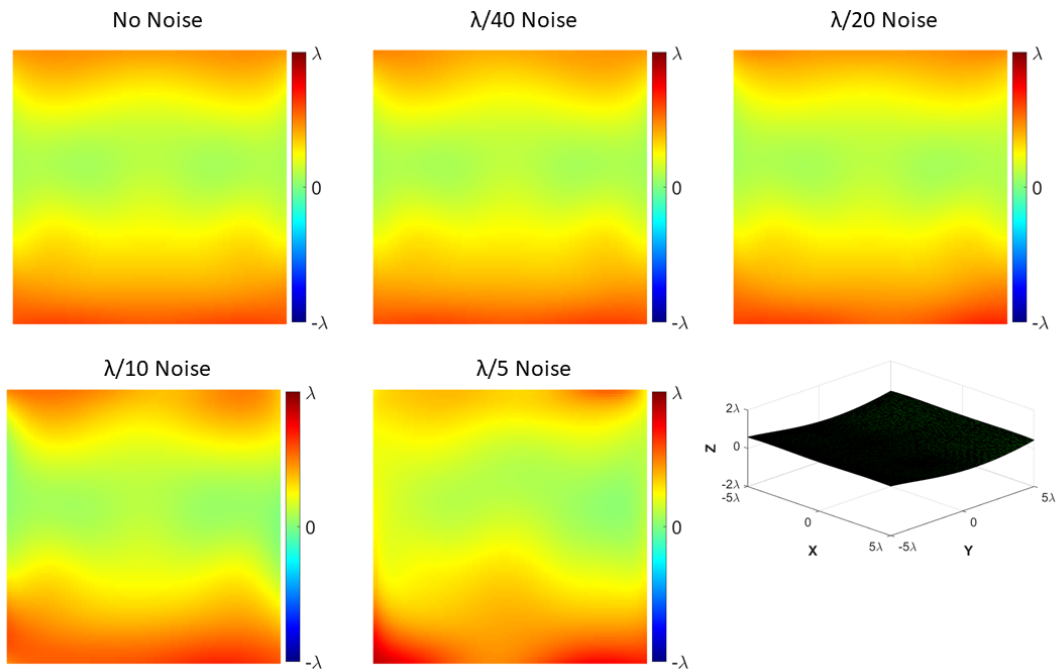

Figure 3.15: Topographical views of surfaces obtained by adding Gaussian noise onto the control points, together with a 3D view of the original optimized surface.
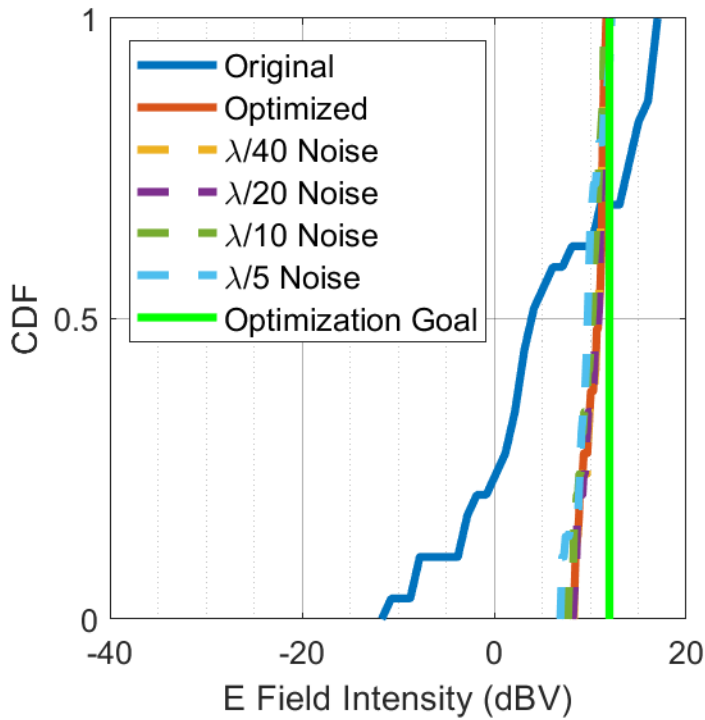
Figure 3.16: Comparisons of CDF values for the deformed surfaces in Figure 3.15.

3.5 Optimization Stability Analysis

In GAs, obtaining similar results for the same optimization problem in different trials is essential to prove whether the optimization process is stable or not. Due to its random nature, the optimization path can be different in each run, but the the quality of the final result is desired to be consistent. Figure 3.17 shows optimization histories for four different optimization runs for an identical purpose (using design criteria for OPT1). It is observed that, regardless of the random nature of the optimization process, the final designs have fitness values between $-33\,\mathrm{dBV}$ and $-36\,\mathrm{dBV}$. Specifically, there is only a 3 dBV discrepancy between the fitness values, confirming the stability of the GA implementation.

Figure 3.18 shows that, despite they reach similar fitness values, the optimized surfaces are different from each other due to random initialization and alternative optimization paths. On the other hand, when we investigate the electric field intensity distributions for these surfaces in Figure 3.19, we observe their similar reflection

characteristics, which are consistent with their fitness values. In addition, Figure 3.20 displays the similarity of the CDF values for the designed reflector. The median gains over the flat surface for these designs (OPT1 to OPT4) are 6.8, 6.4, 6.6, and 6.6 dBV, respectively.
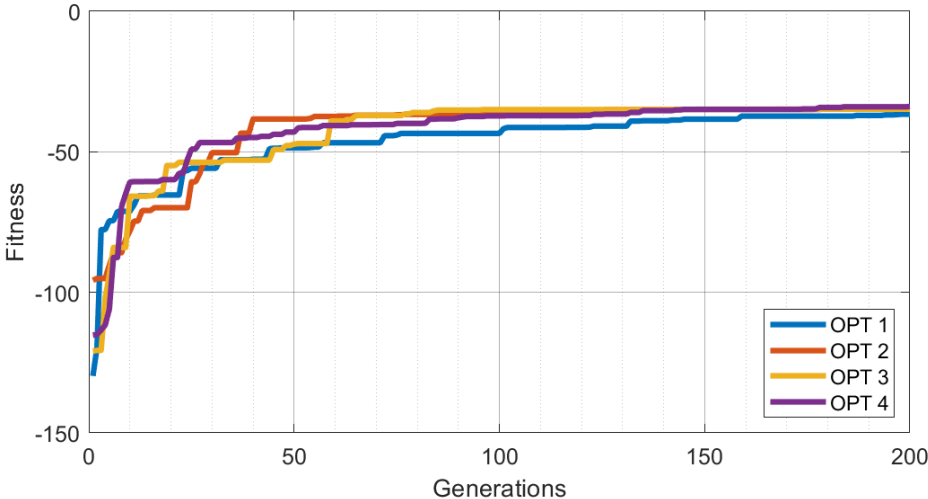
Figure 3.17: Optimization histories for four designs: OPT1, OPT2, OPT3, and OPT4.
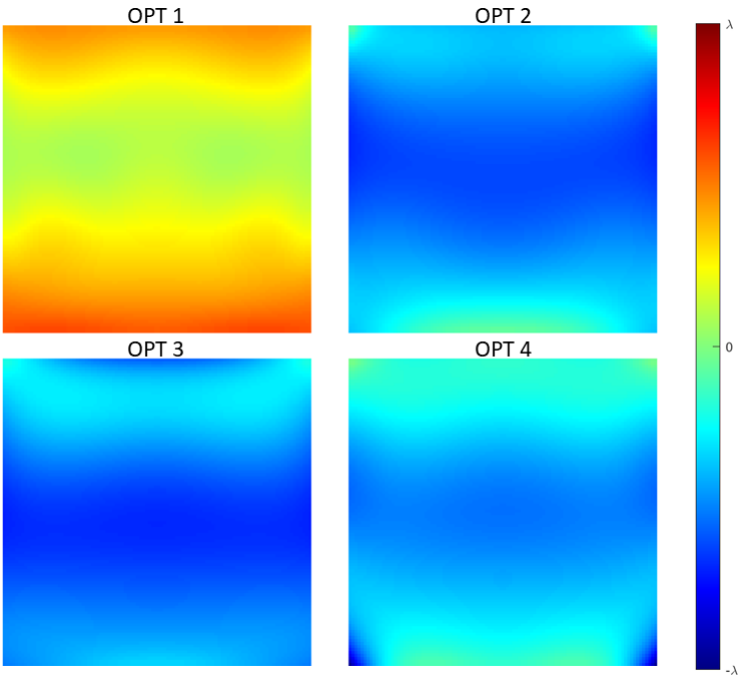
Figure 3.18: Topographical views of the optimized surfaces OPT1, OPT2, OPT3, and OPT4.

51
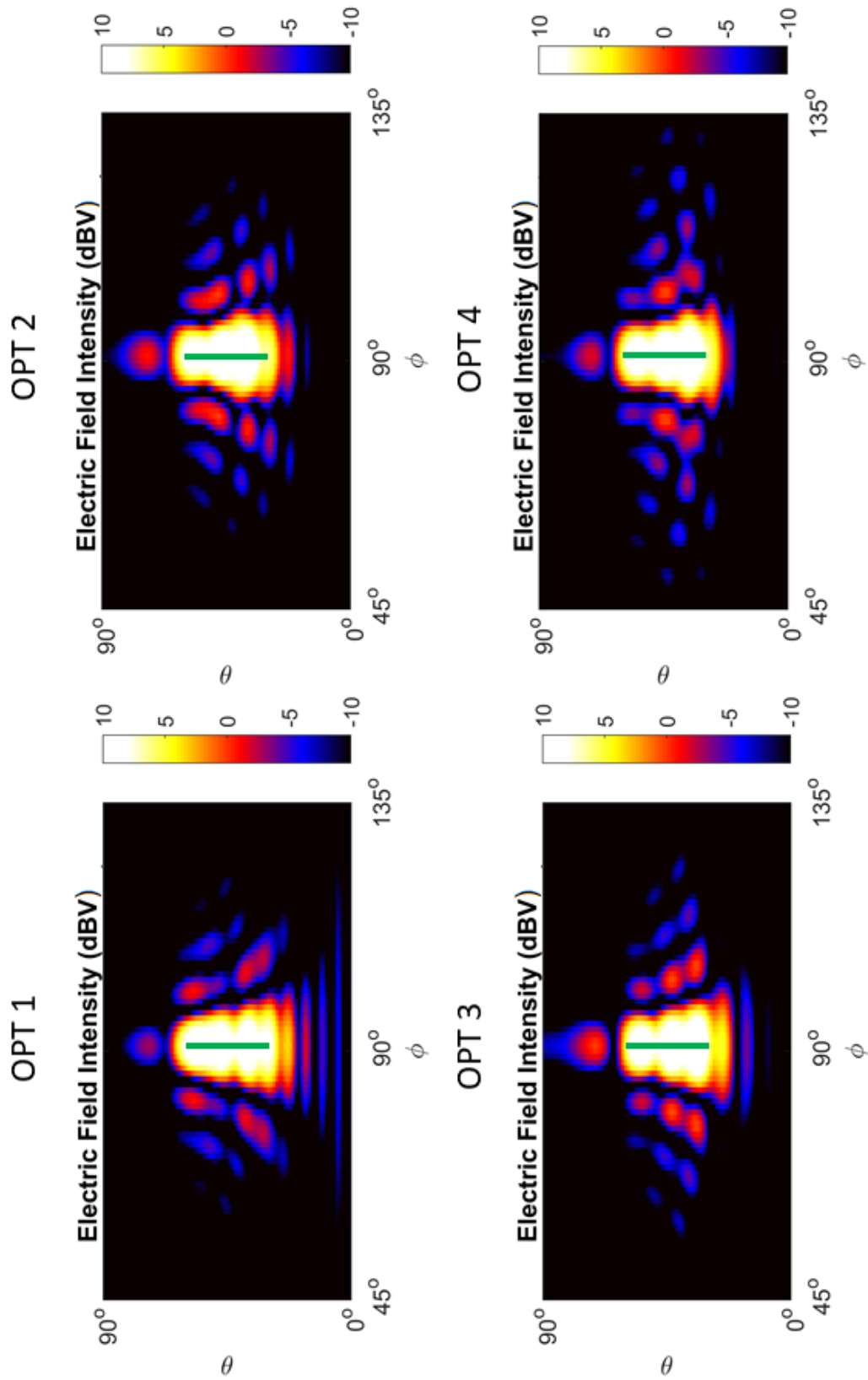
Figure 3.19: Electric field intensity distributions obtained by the reflections from the optimized surfaces OPT1, OPT2, OPT3, and OPT4.
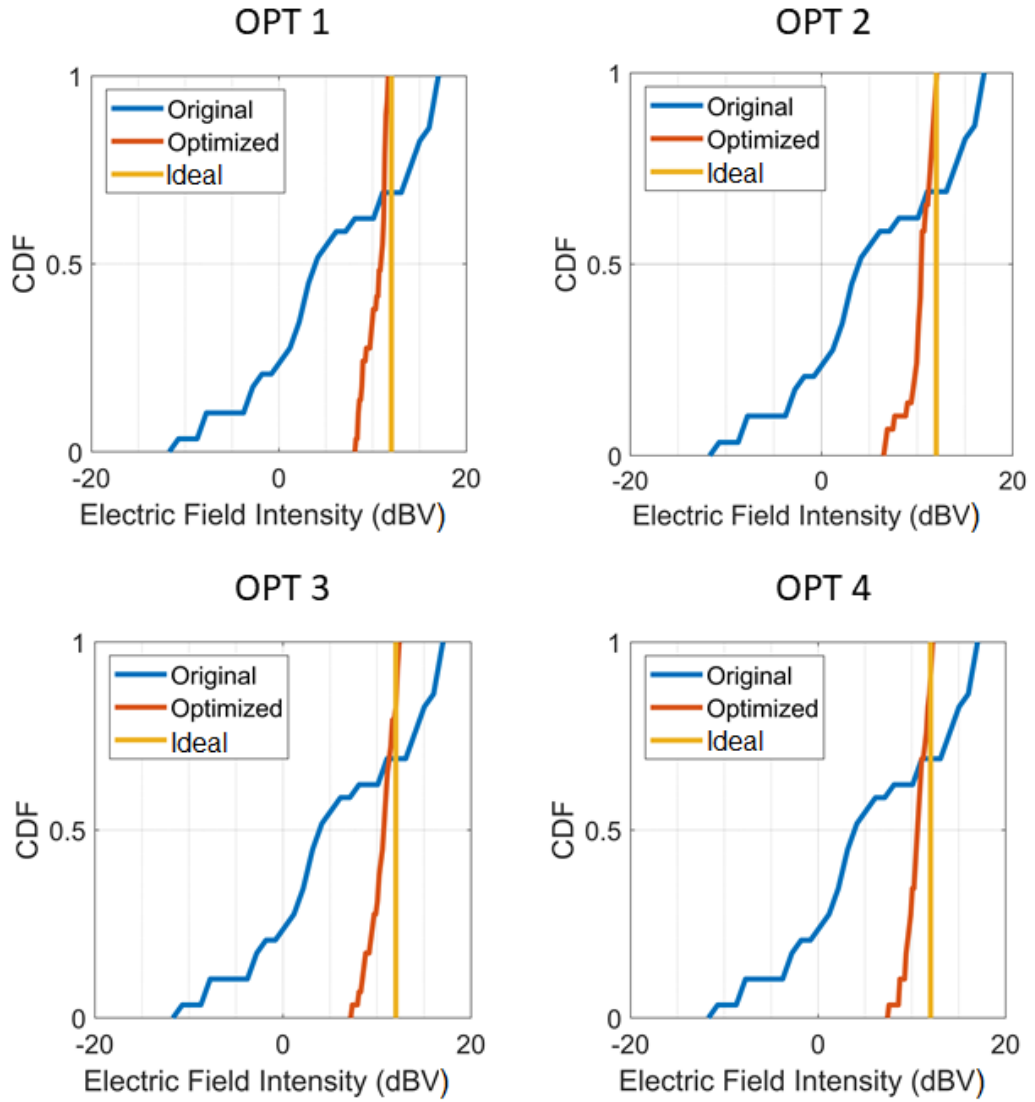
Figure 3.20: CDF values for OPT1, OPT2, OPT3, and OPT4, in comparison to the CDF of the flat surface.

3.6   Fitness Function Analysis

It is also interesting to see the effects of the fitness function definition on the overall optimization results. Even when using the same set of directions, targeting a high electric field intensity may result in poor optimization results; on the other hand, choosing a low value may prevent using the full reflection capability of the optimized surfaces.

In Figure 3.21, electric field intensity distributions of four different optimization trials are presented. In OPT1 and OPT6, the aim is to have constant field values at angles $\theta = 45 \pm 15$ degrees and $\phi = 90$ degrees; specifically 12 dBV for OPT1 and 5 dBV for OPT6. Similarly in OPT5 and OPT7, the aim is to maintain constant field values at $\theta = 45$ degrees and $\phi = 0 \pm 30$ degrees; 12 dBV for OPT5 and 5 dBV for OPT7. In the far-field distributions depicted in Figure 3.21, it is observed that targeting a higher value via the fitness function results in better concentration of power around the selected far-zone locations. Even thought the plots in Figure 3.21 show how the fields are distributed in the far zone, they do not demonstrate how field values vary between the selected optimization points. In Figure 3.22, CDF values are presented for the same optimization results, in comparison to the CDF of the flat surface. In these plots, we observe that targeting a high field value results in higher field values but with a large variance; conversely, targeting a low field value results in lower field values but with very small variance. Numerically, median gains with respect to the flat surface are 6.8, 11.3, 0.9, and 8.9 dBV, for OPT1, OPT5, OPT6, and OPT7, respectively. From these results, it is concluded that choosing the optimization target is important for the quality and characteristics of the results. Both choosing higher and lower values have advantages, and the optimization should be conducted by considering what is preferred between the peak performance and the stability in the region of interest.
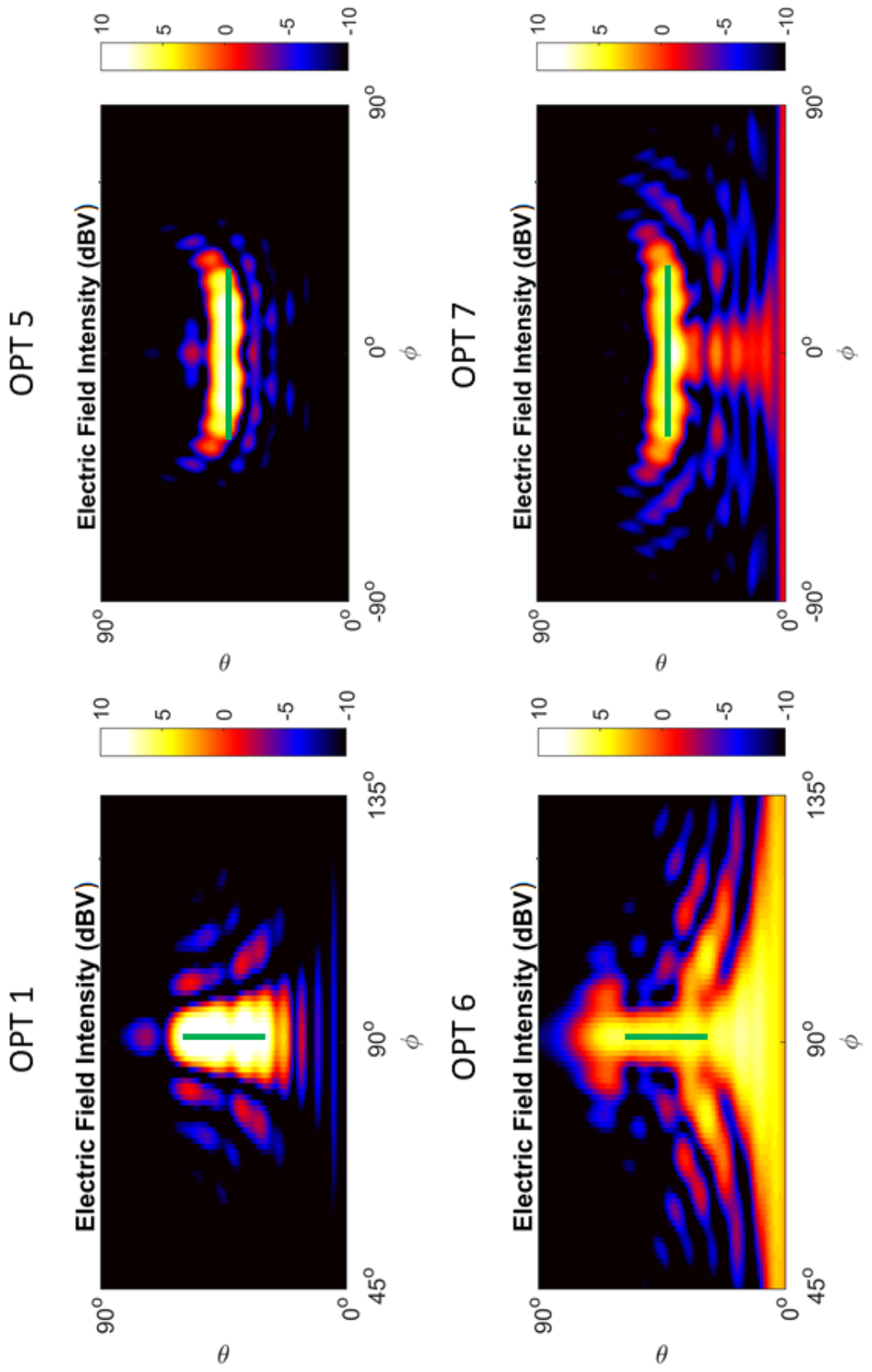
Figure 3.21: Electric field intensity distributions due to optimized surfaces OPT1, OPT5, OPT6, and OPT7.
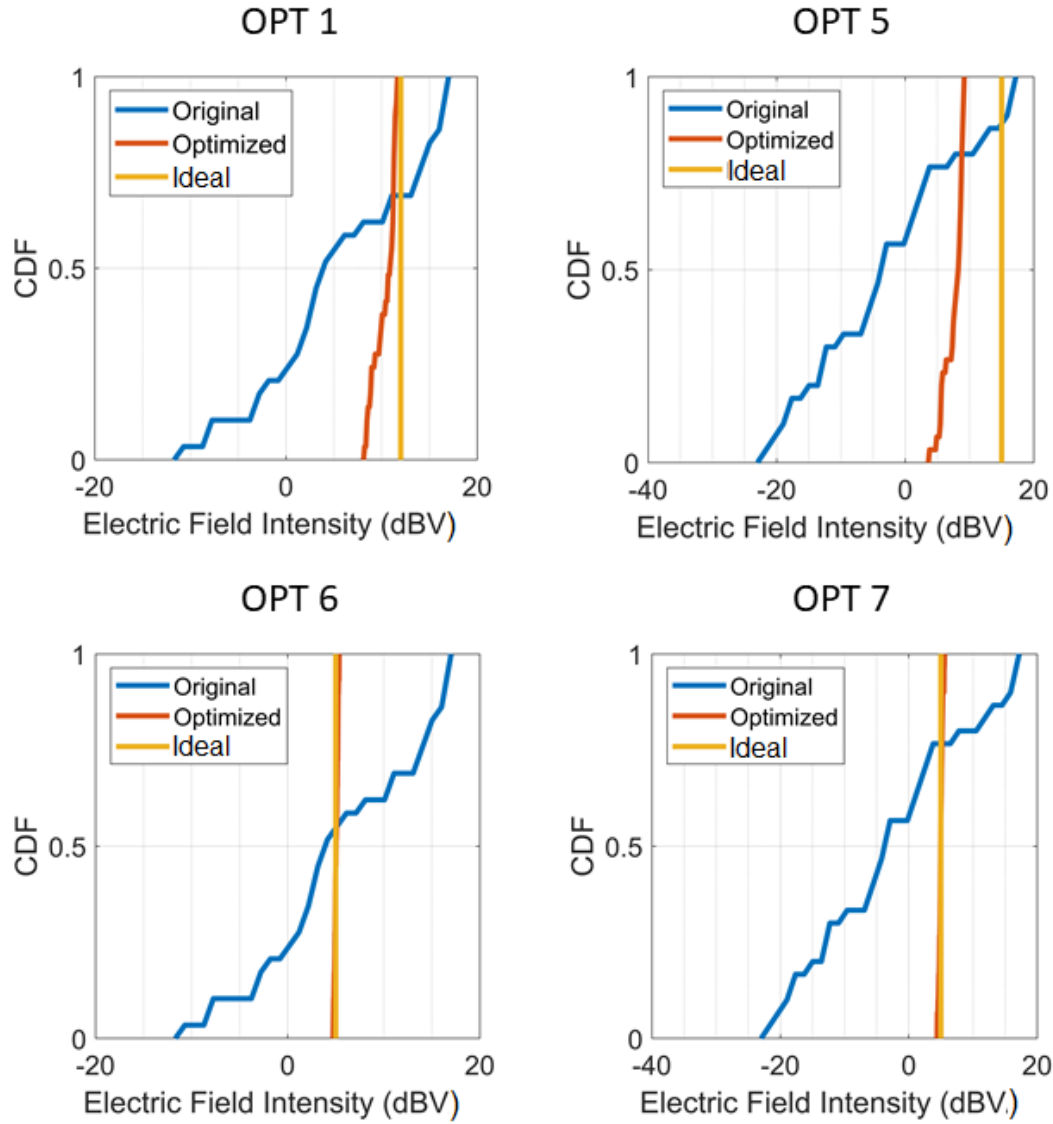
Figure 3.22: CDF values for OPT1, OPT5, OPT6, and OPT7, in comparison to the CDF of the flat surface.

3.7 Examples to Various Optimization Trials

In this part, examples to various optimization trials are presented to exhibit the capabilities of the proposed optimization method, as well as the variety of reflectors that can be designed.

In OPT8, the aim is to achieve a constant field value of 15 dBV at $\theta = 45 \pm 30$ and $\phi = 30 \pm 30$ degrees. The CDF median is increased from -22.9 dBV for the

flat surface to -3.7 dBV for the optimized surface, indicating 19.2 dB improvement. Also, the optimized design has a more uniform field distribution in the selected region of directions. This optimization demonstrates that reflected fields can successfully be reflected towards oblique directions with respect to incident waves.

In OPT9, we aim to maintain a constant field value of 12 dBV at $\theta = 45 \pm 30$ and $\phi = 90$ degrees. In this case, the CDF median is increased from -3.6 dBV for the flat surface to 7.4 dBV for the optimized surface, which corresponds to 10.0 dB improvement. This simulation shows that the optimization directions can be selected in uncommon configurations, such as over a cross shape.

In OPT10, a constant field value of 15 dBV is desired at $\theta = 45 \pm 30$ and $\phi = 30 \pm 15$ degrees. The CDF median is increased from -21.0 dBV for the flat surface to 4.0 dBV for the optimized surface, indicating a significant improvement of 25 dB. In comparison to OPT8, in which a larger sector of directions is considered, this optimization achieves higher field values in the interested region, since the reflected fields are concentrated in a smaller sector.

In OPT11, the aim is to have a constant field value of 5 dBV at $\theta = 30 \pm 15$ and $\phi = 45 \pm 15$ degrees. In this case, we again have a significant improvement in the CFD median, as high as 32 dB, from -30.0 dBV for the flat surface to 2.0 dBV for the optimized surface. This simulation shows that two disconnected sets of directions can be selected as the optimization region.

CDF values for OPT8, OPT9, OPT10, and OPT11 are shown in Figure 3.24, while the electric field intensity distributions in the far zone are depicted in Figure 3.23.

In OPT12, the target is to achieve a constant value of 15 dBV at $\theta = 45 \pm 10$ and $\phi = 30 \pm 10$ degrees. Once again, with a remarkable improvement of 25.2 dB, the CDF median is increased from -19.2 dBV for the flat surface to 6.0 dBV for the optimized surface. The resulting median value of the reflected fields in the selected optimization region is even higher than those obtained via OPT8 and OPT10, as the region of interest is further narrowed in this optimization.

In OPT13, a constant field value of 5 dBV is aimed at $\theta = 45 \pm 30$ and $\phi = 45 \pm 30$ degrees. The CDF median is increased from -24.0 dBV for the flat surface to -5.0

dBV for the optimized surface, demonstrating 19.0 dB improvement. This optimization is another demonstration that an oblique reflection is possible with the optimized designs. Comparing with OPT11, we obtain smaller field values, as the region of interest is enlarged.

A constant field value of 5 dBV is also considered in OPT14, where the directions are selected as $\theta = 60 \pm 15$ and $\phi = 45 \pm 15$ degrees. The CDF median is increased from -24.0 dBV for the flat surface to -2.0 dBV for the optimized surface, i.e., a significant improvement of 22.0 dB is achieved. This optimization is another example that demonstrates the possibility of controlled oblique reflections with the optimized designs.

In OPT15, 5 dBV constant field value is required at $\theta = 45 \pm 30$ and $\phi = 0 \pm 30$ degrees. The CDF median is raised from -16.7 dBV for the flat surface to -1.6 dBV for the optimized surface (15.1 dB improvement), while the field distribution becomes more uniform in the interested region.

In OPT16, the aim is to have constant field value of 15 dBV at $\theta = 45 \pm 30$ and $\phi = 90 \pm 0$ degrees. The CDF median is increased from -2.7 dBV for the flat surface to 7.4 dBV for the optimized surface (10.1 dB improvement). The corresponding CDF plots show that field values inside selected region are more uniform but smaller than those of OPT1 as expected, since the region is enlarged.

Finally, in OPT17, our aim is to maintain a constant field value of 15 dBV at $\theta = 30 \pm 10$ & $\theta = 60 \pm 10$ and $\phi = 45 \pm 10$ & $\phi = 45 \pm 10$ degrees. The CDF median is increased from -27 dBV for the flat surface to -1 dBV for the optimized surface, demonstrated a significant 26.0 dB improvement. This example shows that incident waves can be reflected towards four disconnected sets of directions simultaneously.

CDF values for OPT12, OPT13, OPT14, OPT15, OPT16, and OPT17 can be seen in Figure 3.26. Also, the electric field intensity distributions in the far zone are compared in Figure 3.25.

We finally summarize all optimization results in Table 3.3.

Figure 3.23: Far-zone electric field intensity distributions obtained by the reflections from the optimized surfaces OPT8, OPT9, OPT10, and OPT11.

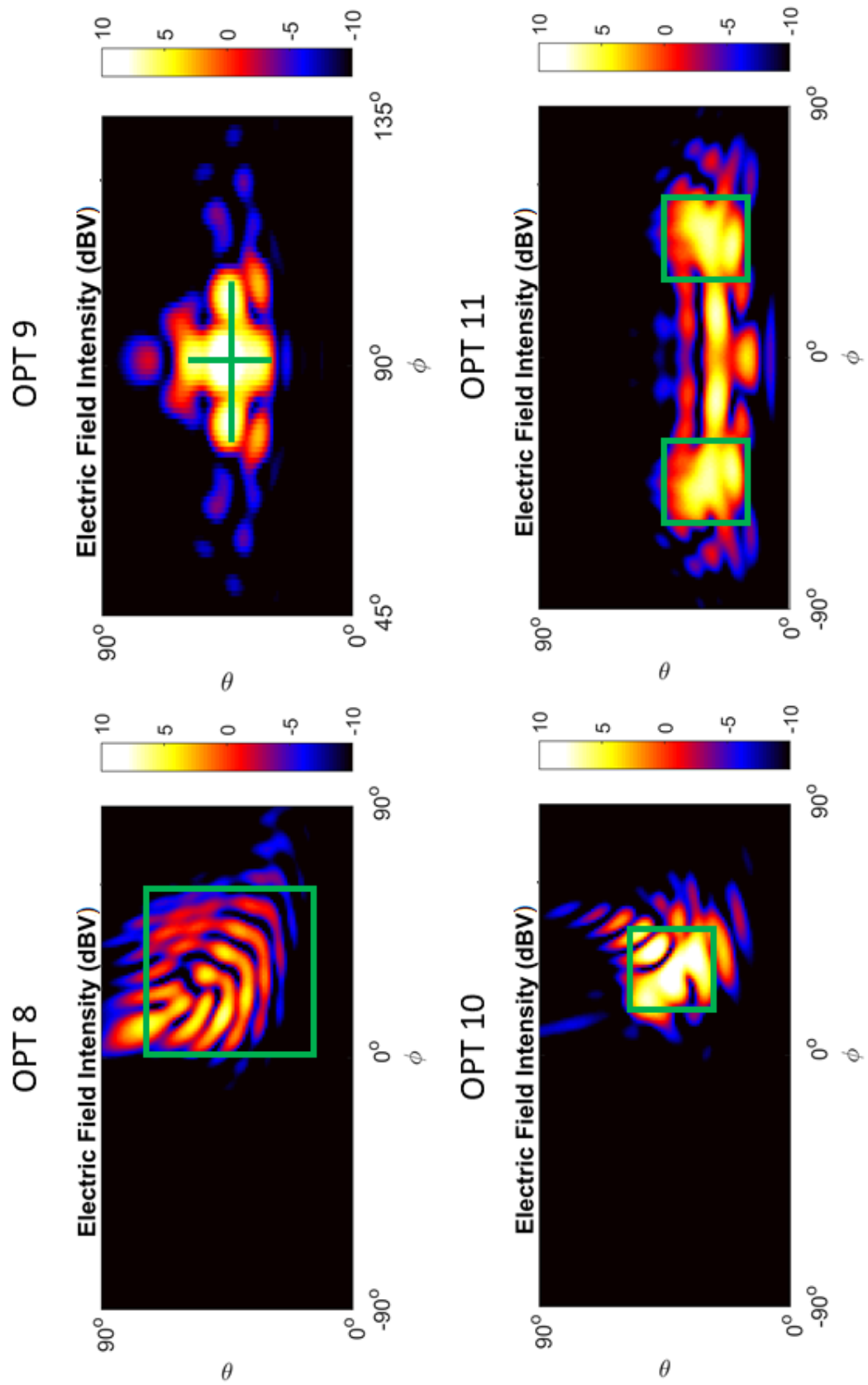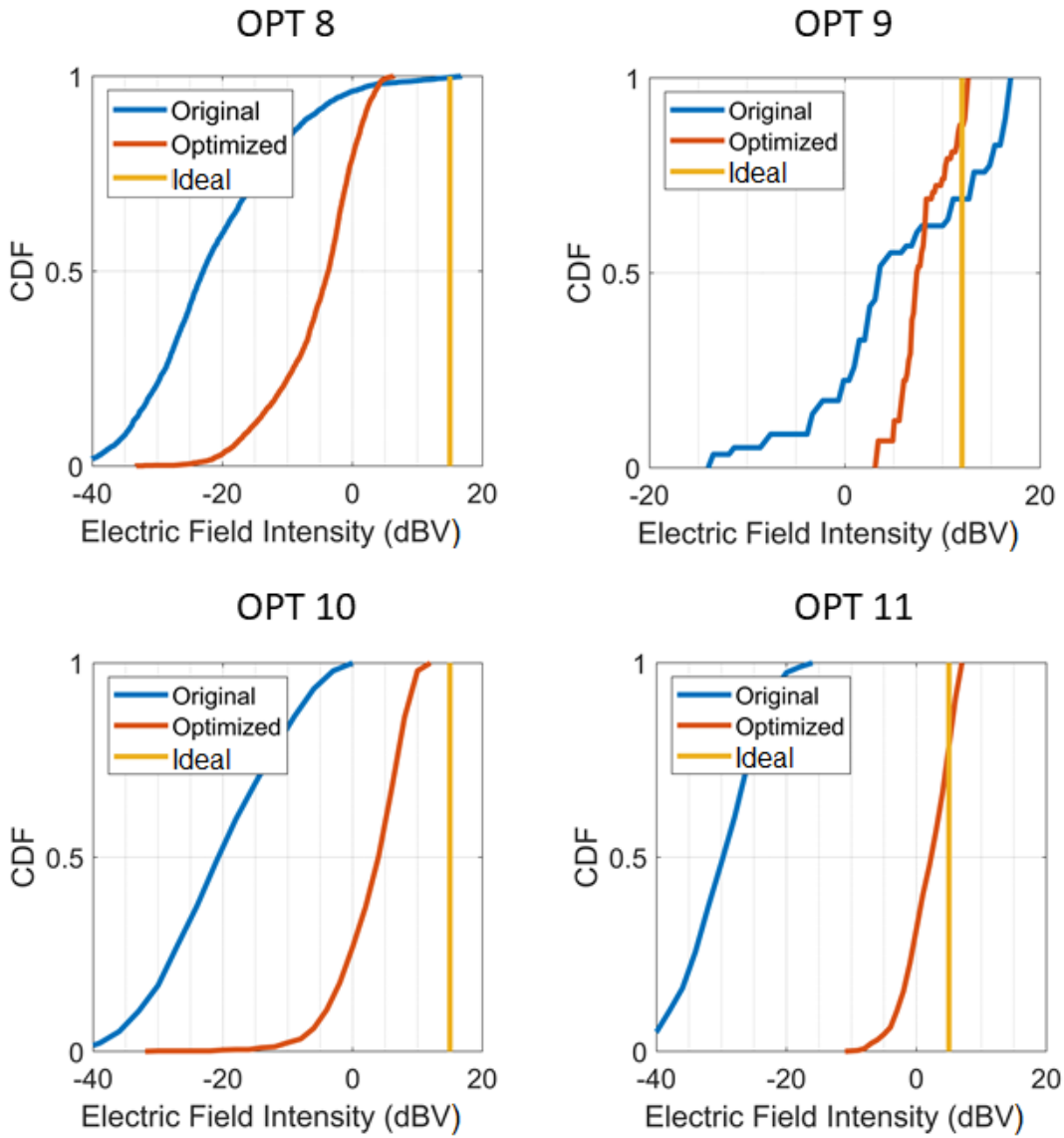Figure 3.24: CDF values for OPT8, OPT9, OPT10, and OPT11, in comparison to the CDF of the flat surface.
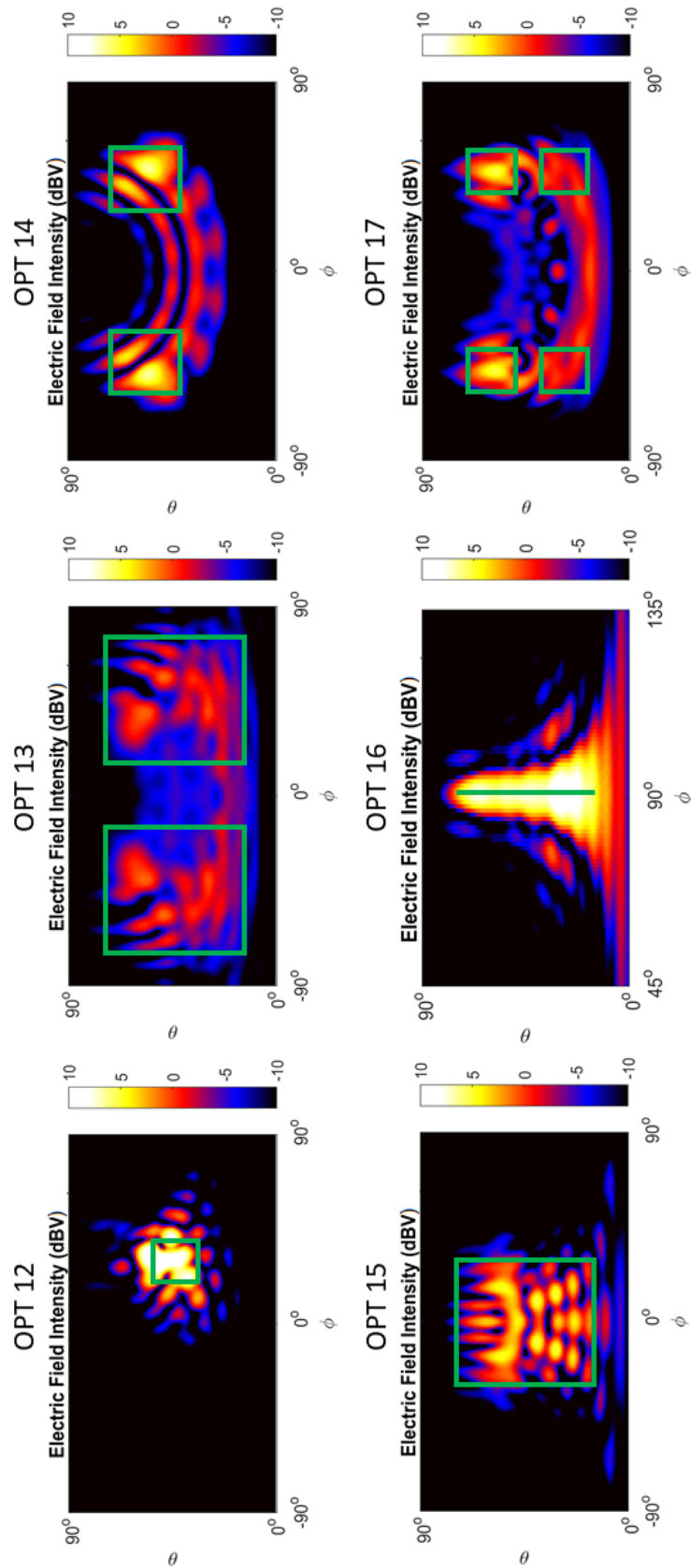
Figure 3.25: Far-zone electric field intensity distributions obtained by the reflections from the optimized surfaces OPT12, OPT13, OPT14, OPT15, OPT16, and OPT17.
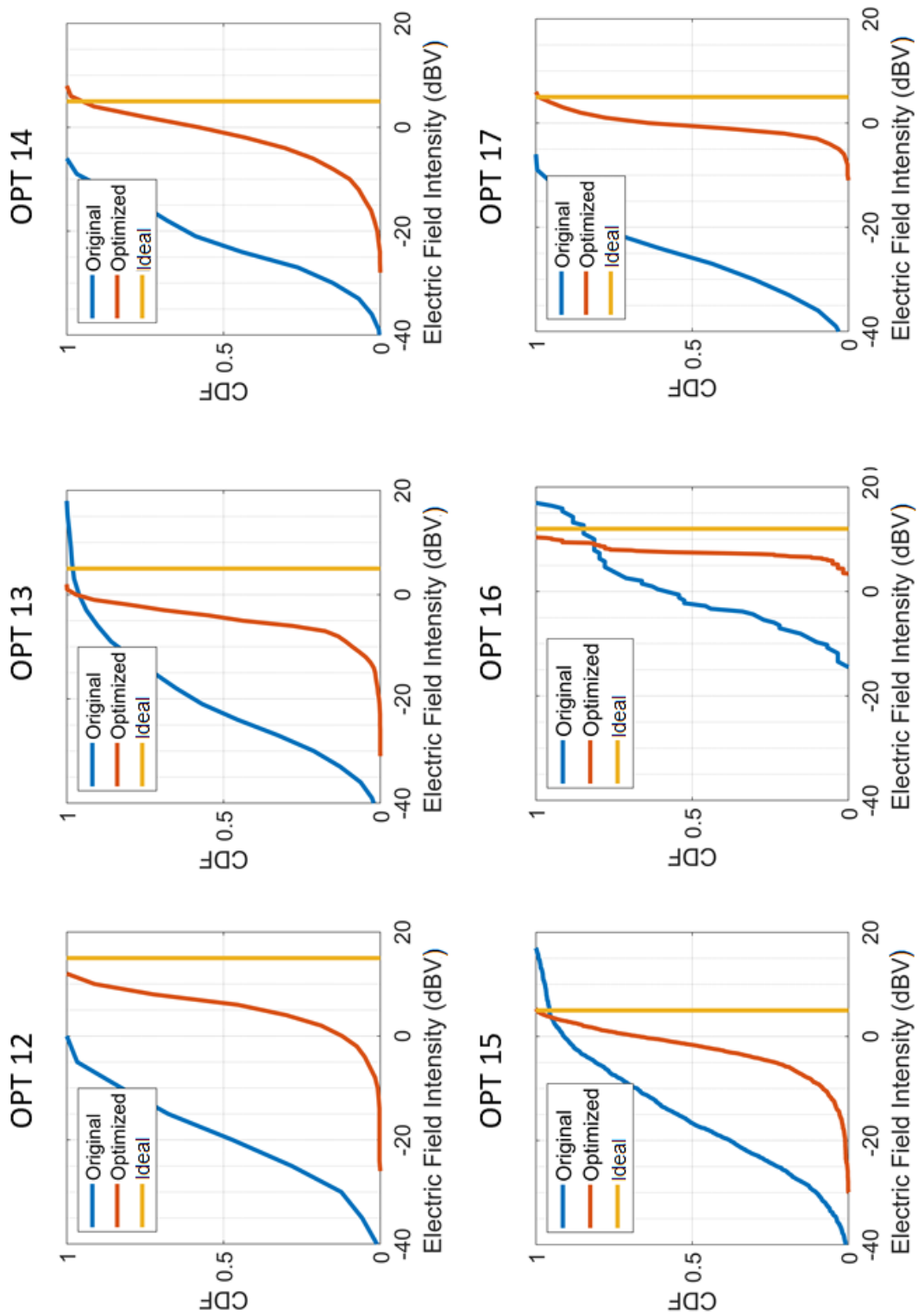
Figure 3.26: CDF comparisons of various optimizations (OPT12, OPT13, OPT14, OPT15, OPT16, OPT17).

Table 3.3: Optimization Results

OPTIMIZATION	THETA (degree)	PHI (degree)	FIELD (dBV)	MEDIAN GAIN (dBV)	VARIANCE (dBV)
OPT1	45 ± 15	90± 0	12	6.8	1.8
OPT2	45± 15	90± 0	12	6.4	5.3
OPT3	45± 15	90± 0	12	6.6	5.1
OPT4	45± 15	90± 0	12	6.6	3.8
OPT5	45± 0	0± 30	12	11.3	5.5
OPT6	45± 15	90± 0	5	0.9	0.6
OPT7	45± 0	0± 30	5	8.9	1.1
OPT8	45± 30	30± 30	15	19.2	0.0
OPT9	45± 30	90± 0	12	10.0	9.4
OPT10	45± 30	30± 15	15	25.0	0.0
OPT11	30± 15	45± 15	5	32.0	0.0
OPT12	45± 10	30± 10	15	25.2	0.0
OPT13	45± 30	45± 30	5	19.0	0.0
OPT14	60± 15	45± 15	5	22.0	0.0
OPT15	45± 30	0± 30	5	15.1	0.0
OPT16	45± 30	90± 0	15	10.1	6.9
OPT17	(30,60)± 10	45± 10	15	26.0	0.0

3.8 Near Field Analyses for Selected Designs
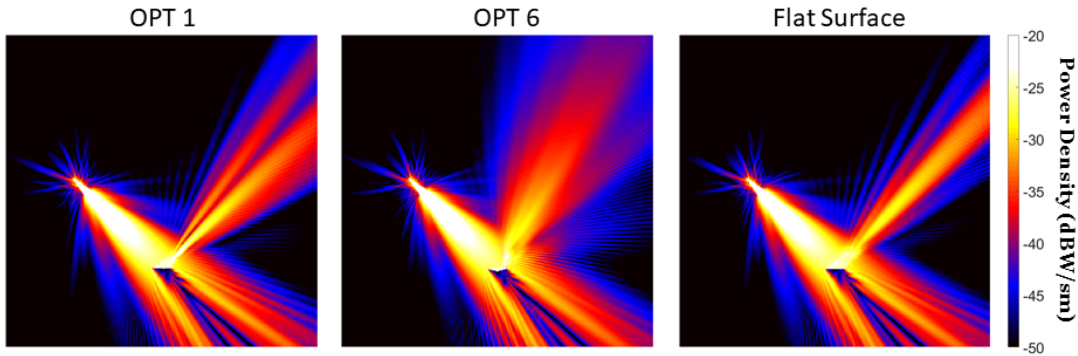
Figure 3.27: Power density distributions when OPT1 (left), OPT6 (middle), and flat surface (right) excited by a horn antenna.

Up to this point, optimization and analyses of the designed reflectors based on far-field values are presented. At the same time, it can be interesting to observe how reflected waves behave around the reflecting surfaces.

In Figure 3.27, the near-zone power density distributions are shown for OPT1 (left), OPT6 (middle), and a flat surface (right) when they are excited by a tilted horn antenna. It is observed that the reflected fields and the produced patterns strongly depend on the types of the reflector. For example, using reflectors OPT1 and OPT6, surfaces reflect incident waves uniformly in larger areas, as they are designed for this purpose, while the flat surface confines the waves into a narrower area.

In Figure 3.28, reflected fields (power density values) are observed when a large flat plate is placed below OPT6. The inserted plate is also PEC. It is observed that, as the plate is placed closer to the optimized reflector (OPT6), its reflection characteristics significantly deteriorate and deviate from the desired characteristics obtained via optimization.

Finally, in Figure 3.29, near-field plots for dual reflector setups are shown (on top) in comparison to the single reflector setups (at the bottom). It is observed that the optimized reflectors behave as desired, even when they are not directly illuminated but used as second reflectors. These results demonstrate the effectiveness of the designed

reflectors that can be used in alternative configurations to generate diverse mm-wave pathways.
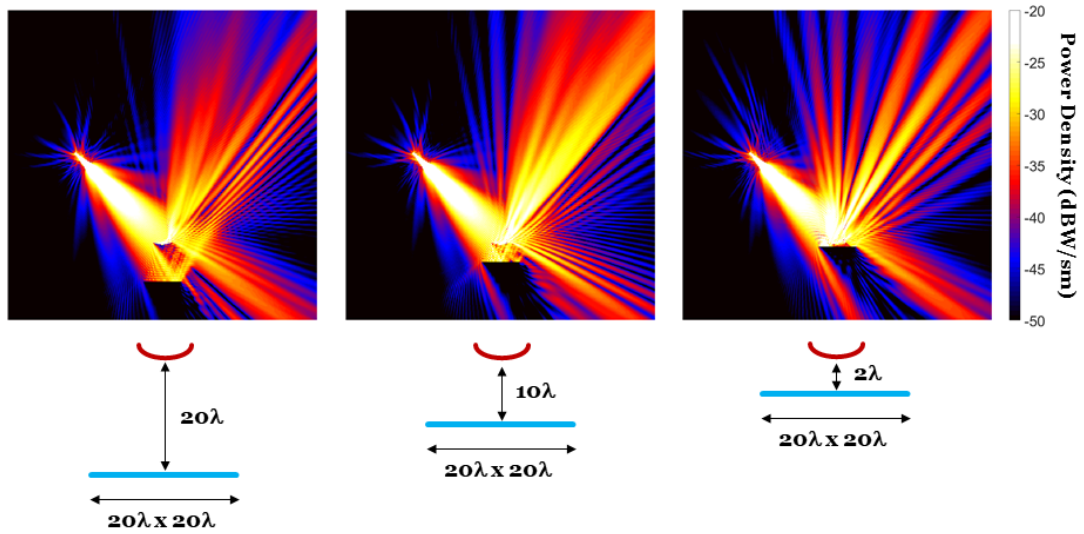
Figure 3.28: Power density distributions when OPT6 is placed above a large flat surface (at various distances) and excited by a horn antenna.
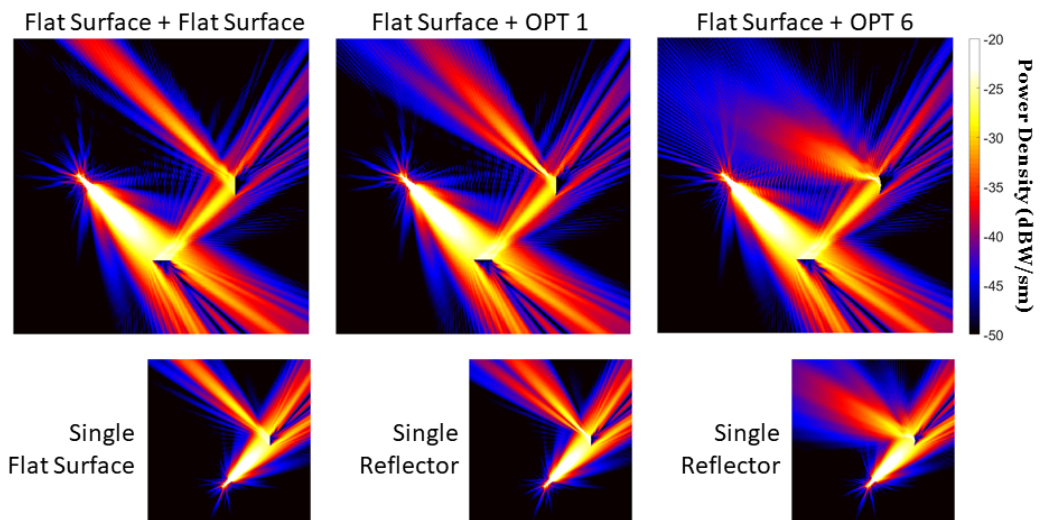
Figure 3.29: Power density distributions when two flat surfaces (left), OPT1 and a flat surface (middle), and OPT6 and a flat surface (right) are used as a system to redirect the excitation by a horn antenna.

In this chapter, we first present an initial surface to be optimized together with funda-

mental optimization parameters. Then, an optimization result is investigated in detail in terms of field distribution, CDF, and other performance metrics to demonstrate the our assessment procedures for the designs. Then, various optimization results are presented to illustrate different aspects, such as the optimization stability, effect of fitness function, and capability of the optimization mechanism for various design goals. In the next chapter, the fabrication method is presented together with measurement results of two optimized surfaces, namely OPT1 and OPT6.

CHAPTER 4

FABRICATION AND MEASUREMENT OF THE DESIGNED REFLECTORS

In this chapter, an adaptive and low-cost fabrication method for the designed reflecting surfaces is presented together with measurement results.

4.1 Fabrication of the Designed Reflectors

In this study, reflectors are designed to be used in physical applications; thus a reliable fabrication method is necessary to realize them. Various techniques can be used to fabricate such reflectors, from shaping aluminum blocks using computer numerical control (CNC) machines or metal casting to additive manufacturing techniques such as 3D printing.

Cost and energy efficiency are critical design features for devices to be used in 5G mm-wave applications, since the numbers required elements in a 5G mm-wave network are substantially higher than those in the existing conventional networks. In this study, 3D printing method and conductive coating are employed to demonstrate the possibility of fabricating the designed reflectors with low costs and in a reliable manner.

4.1.1 Fabrication of Reflectors Using 3D Printing

In various applications, 3D printing can be used to fabricate a computer-aided design (CAD) without requiring industrial tools and complex manufacturing processes. This fabrication method has been used since the 1950s, and thanks to the rapid technological advancements in this area, it has become increasingly more popular and accessible

with inexpensive operating costs. As another major advantage, in addition to its low cost, 3D printing is highly adaptive; a unique geometry can be printed without altering the setup. Consequently, 3D printing is preferred as the fabrication method in this study. Selected reflectors among many are fabricated using generic 3D printers located in the Department of Electrical and Electronics Engineering at Middle East Technical University. The department has Ultimaker 2+ printers and polylactic acid (PLA) filaments in stocks. In this study, the filament type is not a critical parameter in terms of fabrication, since a printed surface is later coated with a conductive material. However, the compatibility of the conductive paint and the filament is particularly monitored to observe that the paint can be applied onto a printed sample without disastrous effects, such as melting or bending.

The printers have 0.25 mm nozzles as the finest option, indicating that the precision level in the produced prints is $\lambda/40$. In the simulation results (Figure 3.14), it can be observed that such an error rate on the surface does not deteriorate the reflecting performance of the optimized surfaces. Since using the finest option does not have any foreseeable disadvantage in terms of prototype fabrication, the reflectors are fabricated using the 0.25 mm nozzle that is the best option provided by the 3D printer setup.

The printer is shown when it is being used to print a reflecting surface (OPT1) in Figure 4.1. The entire process took about 22 hours for the 16.6 cm by 16.6 cm base-sized reflector, which has a center frequency of 18 GHz. A total of 120 grams of filament is used to fabricate the reflector, meaning that the resulting reflector is also lightweight. The final form of the fabricated reflector before applying the conductive paint is shown in Figure 4.2,

As previously discussed, the reflectors can be printed with a $\lambda/40$ error tolerance using the 3D printer. Such error level is small to disrupt the performance of a PEC reflector; but, it may lead to other issues in the coating stage. Specifically, such defects on the surface may cause nonuniform coating, resulting in poor performance of reflectors. A well-known method to remove small defects on a 3D-printed material is to apply sanding. Therefore, after printing, each surface is sanded with dry and wet sandpapers using two grit levels (a coarse and a fine one). In Figure 4.3 depicts

68

two printed samples, one of which is sanded (bottom) and the other one is not (top). The defects are effectively minimized on the sanded surface compared to its original (unrefined) version, allowing a more uniform coating.
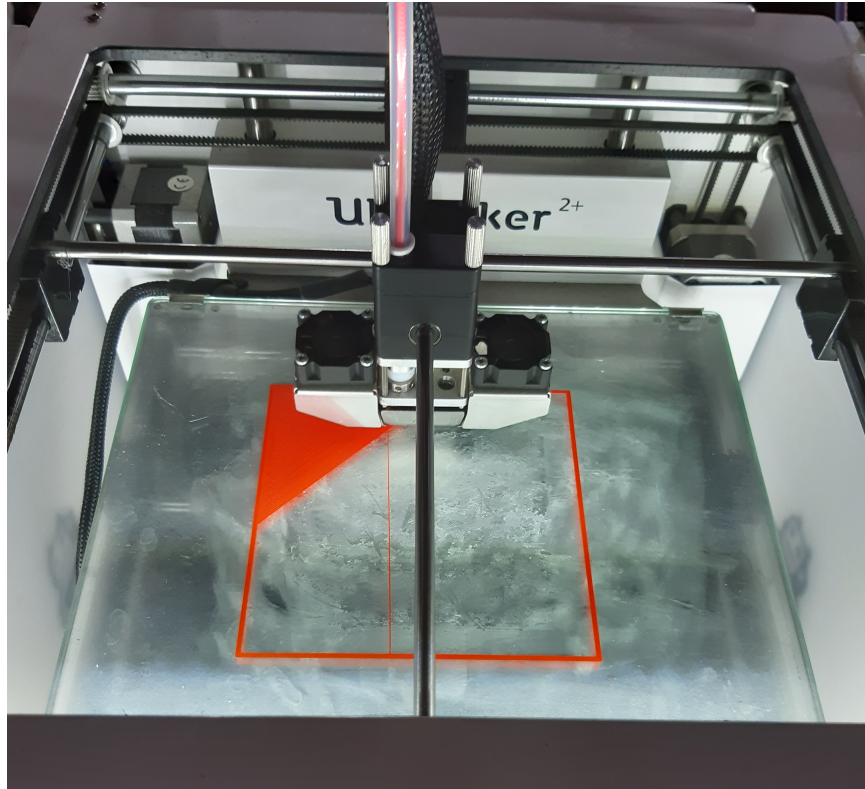

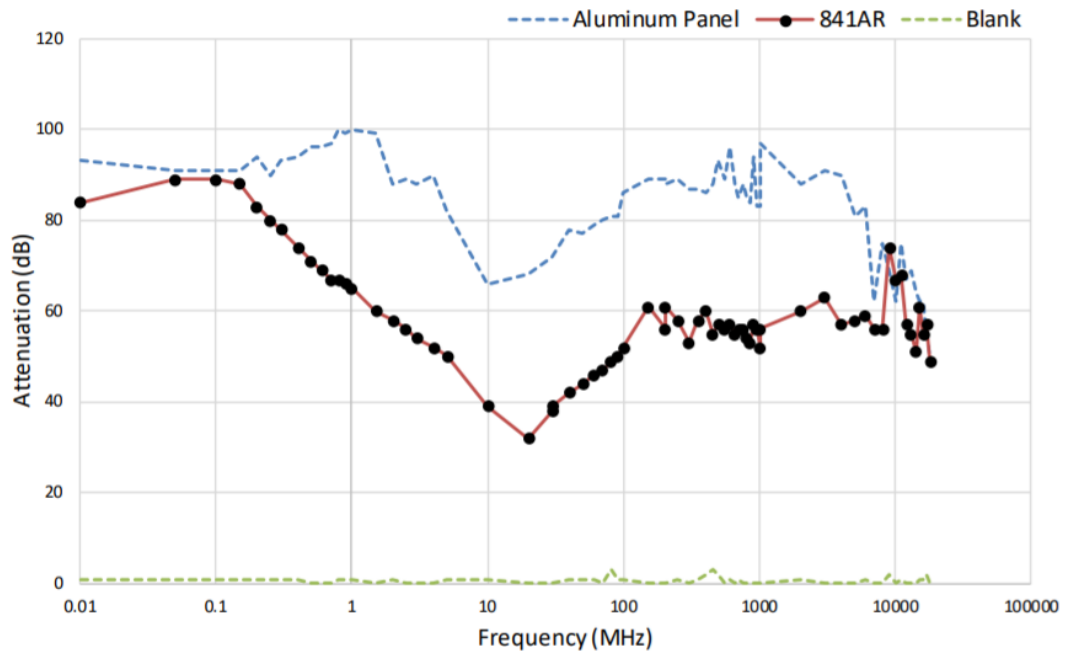Figure 4.1: Photograph of Ultimaker 2+ during the fabrication of a reflector.

Figure 4.2: A fabricated reflector (OPT1) before the conductive paint is applied.

Figure 4.3: Sample printed reflectors before (top) and after (bottom) sanding.

4.1.2 Application of Conductive Paint to Fabricated Samples

Test performed with a 2 coat thickness.

Figure 4.4: MG Chemicals Super Shield Nickel Conductive Coating Paint attenuation performance in comparison to aluminum panel. Image is taken from the datasheet prepared by the manufacturer.

Using a 3D printer, the surfaces with optimized surfaces are produced from a dielectric material (PLA) and cannot be used directly as reflectors in mm-wave applications. Therefore, a type of conductive paint is applied to the fabricated bodies to obtain highly conductive and reflective surfaces. MG Chemicals Super Shield Nickel Conductive Coating Paint (841 AR Aerosol) is chosen as the coating material. According to the manufacturer, this conductive paint promises to provide high conductivity on the applied surface from static (DC) up to mm-wave frequencies, as shown in Figure 4.4. In the figure, attenuations for shielding applications are compared for aluminum and conductive-paint-applied surfaces. This comparison can be considered as a milestone on the fabrication of the reflectors in this thesis study, as it demonstrates the feasibility of using conducting paints on 3D-printed samples rather than shaping hard metallic surfaces to realize the designed reflectors.

Before applying the paint on the reflectors, however, additional tests are conducted to verify the sufficient reflectivity of the conductive paint. For this purpose, a 30 cm by 30 cm aluminum plate and a similar-size acrylic glass plate with two-layer conductive paint are tested from 17 GHz to 20 GHz in terms of their reflection capabilities. In Figure 4.5, the test setup including the measured plates is shown, while in Figure 4.6, reflection performances of the two plates in reference to the surrounding noise are demonstrated. In these measurements, it is concluded that the coated aluminum plates show similar reflection (overall transmission from the transmitter antenna to the receiving antenna via reflection) characteristics. Based on this and similar experiments, the conductivity of the paint is found to be sufficient to realize the final reflectors by applying it onto the surfaces of the 3D prints.

After the verification of its effectiveness, the conductive paint is applied to the 3D-printed surfaces. In each case, the paint is applied as two layers with a 3-minute waiting time between the applications, and the coated reflectors are rested for one day before measurements, as suggested by the manufacturer. A coated reflector (OPT1) is shown in Figure 4.7 from different directions. DC measurements show that the corner-to-corner resistance is under 5 ohms from a corner to the diagonal corner across a printed surface.

It is also possible to cover the 3D prints with other materials, even with aluminum papers, to reach conductive surfaces, while using conductive paints seems to be an effective option, especially considering their applicability while being relatively inexpensive.

As previously discussed, the optimized surfaces can be scaled to any frequency of operation within the mm-wave range. Figure 4.8 depicts two scaled versions of the same design, i.e., the smaller version for 24 GHz (left) and the larger version for 18 GHz. Both structures are fabricated with the same printing settings, sanded, and coated with two layers of conductive paint. The functionality of both reflectors demonstrates the feasibility of the overall fabrication process for different frequencies in accordance with the target mm-wave application.
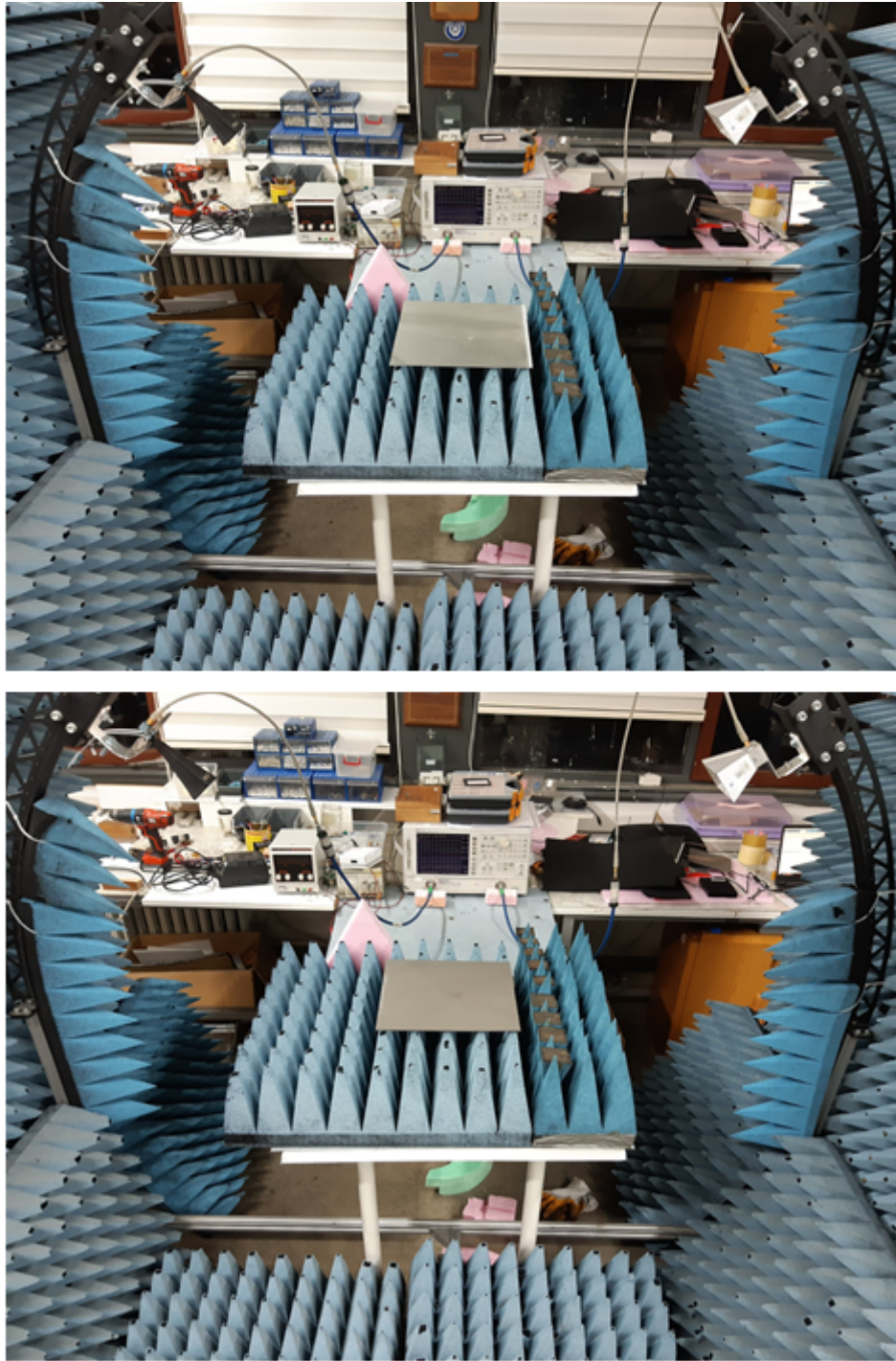
Figure 4.5: Test setup for measuring the conductivity and reflection performance of the paint. Top and bottom photographs show aluminum plate and conductive-paint-applied glass plate, respectively, in the test setup.
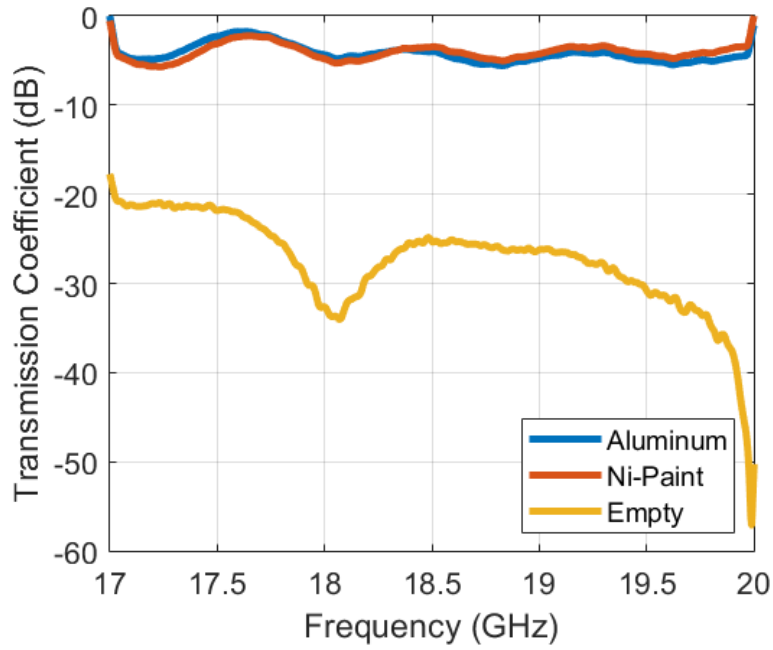
Figure 4.6: Comparison of the antenna-to-antenna transmission (see Figure 4.5) via reflection from an aluminum panel and a glass plate with conductive paint. Values are shown also for empty case, i.e., in the absence of any reflector.

Figure 4.7: Photographs of a reflector (OPT1) obtained by using conductive paint on a printed surface viewed from different directions.
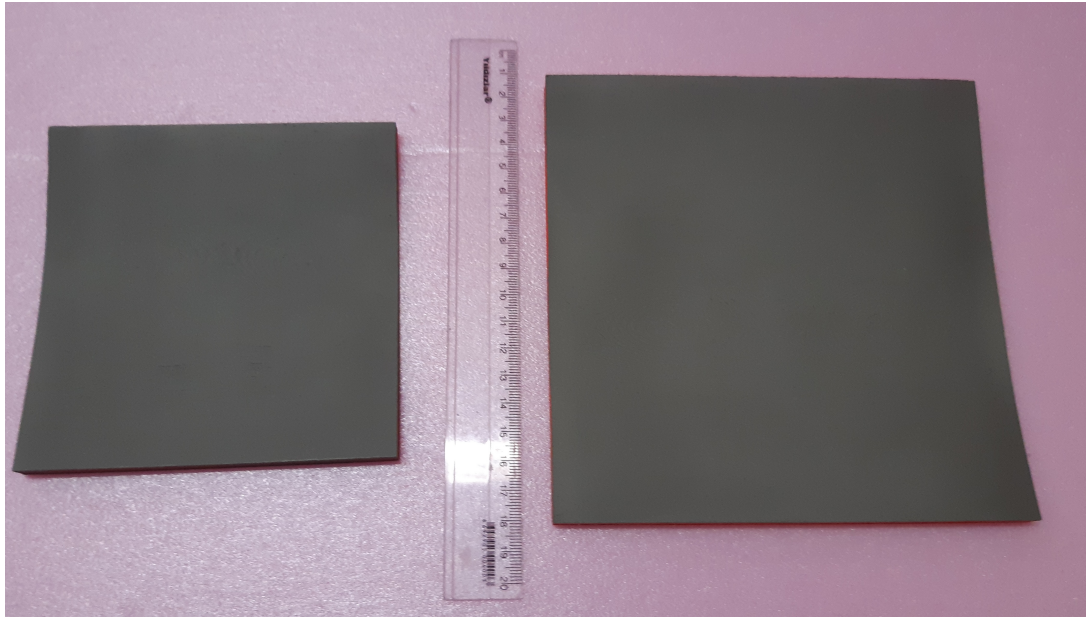
Figure 4.8: Photographs of two reflectors based on the same design (OPT1) to operate at 24 GHz (left) and 18 GHz (right).

4.2 Measurements

After fabrications are completed, the fabricated reflectors are measured using two different measurement setups. In the next section, these measurement setups are introduced, and measurement results a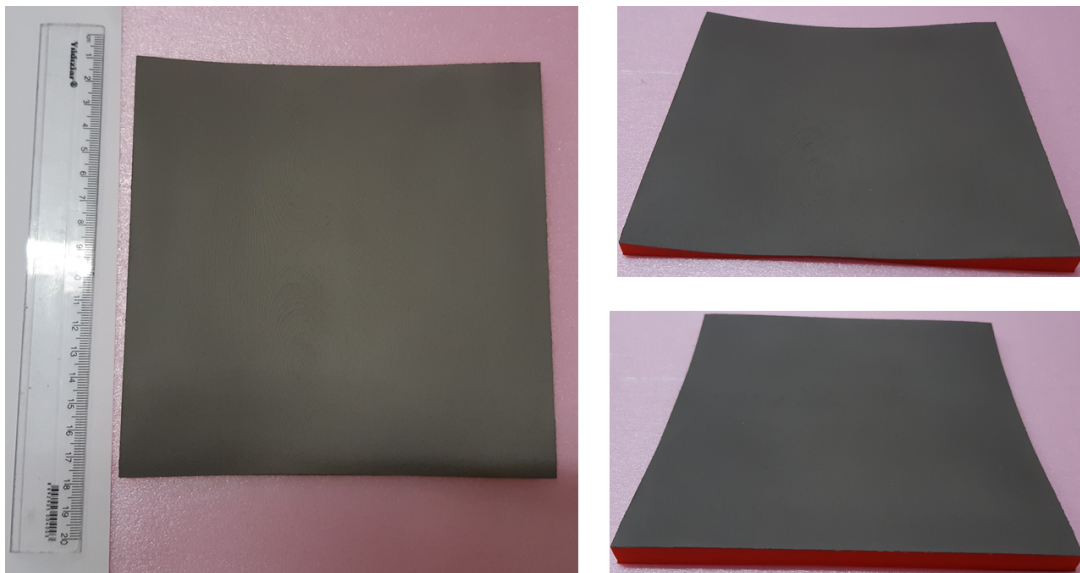re shown in comparison to the simulation results. We further discuss possible measurement errors that may explain the deviations of the measured values from the ideal simulation values.

4.2.1 Naval Radio Lab Arch Measurement Setup

NRL arch is designed for measuring free-space radar reflection coefficients of radar absorbing materials [37]. In this study, it is employed to measure the reflection behaviors of the designed reflectors. A schematic representation of the measurement setup based on the NRL arch is shown in Figure 4.9. In this setup, one antenna is used as a transmitter and the other is to receive the waves (signals) reflected from the investigated reflector, which is located at the center of the arch. We use this setup particularly to evaluate the reflection performance of a printed OPT1 reflector. Both antennas are directed toward the designed surfaces as described in 4.9. The trans-

75

mitting (radiating) antenna is fixed at $\theta = 45$ degrees, while the receiving antenna is moved from 30 to 60 degrees. Measurements are performed at every 2 degrees. The distance from each antenna to the reflecting surface is approximately 80 cm, corresponding to 50λ at 18 GHz. A sufficient isolation is necessary for accurate measurements; thus, absorbing materials are placed at suitable places in the measurement setup to suppress noises from the environment. A list of used equipment for measurements is given in Table 4.1, and a photograph of the setup can be seen in Figure 4.10.

Table 4.1: Equipment list for measurements in the NRL arch setup.

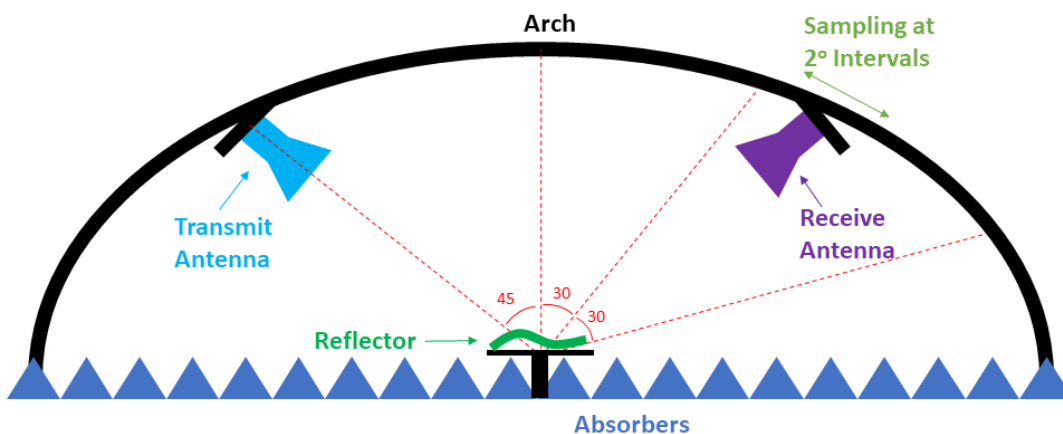| Vector Network Analyzer	Hewlett Packard 8720 D Network Analyzer 0.05-20 GHz
Antenna 1	Flann Microwave Standard Gain Antenna Model 2024-20 18-26.5 GHz
Antenna 2	ETS-LINDGREN Double Ridged Horn Model 3116 18-40 GHz
NRL Arch	NRL arch with 2 degree spacing

Figure 4.9: A schematic diagram of the NRL arch measurement setup.

Figure 4.10: A photograph of the NRL arch measurement setup.

4.2.2 Naval Radio Lab Arch Measurements

In the NRL arch setup, due to the physical dimensions of the NRL arch and the measurement frequency, the antennas and the reflector are not in the far-field regions of each other, but in their radiating near-field regions. Thus, an additional simulation that is more similar to the NRL arch measurement setup (where the antennas and the reflector are 50λ away from each other) is performed and included in the comparisons.

Comparisons of simulated and measured results for a flat reflector are shown in Figure 4.11. In this figure, the light gray lines represent individual measurements, while the red line represents the average of them. The light blue and dark blue lines denote the simulation results obtained with near-field conditions (as in measurements) and far-field conditions (as in optimization), respectively. We note that both measurement and simulation results are normalized, i.e., they are fixed at 0 dB transmission value from the transmitting antenna to the receiving antenna. It can be inferred from the

figure that the measurements are mostly in agreement with the simulations. The main differences are the slight shift of the main lobe and the absence of clear nulls in the measured results, which seem to be caused by measurement errors. Similar measurements are performed for OPT1 (the designed reflector) and the results are shown in Figure 4.12. We again observe consistent results, especially when comparing the measurement results with the near-field simulation that is based on the measurement scenario. In addition to measurement errors (e.g., imperfect positioning and orientation of antennas/reflector and unsuppressed noises from the environment), as in the case of the flat reflector, the differences between the measured and simulated results in Figure 4.12 are partially caused by the imperfect fabrication (e.g., imperfect conductivity and geometry) of the reflector.

For a better comparison of the results, Figure 4.13 depicts the normalized patterns obtained with measurements (average) and near-field simulations of the flat plate and the designed reflector (OPT1). Comparing the results for the flat plate and the optimized reflector, we observe the dramatic improvement provided by the reflector, which leads to a significantly more uniform distribution in the range of observation directions. In simulations, OPT1 shows only 6.4 dB difference between its maximum and minimum values over the interested directions (angles), compared to 23 dB difference for the flat reflector. These values become 10 dB and 16 dB, respectively, in the measurements. It can be concluded that the measurements using the NRL arch setup lead to less satisfying results compared to the simulations; however, there is still a 6 dB improvement in favor of the optimized surface, which achieves more uniform power distribution over the range of the observation angles.

In Figure 4.14, CDF values corresponding to the results in Figure 4.11 and Figure 4.12 are presented. Supporting our previous observations, CDF values clearly demonstrate that the transmission values are much more uniform throughout the desired set of directions using OPT1 instead of the flat plate. Obviously, measurement results represent less improvement from the flat plate to the designed reflector, due to both measurement errors and the deviation of the fabricated reflector from the ideal one. One particular disadvantage in the measurements is the absence of clear nulls in the flat plate, which show this unoptimized reflector much better than it is expected to be, so that the improvement via optimization seems less significant.
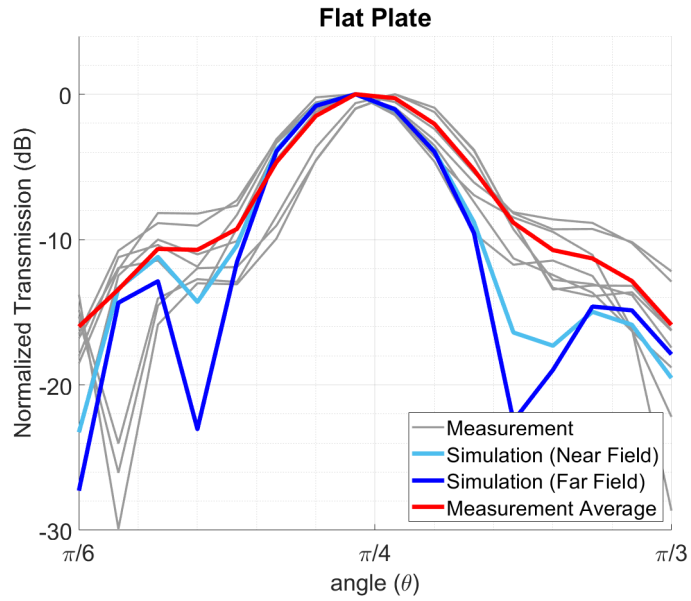
Figure 4.11: Measurement (NRL arch setup) and simulation results for a flat plate. Transmission refers to the normalized power received by the receiving antenna due to reflection from the plate that is illuminated by the transmitting antenna.

Figure 4.12: Measurement (NRL arch setup) and simulation results for OPT1 (designed reflector). Transmission refers to the normalized power received by the receiving antenna due to reflection from the reflector that is illuminated by the transmitting antenna.

Figure 4.13: Comparison of measurement (NRL arch setup) and simulation (near-field setup) results for the flat plate and OPT1.

Figure 4.14: CDF of the transmission patterns in Figure 4.11 and Figure 4.12

80

4.2.3 Free-Space Measurement Setup
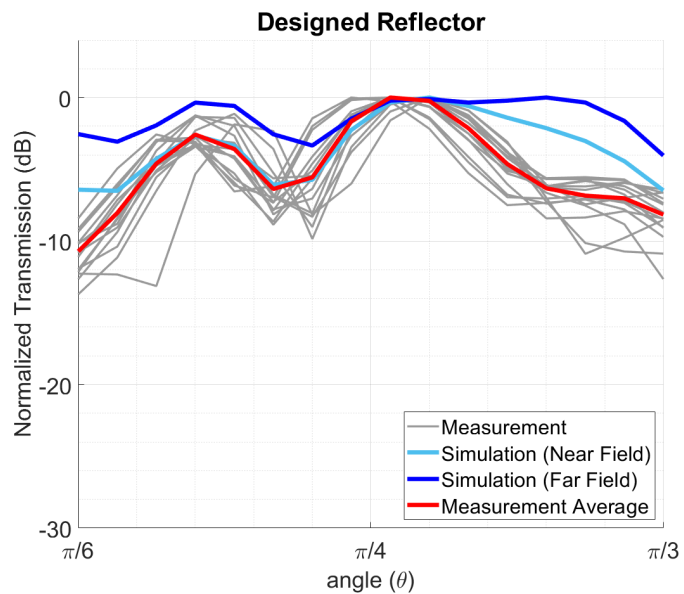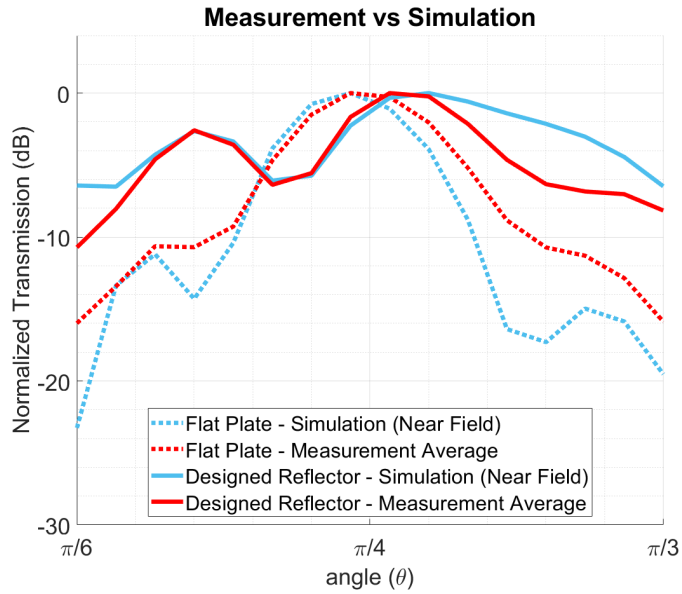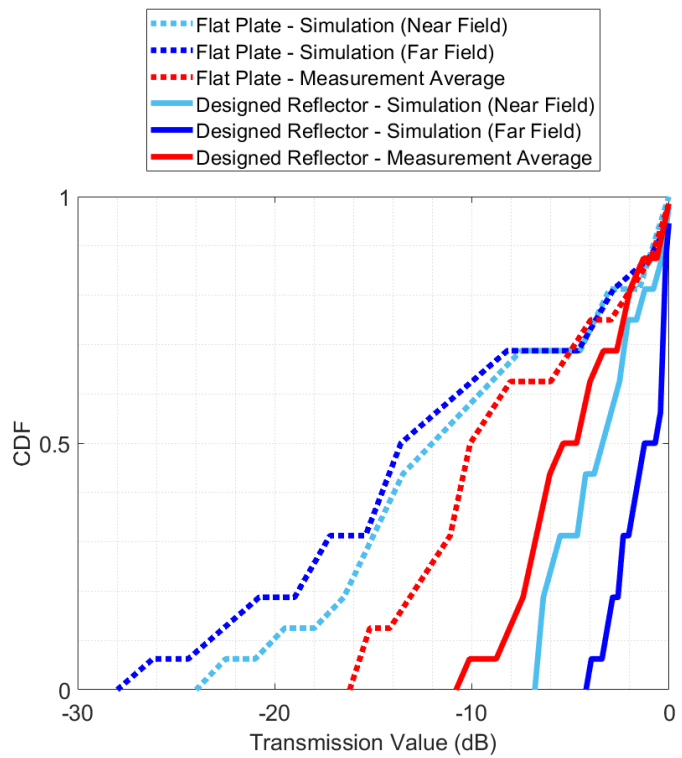
In an alternative measurement setup, the antennas and reflectors are located in an indoor environment without a physical connection (such as an arch). This measurement setup allows the antennas and the reflecting surface to be placed further away from each other, which is necessary to perform far-field measurements. A schematic diagram of the free-space measurement setup is shown in Figure 4.15. In the setup, two antennas are present to be used for transmitting and receiving waves (or signals), while the tested reflector is placed at the center. The radiating antenna is connected to a signal generator and the receiving antenna is connected to a spectrum analyzer. Both antennas are directed toward the reflector. Using this setup, OPT1 and OPT6, as well a flat surface as a reference, are measured. Transmitting (radiating) antenna is fixed at $\theta = 45$ degrees, while the receiving antenna is swept from 30 to 60 degrees. As opposed to the previous setup with 2-degree samples, measurements are performed at every 1 degree. The distance between each antenna and the tested reflector is 200 cm, corresponding to 120λ at 18 GHz. The antennas and the reflecting surface are placed at 130 cm height to minimize reflections from the ground. Absorbing materials are placed at suitable places to further suppress noise from the environment. As in NRL arch measurements, careful adjustments and repetitive measurements are performed to obtain accurate measurement results. A list of used equipment for measurements are given in Table 4.2, and a photograph of the test setup can be seen in Figure 4.16.

Table 4.2: Equipment list for measurements in the free-space setup.

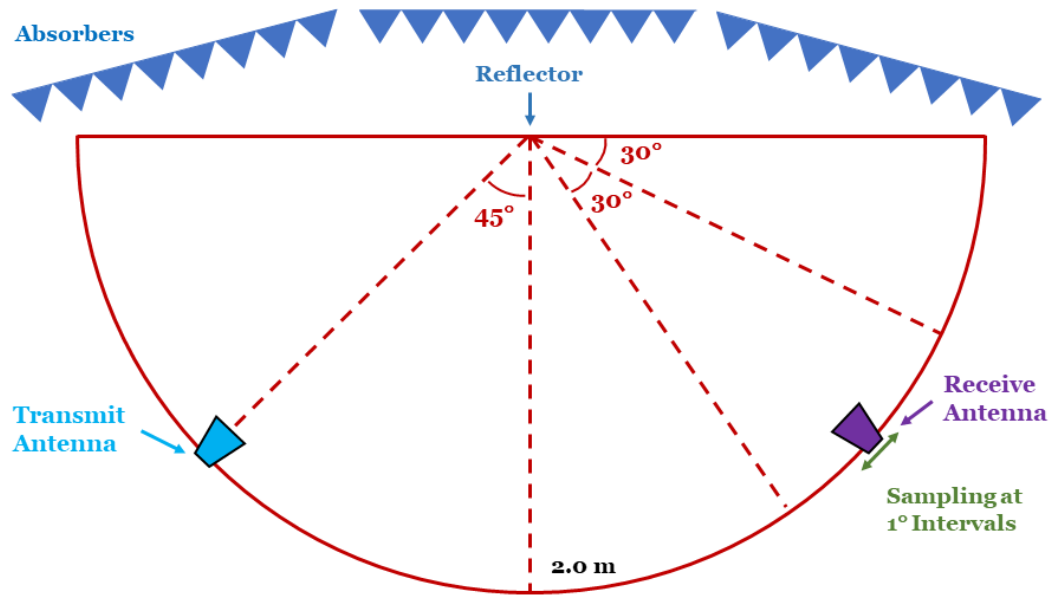|	
Signal Generator	Agilent Technologies E8257C PSG Analog Signal Generator
Spectrum Analyzer	Agilent Technologies E4408B ESA-L Series Spectrum Analyzer
Antenna 1	Flann Microwave Standard Gain Antenna Model 2024-20 18-26.5 GHz
Antenna 2	ETS-LINDGREN Double Ridged Horn Model 3116 18-40 GHz

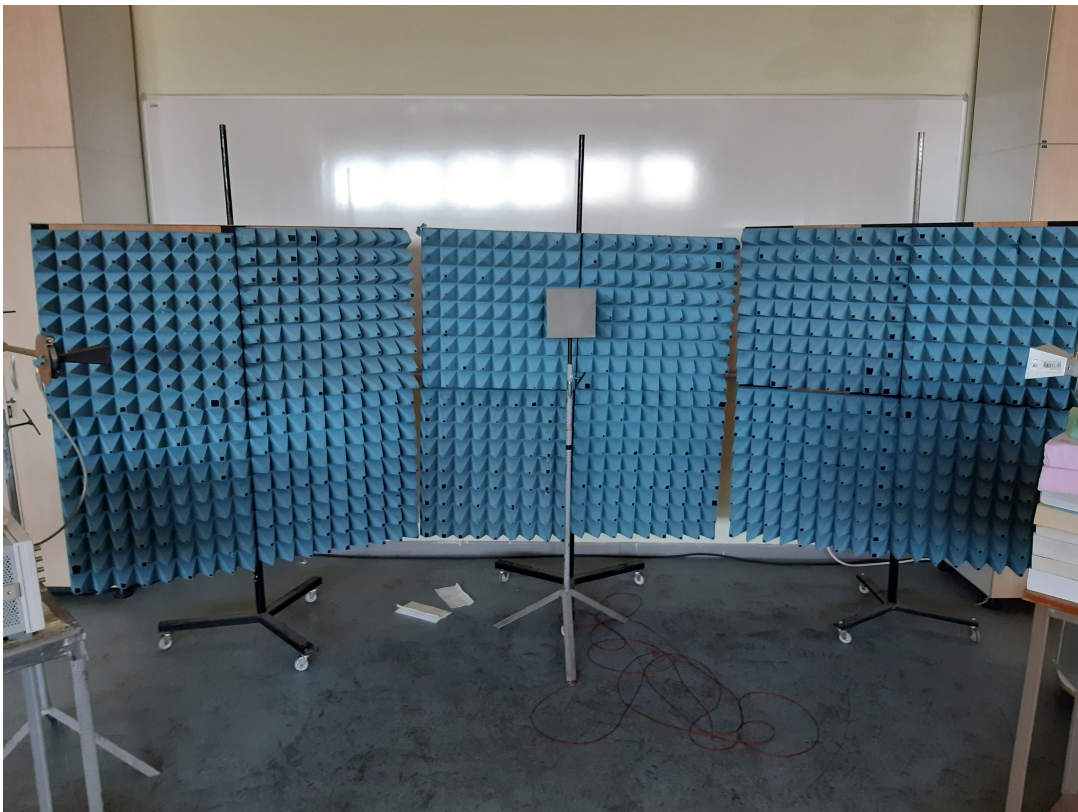Figure 4.15: A schematic diagram of the free-space measurement setup.

Figure 4.16: A photograph of free-space measurement setup.

4.2.4 Free-Space Measurements

4.2.4.1 Free-Space Measurements for OPT1 in Comparison to the Flat Surface

Simulation and measurement results for the flat and designed (OPT1) reflectors are shown together with the measurement of the environment noise in Figure 4.17. In this figure, the red lines represent measurement results, the light blue lines represent simulation results obtained with measurement setup conditions, and the blue lines show simulation results using optimization conditions (plane-wave incidence). Furthermore, the dotted lines represent the results for the flat plate, while the solid lines are for OPT1. It can be observed that the measurements are in good agreement with the simulations. Far-field and near-field simulations are also more consistent, in comparison to those for the NRL arch setup, due to the longer distances between the antennas and reflectors in the free-space measurement setup.

CDF values corresponding to the results in Figure 4.17 are presented in Figure 4.18. In far-field simulations, the variation of the transmitted power in the measured plane is reduced by 28 dB. This number is 22.1 dB in the near-field simulations, and 13.2 dB in the measurements. In comparison to the results obtained with the NRL arch setup, the measurement results are more promising, indicating the importance of placing the antennas and the reflector in the far zone of each other. On the other hand, the nulls for the flat reflector are still absent in the free-space measurements, leading to an underrated improvement by the designed reflector.

In Figure 4.19, measurement and simulation results for the CDF of the flat and OPT1 reflectors are shown at different frequencies. It is observed that, in the considered range of frequencies, the measurements are in well agreement with the simulations. The CDF mean of the designed reflector is always higher than that of the flat surface, demonstrating the effectiveness of the designed reflector in a wide range of frequencies.

Lastly, in Figure 4.20, CDF values for the designed reflector are compared when the reflector is illuminated by the original (optimization) polarization and a perpendicular one. It can be observed that the change in the polarization does not affect the reflection characteristics, as previously demonstrated via simulations.
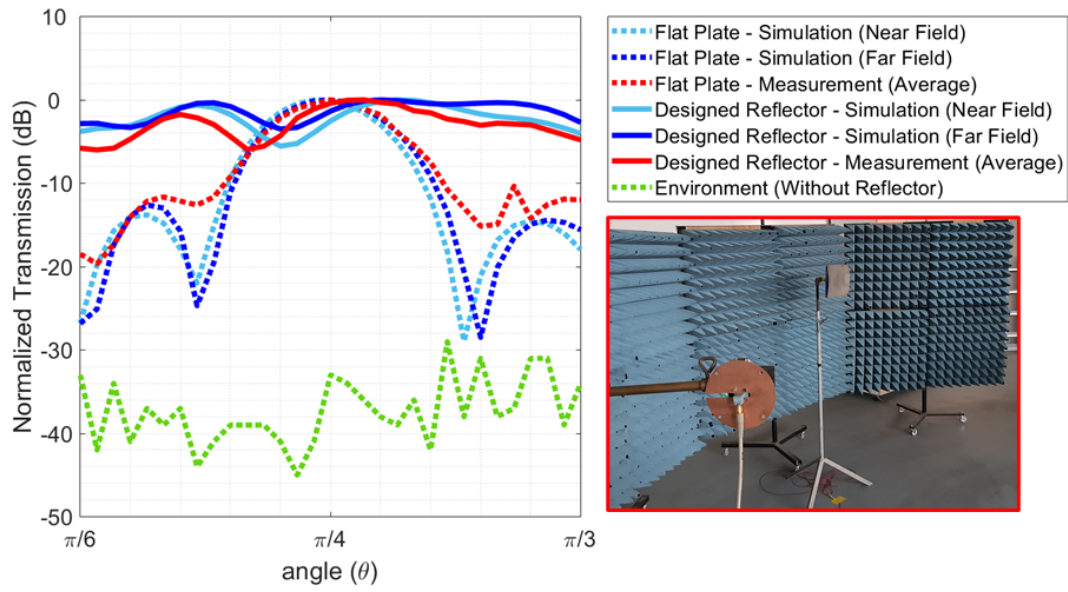
Figure 4.17: Measurement and simulation results for the flat and OPT1 reflectors using the free-space setup.
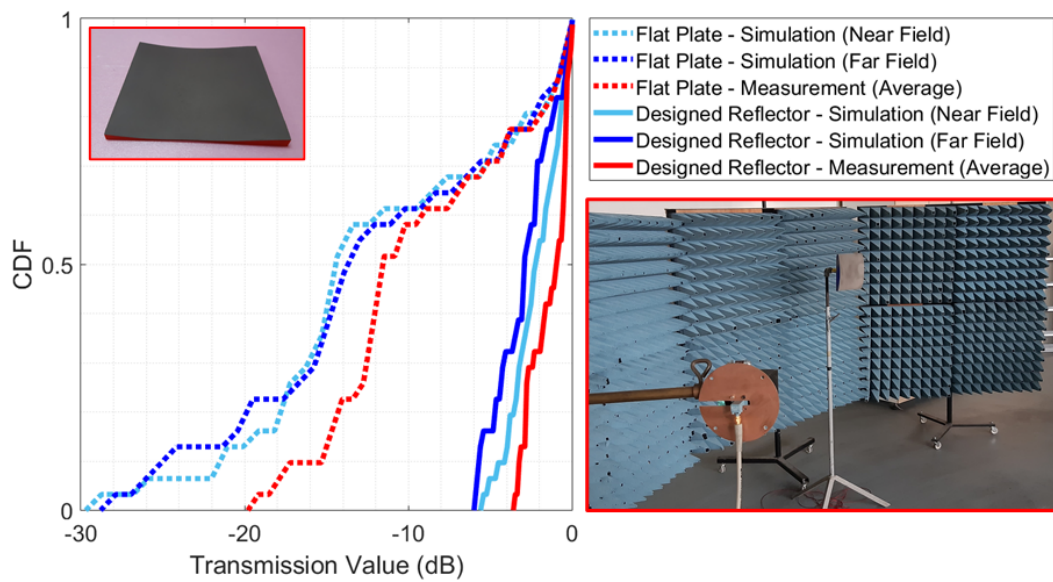

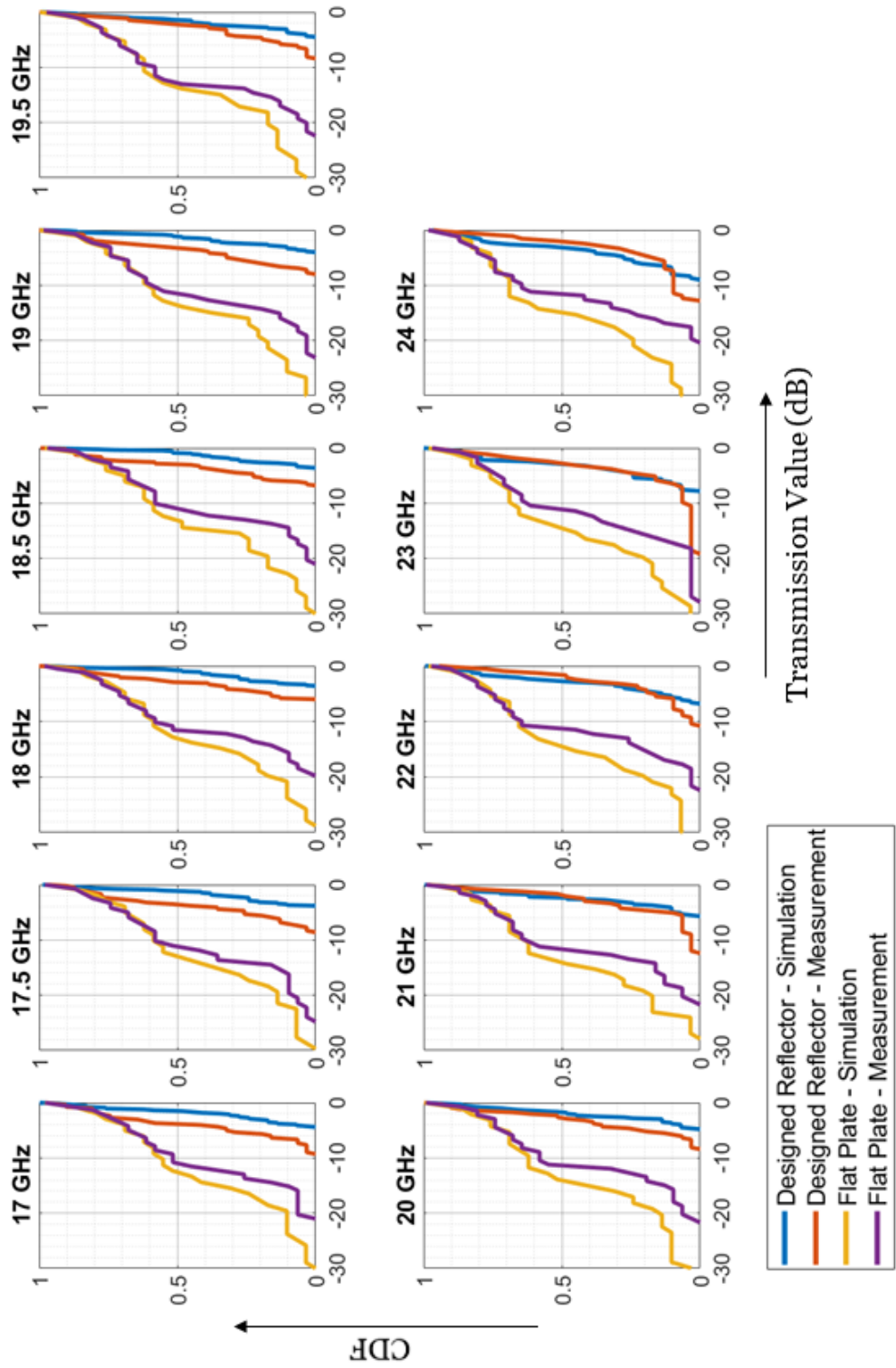Figure 4.18: CDF of the transmission patterns in Figure 4.17.

Figure 4.19: CDF of the transmitted power over the measured planes from 17 to 24 GHz for the flat and OPT1 reflectors.
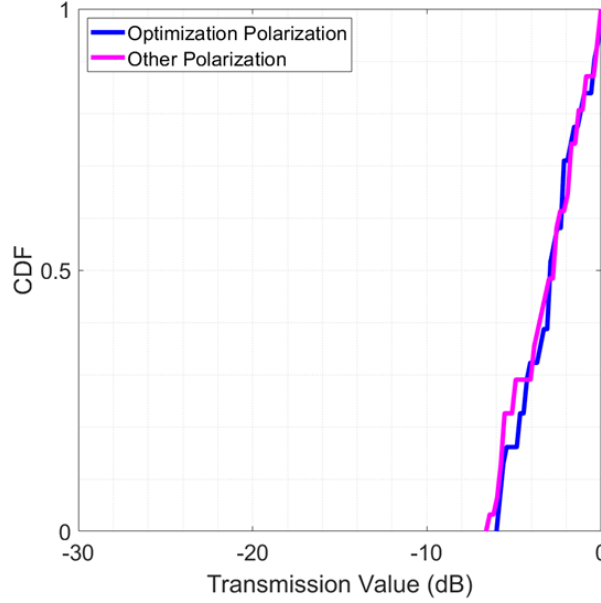
Figure 4.20: CDF of OPT1 when it is illuminated by the original (optimization) polarization and a perpendicular polarization.

4.2.4.2 Free-Space Measurements for OPT6 in Comparison to the Flat Surface

In Figure 4.21, simulation and measurement results for the flat and designed (OPT6) reflectors are presented together with the measured environment noise. The corresponding CDF values are shown in Figure 4.22. The variation of the transmitted power over the measured plane is reduced by 28 dB, 25.6 dB, and 17 dB by using OPT6 instead of the flat reflector, considering far-field simulations, near-field simulations, and measurements, respectively. In Chapter 3, the CDF values for OPT1 and OPT6 are compared (Figure 3.22) in the context of the effect of the fitness function on optimization results. It is presented that a more uniform field (or power) distribution is possible by targeting a lower field value (OPT6 in comparison to OPT1). The better performance of OPT6 is now clearly visible in the measurement results, e.g., with an almost flat curve in Figure 4.21.

Similar to the results for OPT1 using the free-space setup, measured and simulated CDF values for the flat and OPT6 reflectors at different frequencies are presented in Figure 4.23. It is once again observed that throughout the measured frequency band, the optimized reflector is superior to the flat surface in terms of achieving a uniform

86

power distribution.

Finally, the polarization sensitivity of the designed reflector (OPT6) is presented in Figure 4.24. Once again, the reflector maintains its good performance when the transmitting antenna is rotated by 90 degrees around its axis.
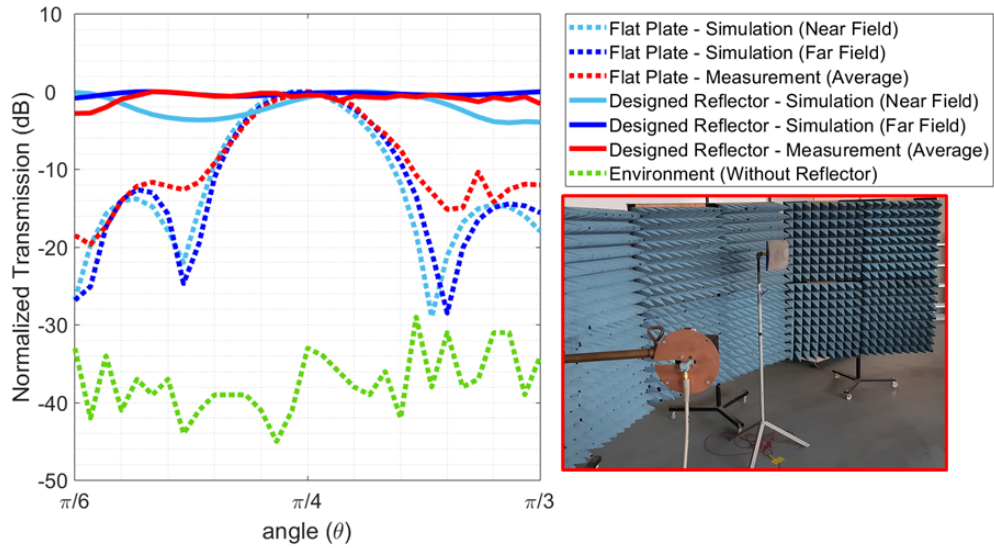

Figure 4.21: Measurement and simulation results for the flat and OPT6 reflectors using free-space setup.
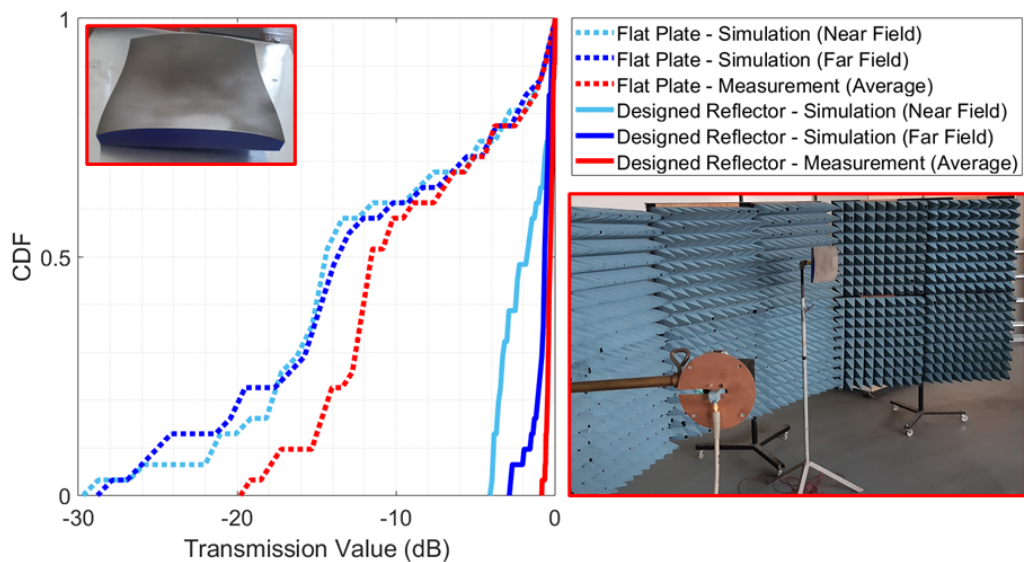

Figure 4.22: CDF for the transmission patterns in Figure 4.21.
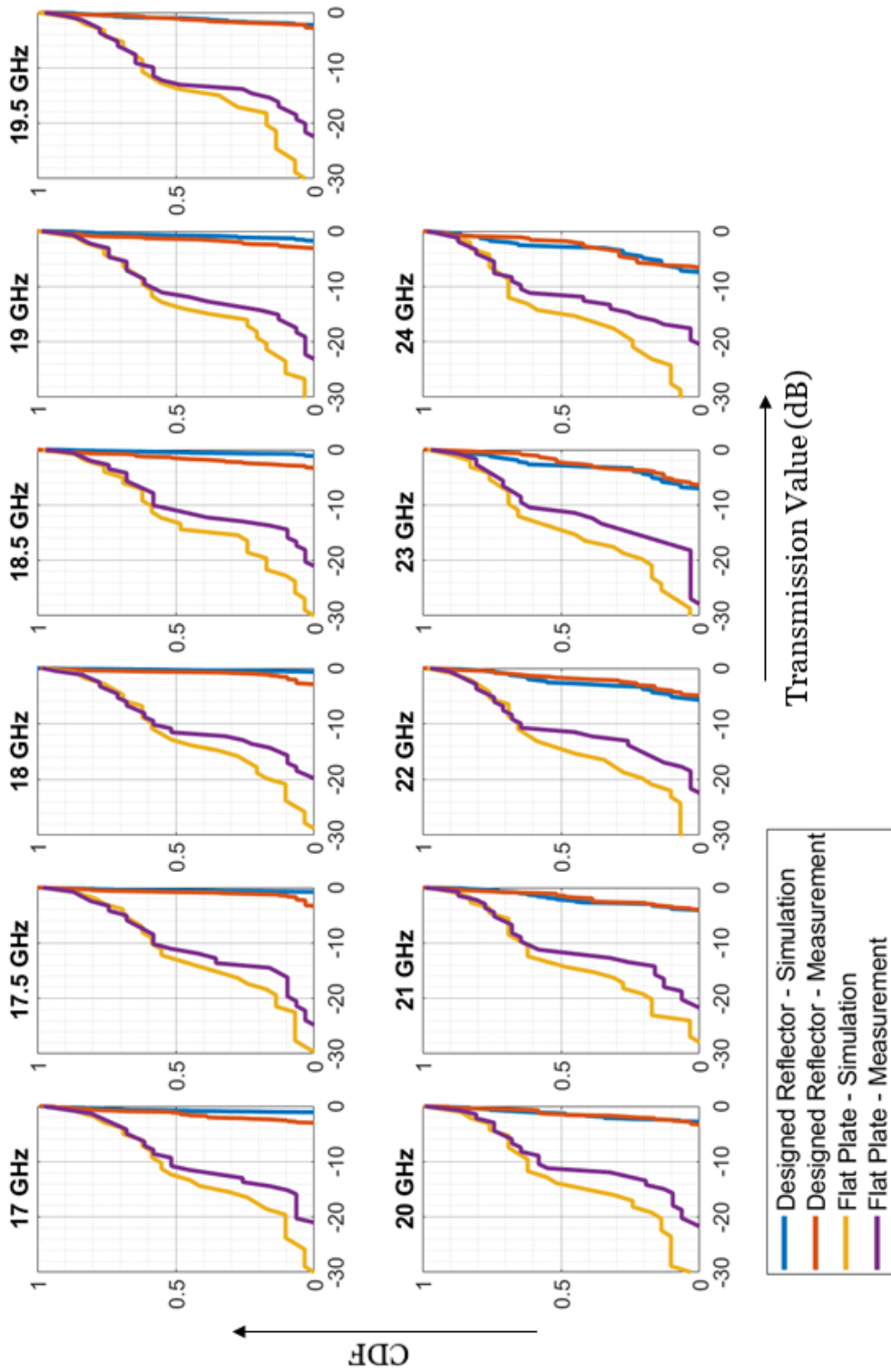
Figure 4.23: CDF of the transmitted power over the measured planes from 17 to 24 GHz for the flat and OPT6 reflectors.
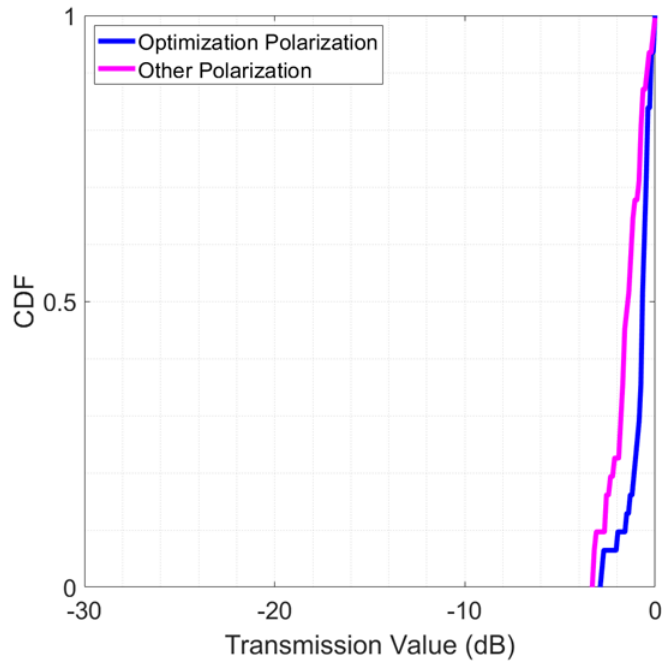
Figure 4.24: CDF of OPT6 when it is illuminated by the original (optimization) polarization and a perpendicular polarization.

4.2.5 Measurement Discussions

So far, it is demonstrated that the designed reflectors successfully operate as designed and they always outperform flat reflectors. On the other hand, the measurement results deviate from the corresponding simulation results due to several reasons.

First, due to the relatively high frequency (18 GHz), the antennas and reflectors must be placed with high precisions, and even sub-cm misplacements cause visible deviations in the results. In both measurement setups, to minimize such errors due to the misplacement of the components, multiple measurements are conducted, while this strategy does not always provide perfect results (e.g., for the nulls of the flat plates).

Second, as in most electromagnetic measurements, there is always unavoidable noise from the environment. To address this problem, absorbing materials are placed where possible, and the measurement environment is kept isolated as much as possible. However, absorbers are not enough to suppress all unwanted waves or signals during measurements, e.g., even the used measurement equipments are sources of re-

flections. In Figure 4.25 and Figure 4.26, antenna-to-antenna transmission values without any reflecting surface are shown for the NRL arch and free-space setups, respectively, together with measurements with reflectors. It is observed that, in the NRL arch setup, such no-reflector transmissions are significant near 60 degrees and they naturally contaminate measurements in such directions. In the free-space setup, the measured transmission value without using reflectors is at least 20 dB less than those with reflectors, indicating that the environmental noise is within acceptable levels for this setup.

Finally, we note that measurement errors for the designed reflectors could be due to the faults in the fabricated samples. However, we find this factor to be negligible in comparison to others described above, considering the difference between measured and simulated values for the flat reflectors.
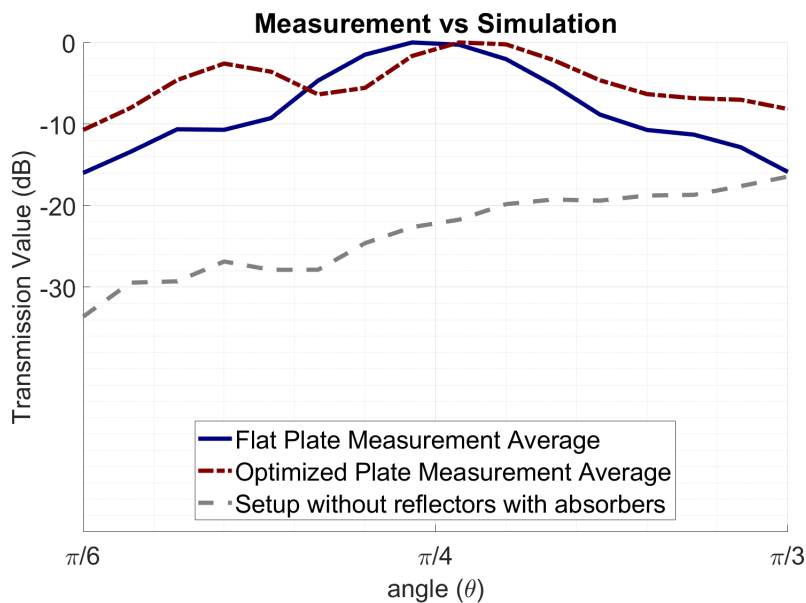
Figure 4.25: Normalized transmitted power with respect to the location of the receiving antenna in the presence and absence of reflectors in the NRL arch setup.

90
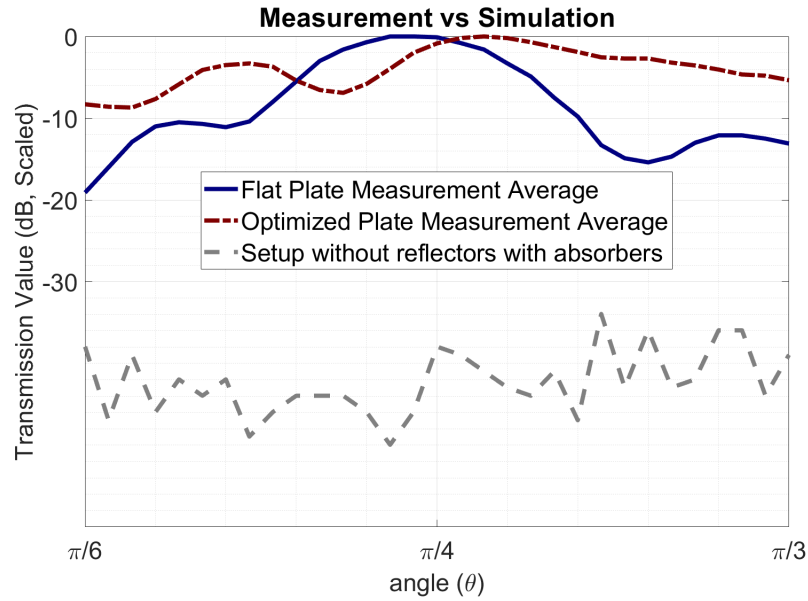
Figure 4.26: Normalized transmitted power with respect to the location of the receiving antenna in the presence and absence of reflectors in the free-space setup.

In this chapter, first a low-cost fabrication method involving 3D printing technology to fabricate the optimized reflectors in Chapter 3 is presented, followed by measurements of the fabricated reflectors. The designed reflectors are printed using a 3D printer, and then, a coating material is applied to obtain conductive surfaces. The measurements are performed in two different setups, namely NRL arch and free-space The measurements are performed in two different setups, namely NRL arch and free-space setups, leading to results that demonstrate the effectiveness of the designed reflectors. As discussed finally, measurements are generally consistent with simulations, but there are deviations mainly due to placement errors and environmental noises.

CHAPTER 5

CONCLUSION

In this study, an optimization procedure to design passive metallic reflectors for 5G mm-wave applications, as well as the fabrication and measurement of the designed reflectors, are presented.

In a 5G mm-wave application, the network infrastructure, especially the backhaul, is expected to consist of a large number of devices compared to the systems of the previous generations. Thus, energy efficient and low-cost (both in terms of manufacturing and operation) devices become crucial to construct 5G systems. The proposed and designed reflectors in this study demonstrate have high-performance metrics, i.e., controlled reflections, large bandwidths, and robustness against various errors, while they tick all the boxes in terms of energy efficiency and low cost.

The optimization mechanism used in this study is an elegant implementation of GAs. A novel approach based on a dynamic variation of reproduction rates is integrated into the GA implementation to improve the optimization technique. Besides, a multigrid approach, which enables a systematic and controlled scan over the solution space, is proposed and used to achieve better results in comparison to a conventional optimization. For the electromagnetic analyses, MLFMA is used as it provides extremely fast simulations, allowing full-wave solutions, even for optimization trials involving thousands of three-dimensional simulations. The result of each optimization is analyzed in detail in terms of design performances, some of which are presented in this thesis. Comparisons are made between various designs to discuss the reliability and capability of the optimization method and to show that the proposed optimization technique can be used to design reflectors for numerous beam-shaping applications.

A fabrication method involving a 3D printer and conductive coating is proposed as a reliable, low-cost fabrication method. Thanks to the relatively simple geometries of the designed reflectors and smooth variations on their surfaces, they can easily be fabricated via additive manufacturing. In addition, the reflectors can be scaled to operate at other frequencies without altering any step in the proposed fabrication process. The fabricated reflectors are measured in two different measurement configurations (setups). It is demonstrated that both setups can be used for successful measurements of the designed reflectors, while the free-space setup enables more freedom in terms of distances between the antennas and reflectors. In addition to the demonstrating the high-quality operations of the designed reflectors, the measurements show the effectiveness and reliability of the adopted fabrication method.

This study shows not only an effective design method and a low-cost fabrication technique for passive reflectors, but also diverse tracks for improvements in the followed methodologies. First, during a fabrication, the coating can be performed in a more standardized manner. Although a two-layer coating of conductive paint is shown to be adequate to obtain a sufficiently conductive surface on a 3D printed geometry, a more controllable coating method can be developed. Specifically, in the fabrication of the prototypes, the coating is performed by using hand-sprayed paint. This may result in an uneven distribution of the conductive layer on the fabricated surface if the application is not performed very carefully, while it is not practical in terms of time for mass production. Obviously, these issues can easily be solved via automated systems, if desired. Another improvement to this study can be related to the fabrication stage. The prototypes presented in this thesis are fabricated using a low-specification 3D printer and a low-cost filament. This kind of an equipment is used for relatively simple applications, and thankfully it has been adequate to fabricate the prototypes. However, even for prototypes, we need post-processing (sanding) to obtain surfaces with sufficient smoothness. In general, the overall fabrication time is relatively long, i.e., about one day per structure. Obviously, for a mass production, more advanced 3D printers can be used, together with automated coating procedures to quickly fabricate the reflectors.

REFERENCES

[1] M. Series, "Imt vision–framework and overall objectives of the future development of imt for 2020 and beyond," *Recommendation ITU 2083*, 2015.

[2] T. S. Rappaport, S. Sun, R. Mayzus, H. Zhao, Y. Azar, K. Wang, G. N. Wong, J. K. Schulz, M. Samimi, and F. Gutierrez, "Millimeter wave mobile communications for 5g cellular: It will work!," *IEEE Cccess*, vol. 1, pp. 335–349, 2013.

[3] O. N. Yilmaz, Y.-P. E. Wang, N. A. Johansson, N. Brahmi, S. A. Ashraf, and J. Sachs, "Analysis of ultra-reliable and low-latency 5g communication for a factory automation use case," in *2015 IEEE International Conference on Communication Workshop (ICCW)*, pp. 1190–1195, IEEE, 2015.

[4] H. Wymeersch, G. Seco-Granados, G. Destino, D. Dardari, and F. Tufvesson, "5g mmwave positioning for vehicular networks," *IEEE Wireless Communications*, vol. 24, no. 6, pp. 80–86, 2017.

[5] K. E. Skouby and P. Lynggaard, "Smart home and smart city solutions enabled by 5g, iot, aai and cot services," in *2014 International Conference on Contemporary Computing and Informatics (IC3I)*, pp. 874–878, IEEE, 2014.

[6] S. K. Rao and R. Prasad, "Impact of 5g technologies on smart city implementation," *Wireless Personal Communications*, vol. 100, no. 1, pp. 161–176, 2018.

[7] J. G. Andrews, S. Buzzi, W. Choi, S. V. Hanly, A. Lozano, A. C. Soong, and J. C. Zhang, "What will 5g be?," *IEEE Journal on Selected Areas in Communications*, vol. 32, no. 6, pp. 1065–1082, 2014.

[8] H. Papadopoulos, C. Wang, O. Bursalioglu, X. Hou, and Y. Kishiyama, "Massive mimo technologies and challenges towards 5g," *IEICE Transactions on Communications*, vol. 99, no. 3, pp. 602–621, 2016.

[9] T. E. Bogale and L. B. Le, "Massive mimo and mmwave for 5g wireless het-

net: Potential benefits and challenges," *IEEE Vehicular Technology Magazine*, vol. 11, no. 1, pp. 64–75, 2016.

[10] F. Z. Yousaf, M. Bredel, S. Schaller, and F. Schneider, "Nfv and sdn—key technology enablers for 5g networks," *IEEE Journal on Selected Areas in Communications*, vol. 35, no. 11, pp. 2468–2478, 2017.

[11] W. Khawaja, O. Ozdemir, Y. Yapici, F. Erden, and I. Guvenc, "Coverage enhancement for nlos mmwave links using passive reflectors," *IEEE Open Journal of the Communications Society*, vol. 1, pp. 263–281, 2020.

[12] Z. Peng, L. Li, M. Wang, Z. Zhang, Q. Liu, Y. Liu, and R. Liu, "An effective coverage scheme with passive-reflectors for urban millimeter-wave communication," *IEEE Antennas and Wireless Propagation Letters*, vol. 15, pp. 398–401, 2015.

[13] O. Ozdemir, F. Erden, I. Guvenc, T. Yekan, and T. Zarian, "28 ghz mmwave channel measurements: A comparison of horn and phased array antennas and coverage enhancement using passive and active repeaters," *arXiv preprint arXiv:2002.00121*, 2020.

[14] H.-T. Chou, L.-R. Kuo, and S.-J. Chou, "Design of shaped reflector antennas for the applications of outdoor base station antennas in lte mobile communications," *Radio Science*, vol. 53, no. 9, pp. 1023–1038, 2018.

[15] J. Bergmann, F. J. Hasselmann, and M. C. Branco, "A comparison between coverage performances of usual antenna arrays for radio base stations and a proposed shaped reflector design," in *1999 SBMO/IEEE MTT-S International Microwave and Optoelectronics Conference*, vol. 2, pp. 487–489, IEEE, 1999.

[16] D. Gies and Y. Rahmat-Samii, "Particle swarm optimization (pso) for reflector antenna shaping," in *IEEE Antennas and Propagation Society Symposium, 2004.*, vol. 3, pp. 2289–2292, IEEE, 2004.

[17] J. A. Martínez-Lorenzo, M. Arias, O. Rubiños, J. Gutiérrez, and A. García-Pino, "A shaped and reconfigurable reflector antenna with sectorial beams for lmds base station," *IEEE Transactions on Antennas and Propagation*, vol. 54, no. 4, pp. 1346–1349, 2006.

[18] W. Hu, M. Arrebola, R. Cahill, J. A. Encinar, V. Fusco, H. S. Gamble, Y. Alvarez, and F. Las-Heras, "94 ghz dual-reflector antenna with reflectarray subreflector," *IEEE Transactions on Antennas and Propagation*, vol. 57, no. 10, pp. 3043–3050, 2009.

[19] J. L. A. Quijano and G. Vecchi, "Optimization of a compact frequency- and environment-reconfigurable antenna," *IEEE Transactions on Antennas and Propagation*, vol. 60, no. 6, pp. 2682–2689, 2012.

[20] J. Kataja, S. Järvenpää, J. I. Toivanen, R. A. Mäkinen, and P. Ylä-Oijala, "Shape sensitivity analysis and gradient-based optimization of large structures using mlfma," *IEEE Transactions on Antennas and Propagation*, vol. 62, no. 11, pp. 5610–5618, 2014.

[21] C. Önol, S. Alkış, Ö. Gökçe, and Ö. Ergül, "Multifrequency and multidirection optimizations of antenna arrays using heuristic algorithms and the multilevel fast multipole algorithm," *Radio Science*, vol. 51, no. 7, pp. 1094–1108, 2016.

[22] G. Karaova, A. Altınoklu, and Ö. Ergül, "Full-wave electromagnetic optimisation of corrugated metallic reflectors using a multigrid approach," *Scientific Reports*, vol. 8, no. 1, pp. 1–11, 2018.

[23] J.-R. Poirier, H. Aubert, and J. David, "Minimizing electromagnetic scattering by varying height of metallic surfaces," *IEEE Microwave and Wireless Components Letters*, vol. 18, no. 5, pp. 299–301, 2008.

[24] J.-R. Poirier, H. Aubert, and D. L. Jaggard, "Lacunarity of rough surfaces from the wavelet analysis of scattering data," *IEEE Transactions on Antennas and Propagation*, vol. 57, no. 7, pp. 2130–2136, 2009.

[25] S. Chakravarty, R. Mittra, and N. R. Williams, "Application of a microgenetic algorithm (mga) to the design of broadband microwave absorbers using multiple frequency selective surface screens buried in dielectrics," *IEEE Transactions on Antennas and Propagation*, vol. 50, no. 3, pp. 284–296, 2002.

[26] M. Otomori, T. Yamada, K. Izui, S. Nishiwaki, and J. Andkjær, "A topology optimization method based on the level set method for the design of negative

permeability dielectric metamaterials," *Computer Methods in Applied Mechanics and Engineering*, vol. 237, pp. 192–211, 2012.

[27] L. Jiang, H. Li, W. Jia, X. Li, and Z. Shen, "Genetic optimization of photonic crystal waveguide termination for both on-axis and off-axis highly efficient directional emission," *Optics Express*, vol. 17, no. 12, pp. 10126–10135, 2009.

[28] G. Karaova, U. Tahan, T. Atmaz, and Ö. Ergül, "Design and optimization of nano-optical couplers for controlling transmission between electrically isolated nanowires," in *2019 Fifth International Electromagnetic Compatibility Conference (EMC Turkiye)*, vol. 1, pp. 1–6, IEEE, 2019.

[29] A. Altınoklu, G. Karaova, and Ö. Ergül, "Design and analysis of nano-optical networks consisting of nanowires and optimized couplers," in *2019 International Conference on Electromagnetics in Advanced Applications (ICEAA)*, pp. 0931–0936, IEEE, 2019.

[30] G. Karaova and Ö. Ergül, "Design and simulations of nano-optical couplers with genetic algorithms and mlfma," in *BEYOND 2019: Computational Science and Engineering Conference*, p. 45, 2019.

[31] M. S. Dadash, N. K. Nikolova, and J. W. Bandler, "Analytical adjoint sensitivity formula for the scattering parameters of metallic structures," *IEEE Transactions on Microwave Theory and Techniques*, vol. 60, no. 9, pp. 2713–2722, 2012.

[32] R. Eberhart and J. Kennedy, "A new optimizer using particle swarm theory," in *MHS'95. Proceedings of the Sixth International Symposium on Micro Machine and Human Science*, pp. 39–43, Ieee, 1995.

[33] N. Jin and Y. Rahmat-Samii, "Advances in particle swarm optimization for antenna designs: real-number, binary, single-objective and multiobjective implementations," *IEEE Transactions on Antennas and Propagation*, vol. 55, no. 3, pp. 556–567, 2007.

[34] M. Srinivas and L. M. Patnaik, "Genetic algorithms: A survey," *computer*, vol. 27, no. 6, pp. 17–26, 1994.

[35] Y. Rahmat-Samii and E. Michielssen, "Electromagnetic optimization by genetic algorithms," *Microwave Journal*, vol. 42, no. 11, pp. 232–232, 1999.

[36] M. Gen and L. Lin, "Genetic algorithms," *Wiley Encyclopedia of Computer Science and Engineering*, pp. 1–15, 2007.

[37] M. Franchitto, R. Faez, A. J. F. Orlando, M. C. Rezende, and I. M. Martin, "Electromagnetic behavior of radar absorbing materials based on conducting polymers," in *Proceedings of the 2001 SBMO/IEEE MTT-S International Microwave and Optoelectronics Conference. (Cat. No.01TH8568)*, vol. 1, pp. 137–140 vol.1, 2001.